

BUBBLES IN INKJET PRINTHEADS:
ANALYTICAL AND NUMERICAL MODELS

Samenstelling promotiecommissie:

prof. dr. ir. L. van Wijngaarden, voorzitter	Universiteit Twente
prof. dr. G. van der Steenhoven, secretaris	Universiteit Twente
prof. dr. rer. nat. D. Lohse, promotor	Universiteit Twente
dr. ir. H. Wijshoff, referent	Océ Technologies B.V.
ir. H. Reinten, deskundige	Océ Technologies B.V.
prof. dr. ir. A. de Boer	Universiteit Twente
prof. dr. ir. H. Tijdeman	Universiteit Twente
prof. dr. ir. A. Hirschberg	Technische Universiteit Eindhoven
prof. dr. ir. D. Rixen	Technische Universiteit Delft
prof. dr. A. Hosoi	Massachusetts Institute of Technology

This research was financially supported by the Dutch Technology Foundation



STW (project TMM.7509) and Océ Technologies B.V. This research was done at the research and development department of Océ, at the Physics of Fluids group at the University of Twente, and at the Hatsopoulos Microfluids laboratory at the Massachusetts Institute of Technology.

Nederlandse titel: Bellen in inkjet printkoppen: analytische en numerieke modellen

Publisher:

Roger Jeurissen, Physics of Fluids, University of Twente,
P.O. box 217, 7500 AE Enschede, the Netherlands
pof.tnw.utwente.nl

Cover design: Roger Jeurissen

Cover illustration: Top: A droplet that moves over the nozzle plate, showing that this translational motion does not lead to spreading. Center: Analytical en numerical predictions of the phase diagram of bubble volume oscillations, dimensionless driving pressure amplitude versus dimensionless bubble volume. Bottom: calculated translation of a bubble per cycle (arrows, scaled) and patterns of motion inferred from this translation, for a bubble radius of $R_b = 5 \mu m$.
Print: Gildeprint Enschede

© Roger Jeurissen, Reuver, the Netherlands 2009

No part of this work may be reproduced by print photocopy or other means without the permission in writing from the publisher.

ISBN 978-90-365-2921-1

BUBBLES IN INKJET PRINTHEADS:
ANALYTICAL AND NUMERICAL MODELS

proefschrift

ter verkrijging van
de graad van doctor aan de Universiteit Twente,
op gezag van de rector magnificus,
prof. Brinksma,
volgens besluit van het College van Promoties
in het openbaar te verdedigen
op vrijdag 23 oktober 2009 om 16.45 uur

door

Roger Josef Maria Jeurissen
geboren op 7 november 1977
te Soest

Dit proefschrift is goedgekeurd door de promotor:
prof. dr. rer. nat. Detlef Lohse

Contents

1	Introduction	1
2	The effect of bubbles on droplet velocity	5
2.1	Introduction	5
2.2	Experimental setup	6
2.3	Experimental results: bubble size and jet velocity	10
2.4	One dimensional disk bubble model	12
2.5	Comparison	14
2.6	Conclusions and outlook	16
	References	19
3	The effect of a bubble on acoustics	21
3.1	Introduction	21
3.2	Experimental setup	22
3.3	Experimental results: bubble oscillations	23
3.4	Bubble model	26
3.4.1	Simplified geometry	26
3.4.2	Channel acoustics	26
3.4.3	Matching the channel sections	28
3.4.4	Bubble volume oscillations	29
3.4.5	Model Results	30
3.5	Comparison between model and experiment	35
3.6	Conclusions and outlook	35
	Appendix A.1: Nozzle representation	37
	Appendix A.2: Glass connection channel representation	39
4	Acoustic measurement of bubble size	45
4.1	Introduction	45
4.2	Geometry of the inkjet printhead	46
4.3	Experimental parameters	47
4.4	Modeling the printhead	47
4.5	Comparing the model with experiments	53
4.6	Summary & Outlook	57
5	Regimes of bubble volume oscillations	61
5.1	Introduction	61
5.2	Dimensionless groups	63
5.3	Case study: a bubble in an inkjet print head	68

5.4	Numerical model	74
5.5	Validation	80
5.6	Conclusion	86
6	Translation of a bubble	89
6.1	Introduction	89
6.2	Numerical model	90
6.3	Theoretical predictions	97
6.4	Results of the numerical model	99
6.5	Conclusion	105
7	Marangoni flow	111
7.1	Introduction	111
7.2	Experimental observation of a translating droplet	113
7.3	Analysis	115
7.4	Validation and demonstration of the solenoidal theory	120
7.5	Conclusion and discussion	129
8	Conclusions	133

Chapter 1

Introduction

Of the states of matter, solid, liquid, and gas, this thesis treats the behavior of liquid with a little bit of gas, enclosed in solid material: a bubble in an inkjet printhead.

Inkjet printing is the process where liquid material is deposited onto a substrate by controlled ejection of liquid from a nozzle. Thus, inkjet printing is a controlled, additive, and non-contact production process. For many applications, these characteristics make inkjet printing the unique enabling technology. Examples are document printing, printed electronics, rapid prototyping 3D printers, and printing DNA microarrays. All these applications are in principle possible with other technologies. However, the non-contact nature of inkjet printing enables more substrate types, such as printing on textile, cardboard, paper, food products, and glass, possibly even with the same machine. The additive nature of inkjet printing make the process economically viable for dangerous or expensive materials, such as OLED displays and the reagents in DNA microarrays. The controlled nature of inkjet printing enables the use of materials that cannot be removed once applied. Full color 3D printers for rapid prototyping are a good example, since this is only possible with inkjet printing. Compared to toner printing, inkjet printing is a simpler procedure in principle. Since inkjet printing is additive, there is no need to remove and recycle material in an inkjet printer whereas a toner printer covers the entire substrate with toner and then removes and recycles the toner that was deposited at the wrong place. Inkjet printers are replacing toner printers or 'laser printers', because the process is much simpler. Inkjet printing is an increasingly important technology in many parts of society, but this pervasion would be much faster and more extensive if the problem of nozzle failure were overcome.

Nozzle failure is a temporary malfunction of a nozzle of a printhead. A printhead is the part of an inkjet printer that generates the droplets of ink and it usually comprises hundreds of nozzles. The failure of one nozzle therefore does not render the machine completely inoperable, but it decreases the accuracy. For some applications, such as document printing and rapid prototyping, this might be acceptable, especially if the nozzle failure can be detected so that the printing strategy can be modified to mask the detrimental effects. A DNA microarray that fails to detect a form of cancer only due to nozzle failure, for instance, is unacceptable. A piece of printed electronics where all electronic connections are severed along a line running across the circuit is useless. An OLED display

where one line of pixels is dead is rejected. For these applications, nozzle failure must be overcome. Even for document printing, when the printer is set to a high-quality presentation mode, nozzle failure might still be unacceptable. Extensive nozzle failure is unacceptable in any mode of printing. Since nozzle failure occurs more often at high printing speeds, nozzle failure must be overcome in order to increase printing speed even for noncritical applications. Therefore, the cause of nozzle failure must be understood in order to improve productivity and to enable new applications.

Nozzle failure is caused by entrained air bubbles. A droplet is produced by generating a pressure drop over a nozzle. This pressure pushes out a quantity of ink that will form a droplet outside of the printhead. In chapter 2, we show that the volume oscillations of the bubble cause nozzle failure though their influence on the pressure drop over the nozzle. The volume oscillations of a bubble in an infinite volume of liquid have been thoroughly investigated in the study of sonoluminescence and they are accurately described by the Rayleigh-Plesset equation. However, the volume of ambient liquid is not infinite in a printhead. Therefore, we developed the theory that describes volume oscillations of bubbles in finite volumes of liquid, and we applied this theory to the case of a bubble in an inkjet printhead. This is described in chapter 3. This theory was tested further in chapter 4 by using it to infer the bubble volume from the acoustic field that the bubble generates. In chapter 5, we analyzed the different regimes of bubble volume oscillations in a pipe by constructing a complete set of dimensionless groups of parameters. We provide an interpretation of these dimensionless groups as criteria for when the influence of finite size effects is important. These predictions are verified with a numerical model. The predictions based on the dimensionless groups were confirmed, showing that the volume oscillations of a bubble in an inkjet printhead and the influence of bubble volume oscillations on the pressure are now understood.

In chapter 6, we investigated how a bubble can be removed from an inkjet printhead. Directly after entrainment, a bubble is too small to influence the droplet formation. However, the bubble grows in the printhead. Eventually, its influence on the pressure is so strong that droplet formation is disrupted. If the bubble can be moved towards the nozzle and ejected before it can disrupt droplet formation, nozzle failure is prevented. Therefore, we investigated how a bubble moves in an inkjet printhead. In an inkjet printhead, the interaction between the bubble and the walls gives rise to forces that are absent in an infinite volume of liquid. We derived expressions for these forces and used these and the expressions for the forces that were already known from the theory of bubbles in infinite volumes of liquid to calculate the patterns of motion of a bubble in a printhead. As the bubble volume increases, the patterns of motion change. Initially, the pattern of motion is such that the bubble might be ejected. Further investigation may yield a useful combination of nozzle shape, actuation mode, and ink properties in which entrained bubbles are always ejected. Our research provided a tool that aids in the search for this combination.

Another way to prevent nozzle failure is to prevent air entrainment by identifying and removing the causes. Air bubbles are entrained due to dust particles that interfere with the droplet formation process. These dust particles are transported to the nozzle by flow of a thin layer of ink that coats the outside of the printhead. Therefore, we studied this ink flow in order to prevent it or to modify it so that dust no longer reaches the nozzles. In chapter 7, we identified the driv-

ing force of these flows. We also derived a simplification to the equations that govern these thin film Marangoni flows. These simplified equations were solved analytically to make quantitative predictions of a fingering instability that was observed in the ink layer. These predictions were compared with experimental data to validate the analysis.

In the presented research, the theoretical and numerical predictions were extensively validated with experimental results. The experiments are described in the following chapters, but they were mentioned only in passing in this chapter. The difficulties in obtaining experimental data were considerable as a result of the small length and time scales and the demanding specifications of the investigated system. High-speed imaging, long-range microscopy at large magnification, MEMS research tools, advanced electronic tools, and carefully set up experiments were necessary to obtain the results that made validation of the developed theory possible. The formulation of hypotheses was often driven by surprising and fascinating experimental results. The experiments were neither developed nor executed by the author of this thesis. They constitute the PhD thesis researches of Jos de Jong, Arjan van der Bos, and Herman Wijshoff, the work of Marc van de Berg, Hans Reinten, and the work of other researchers at Océ technologies B.V. Therefore, the advances in experimental methods that were realized in this research and the results that were obtained by experiments alone are not the focus of this thesis.

Chapter 2

Entrapped air bubbles in piezo-driven inkjet printing: Their effect on the droplet velocity¹

Air bubbles entrapped in the ink channel are a major problem in piezo-driven inkjet printing. They grow by rectified diffusion and eventually counteract the pressure buildup at the nozzle, leading to a breakdown of the jetting process. Experimental results on the droplet velocity u_{drop} as a function of the equilibrium radius R_0 of the entrained bubble are presented. Surprisingly, $u_{drop}(R_0)$ shows a pronounced maximum around $R_0 = 17 \mu m$ before it sharply drops to zero around $R_0 = 19 \mu m$. A simple one-dimensional model is introduced to describe this counterintuitive behavior which turns out to be a resonance effect of the entrained bubble.

2.1 Introduction

The number of possible applications of drop-on-demand (DOD) printing has increased considerably in the last few years. Beyond printing of text and pictures, the technique will be or has already been applied in diagnostics, the pharmaceutical industry, and the manufacturing of solar-cells and small and cheap devices [1,2]. Stability of the inkjet printing process and its reproducibility is crucial for most of these applications. Moreover, a large jetting frequency is desirable, in order to reduce the printing time.

Under normal conditions drop-on-demand piezo-electric inkjet printing [3–9] fulfills all the requirements with respect to stability and reproducibility. However, under certain conditions an air bubble can be entrained in the nozzle

¹Published as: Jos de Jong, Roger Jeurissen, Huub Borel, Marc van den Berg, Michel Versluis, Herman Wijshoff, Andrea Prosperetti, Hans Reinten, Detlef Lohse, *Entrapped air bubbles in piezo-driven inkjet printing: Their effect on the droplet velocity*, Phys. Fluids **18**, 121511 (2006).

[10–12], in particular at large jetting frequencies beyond 20 kHz . This air bubble grows by rectified diffusion [13–16]: While at pressure maxima air is squeezed out of the bubble, this loss is overcompensated at the pressure minima when the bubble expands, resulting in a net gas diffusion into the bubble. The bubble growth first leads to a modification of the drop production process and ultimately to the breakdown of the jetting. In ref. [12] we have introduced a method to acoustically monitor the inkjet channel, using the piezo as a sensor. In this way we could identify two different scenarios how bubbles are entrained at the nozzle and what their long-time effect on the jetting is. However, a direct optical observation of the entrained bubbles was not possible, as standard inkjet channels are not optically accessible.

In this chapter we overcome this restriction by introducing a glass channel and a glass nozzle plate, so that direct observation of the entrained bubble and its radial and translational dynamics becomes possible. The aim of the chapter is to correlate the bubble size (characterized by its equilibrium radius R_0 at standard static pressure) with the droplet velocity u_{drop} . We will find that surprisingly the droplet velocity first increases with increasing bubble size, namely from about 1.5 m/s without any air entrainment to about 2.5 m/s for an air bubble with $R_0 = 17 \mu m$. Then it decreases sharply and at a bubble radius of $R_0 = 19 \mu m$ the jetting breaks down.

The chapter is organized as follows: In section 2.2 we briefly introduce the experimental setup. The main section is section 2.3 where we present the correlation results between u_{drop} and the bubble size R_0 . In section 2.4 we introduce a simple one-dimensional model to qualitatively account for the observations. The comparison with the experimental data is favorable (section 2.5). section 2.6 contains the conclusions and an outlook towards future work.

2.2 Experimental setup

The printheads under consideration in this chapter are side-shooter printheads developed by Océ and used for professional printing. The schematic setup of the printhead is depicted in figure 2.1 [12]. The channel block is a graphite block with ink channels inside. The ink reservoir is connected to the channel and can be set at a specified pressure. In the rectangular ink channel one of the four walls is formed by a piezo element. Under the action of an applied voltage, the piezo first contracts increasing the volume of the ink channel thereby reducing the pressure and drawing in ink from the reservoir. During the second part of the pulse, the piezo expands, reducing the volume of the channel and ejecting a drop. The pressure waves generated by the piezo travel towards the ink reservoir, where they are reflected out of phase, and to the nozzle, where they are reflected in phase. The ink is pressed out through a 30 μm diameter electroformed nickel nozzle.

The piezo is actuated with 6 μs trapezoidal pulses with a repetition rate of 10 kHz , corresponding to one pulse every 100 μs , implying a 10 kHz firing frequency of the droplets. More details of the driving protocol are given in Ref. [12]. The transfer function of the piezo voltage, V_{act} , to the (maximum) nozzle velocity u_n can be calculated from viscous acoustics in pipes, as described e.g. by Tijdenman [17]. As shown in figure 2.2, in our printhead the dominant frequency is $f = 60 kHz$.

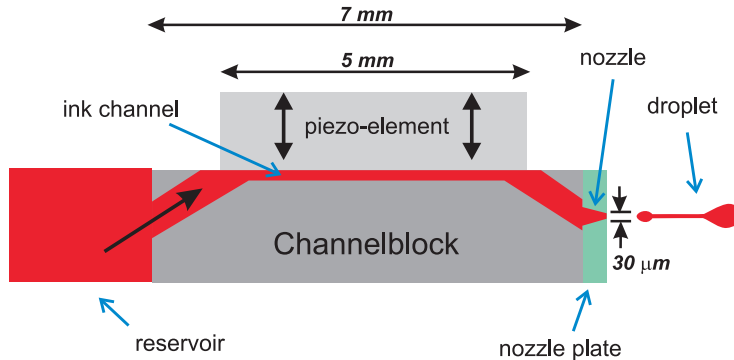


Figure 2.1: Sketch of the geometry of one ink channel of the printhead, which typically contains 256 of such channels. Only one channel on the printhead is actuated in our experiments. The pressure controlled reservoir supplies ink to the rectangular ink channel of length of 7 mm , width of $200\ \mu\text{m}$, and height of $150\ \mu\text{m}$. The piezo-element of length of 5 mm is covered with a foil of $20\ \mu\text{m}$ thickness, which is in direct contact to the ink. The nickel nozzle plate has round openings of diameter $30\ \mu\text{m}$, which serve as nozzles. The ejected droplets have a diameter of typically $35\ \mu\text{m}$.

To optically monitor the entrapped air bubbles, the standard printhead just described was modified. The nickel nozzle plate was replaced with (i) a glass connection channel and, in addition, (ii) a glass nozzle plate glued to it; see figure 2.3a for a sketch, figure 2.3b for a photograph and figure 2.3c for an enlargement of the entrained bubble. (i) The glass connection channel built by Micronit Microfluidics B.V. [19] is constructed from a glass plate with a thickness of $400\ \mu\text{m}$. The channel was obtained by powder-blasting the glass plate from both sides, leading to an hour-glass shape with a waist diameter of approximately $80\ \mu\text{m}$ and an inlet/outlet diameter of $250\ \mu\text{m}$. (ii) The glass nozzle plate was cut from a $70\ \mu\text{m}$ thick glass plate, which again was powder-blasted from both sides. The result is a conical nozzle shape with a diameter of about $50\ \mu\text{m}$ at the channel exit and $30\ \mu\text{m}$ at the nozzle end.

The nozzle plate and the connection channel are glued together to prevent leakage. The plates are then positioned onto a standard printhead, replacing the nickel nozzle plate. The glass is kept in place by small magnets, which push it against the printhead. To permit visualization of the air bubbles, a transparent ink was used. A continuous light source illuminates the glass from the back. A Phantom V7 high speed camera records the ejected droplets and the entrained air bubble at the same time. Due to the limited focal depth of the optical system, small bubbles in the ink channel can be visualized without optical distortions. For the chosen actuation voltage of 180 V , the droplet velocity without entrapped bubbles is $u_{drop} = 1.05\text{ m/s}$.

In order to start the experiment we cause the entrapment of an air bubble as described in [12]. Under the action of the oscillating pressure in the channel, the bubble grows by rectified diffusion [13–15] and causes the droplet formation to stop. At this point the acoustic field is switched off and the bubble starts dissolving. Shortly before the dissolution is complete, actuation is resumed and

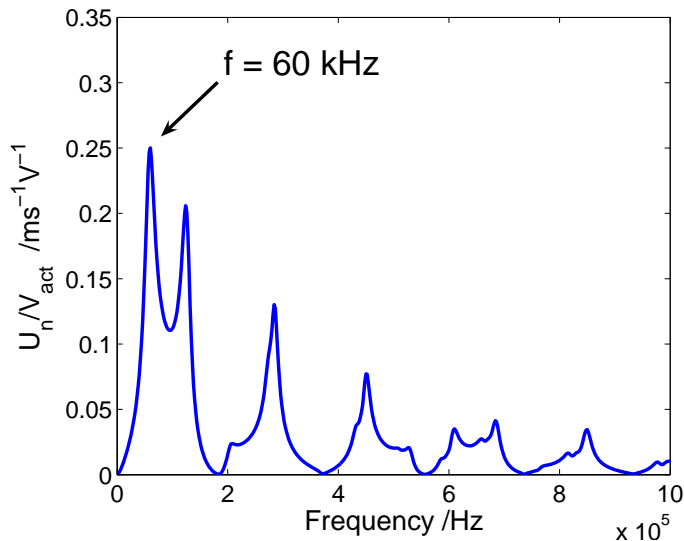


Figure 2.2: The transfer function for the printhead under consideration showing the dominant frequency at $f = 60 \text{ kHz}$. u_n is the nozzle velocity and V_{act} the applied actuation voltage. The transfer function is calculated according to Tijdenman’s model [17], which from various measurements in other channels is known to well represent the experimental one.

the high speed camera is triggered, recording the growth of the bubble and its effect on the ejection of drops.

In figure 2.4 we show an example of the time evolution of a bubble obtained in this way. We first let a bubble of initial size $R_0 = 26 \mu\text{m}$ dissolve; there is no actuation. The dissolution rate is constant at about 0.5 pl/s , as seen from figure 2.4b. At $t = 165 \text{ s}$ the actuation is switched on, leading to immediate jetting through the nozzle. The bubble which had nearly completely dissolved then starts to grow by rectified diffusion. Note the fast growth of the bubble compared to its dissolution. Once it has reached an equilibrium radius of about $19 \mu\text{m}$, jetting breaks down. This experiment shows the strong influence of the size of the entrained bubble on the jetting. Note that if we had waited some tens of seconds longer before switching on the actuation, the bubble nucleus would have completely vanished, and the nozzle would have resumed jetting without any problem – until the occurrence of the next bubble entrainment [12].

The recorded images of the ejected droplets and oscillating bubbles are analyzed with a gray-level threshold to determine the location of the edges of the droplets and bubbles. The images of both drops and bubbles only consist of some tens of pixels, limiting the accuracy of the size determination for smaller bubbles. Other sources of errors are optical diffraction and the assumed sphericity of the droplets and bubbles in the digital image analysis. For the ejected drops and for the bubbles *within* the channel (away from the walls) we do not have any indication of deviations from sphericity. However, the bubbles pushed against the glass nozzle plate seem to be slightly nonspherical.

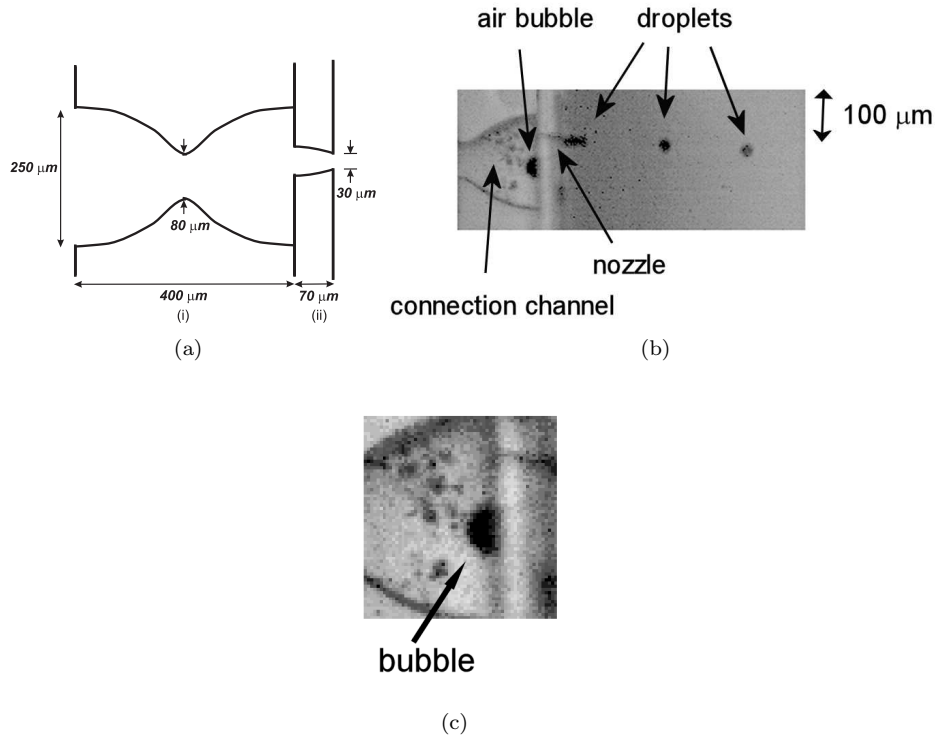


Figure 2.3: (a) Sketch of (i) the glass connection channel with (ii) the glass nozzle plate glued to it. (b) Photograph of half of the glass connection channel and the glass nozzle plate under operation. An air bubble is present in the connection channel close to the nozzle and droplets are ejected. The multimedia part of this figure shows a high-speed movie (taken at 40,000 frames per second) of the oscillating entrained bubble and the ejected droplets. (c) An enlargement of the bubble in (b). Here the arrow points at the bubble, that is pressed against the glass nozzle plate. The little dark dots left to the bubble originate from dirt on the glass connection channel. (enhanced online)

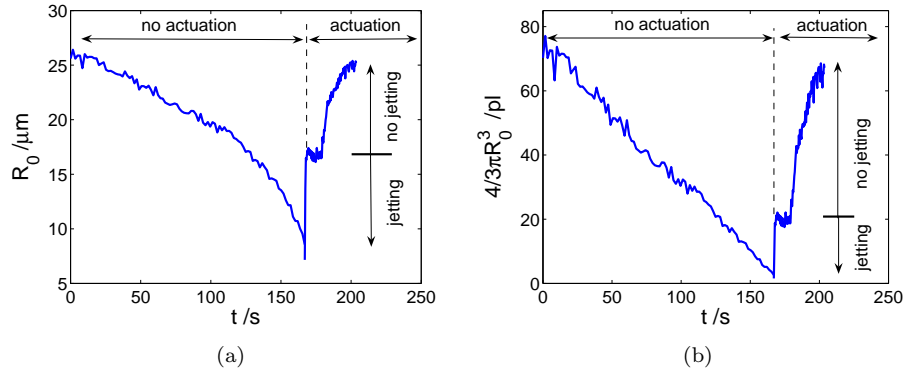


Figure 2.4: Equilibrium radius R_0 (a) and corresponding bubble volume (b) as function of time. Up to about $t = 165$ s there is no actuation and the bubble dissolves. At $t = 165$ s the actuation is started and the bubble, which was nearly fully dissolved, starts to grow by rectified diffusion. From the onset of actuation up to the time that the bubble has reached about $19 \mu\text{m}$ the nozzle is jetting. For larger bubbles the jetting breaks down.

During the experiments the jetting frequency is kept constant at 10 kHz . The frame rate of the camera is four times as high, 40 kfps . Therefore, 4 frames are acquired during one acoustic cycle, each at a different phase. To prevent motion blur the exposure time was set to $3 \mu\text{s}$.

2.3 Experimental results: bubble size and jet velocity

In figure 2.5a the droplet velocity is displayed as a function of time. The actuation is started at $t = 0$ s. Up to $t = 0.2$ s, the droplet velocity increases, reaching a maximum of 2.5 m/s . Then the droplet velocity gradually decreases to $u_{drop} = 1 \text{ m/s}$ at $t = 0.9$ s. A small amplitude oscillation of $f = 50 \text{ Hz}$ is superimposed onto the droplet velocity, reflecting the AC frequency of the devices. This effect is negligible compared to the effect of the entrained air bubble.

When the radius of the air bubble is plotted in figure 2.5b, it is evident that the air bubble grows over time by rectified diffusion. The scatter in the bubble radius is found to be quite large, due to the low contrast in the images and because multiple bubble radii are measured over one acoustic cycle. When we compensate for the latter by plotting the average radius (over 40 bubble radii) the bubble growth becomes more obvious as depicted in figure 2.5c. Combining figures (a) and (c) results in the droplet velocity u_{drop} as a function of the bubble radius R_0 , figure 2.5d. This figure is the main experimental result of this work. Surprisingly, u_{drop} first *increases* with increasing bubble radius. Around $R_0 \approx 17 \mu\text{m}$ the droplet velocity has a pronounced maximum before dropping sharply and jetting breaks down for bubble radii around $19 \mu\text{m}$.

To estimate the error in the bubble radius arising from averaging over only

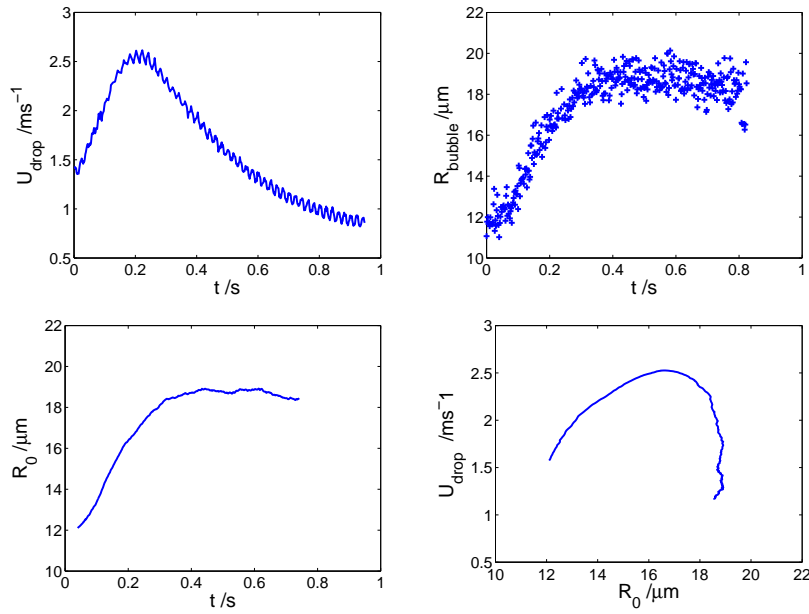


Figure 2.5: (a) The time development of the droplet velocity. At $t = 0$ the actuation is started with an air bubble in the ink channel, resulting in an initial droplet velocity enhancement. (b) The radius of the entrapped air bubble over time, showing large variation due to multiple frames during one acoustic cycle. (c) The averaged bubble radius as a function of time. (d) Droplet velocity u_{drop} as a function of the equilibrium radius R_0 of the entrapped air bubble. The curve shows a pronounced maximum.

four frames per cycle, we numerically model the bubble oscillations with the Rayleigh-Plesset equation [13] and then apply the very same averaging procedure as in the experiment. We find that in our parameter regime the error introduced is small as compared to other error sources. The major error is caused by the low contrast and hence the difficulties in edge detection. This error is estimated to be $\pm 4 \mu m$ (1 pixel). Note that this error is constant for all bubbles, i.e., it is *systematic* and not statistical. Therefore, the *shape* of the curve, and in particular the existence of the maximum, is not affected by it.

A quantitative explanation of the growth of the bubble as a function of *time* (figure 2.5c) and the dynamics of the bubble's position will be presented elsewhere. In particular, we will account for the observed saturation in size as a feedback effect: The grown bubble counteracts the pressure buildup in the channel. Being larger than its resonance size, the bubble is pushed away from the pressure antinode against the nozzle plate.

2.4 One dimensional disk bubble model

What is the origin of the maximum in $u_{drop}(R_0)$? It might be expected that the main effect of the bubble in the inkjet nozzle would be to counteract the pressure buildup in the nozzle, as the bubble gets compressed, thus making jetting more difficult. The experimental results, however, show that the effect of the bubble is more subtle, as for small entrained bubbles the droplet velocity increases. To get further insight into the problem, we develop a simple one-dimensional model. It will turn out that the droplet velocity increase is due to a *resonance* phenomenon.

The nozzle flow and the bubble dynamics are both driven by the channel acoustics. Note the feedback mechanism: The sound-driven bubble emits a pressure wave that propagates into the channel, modifying the channel acoustics and thus ultimately its own dynamics. A complete analysis of the system should therefore comprise the coupling of the channel acoustics to the bubble and nozzle dynamics. For the sake of simplicity, here we neglect the back-effect of the bubble on the channel acoustics.

As shown already in figure 2.2, the channel transfer function has a strong peak at $f = 60 kHz$. To simplify the analysis, in our one-dimensional model we will consider only this dominant frequency and impose a sinusoidal velocity in the channel. Extensions are easily possible, but not necessary to understand the physics of the peak in u_{drop} .

A sketch of the main ingredients of the model is shown in figure 2.6. The channel has cross section A_c and the time-dependent velocity therein (averaged over the cross section) is $u_c(t)$. The nozzle has an effective cross section A_n , length l_n , and the time-dependent (average) nozzle velocity is $u_n(t)$. In between channel and nozzle there is a *disk-shaped* compressible bubble, reflecting the one-dimensional nature of the model. In spite of the fact that, in this simple model, the bubble would actually block the channel, we allow an ink flow in the direction of the nozzle. The relevant feature of the bubble is its compressibility. This disk model is based on Oğuz and Prosperetti's work [18] who suggested this simplification for large bubbles in tubes.

The viscous friction in the nozzle is approximated by the friction factor of Poiseuille flow. From the Navier-Stokes equation, i.e., from balancing inertia,

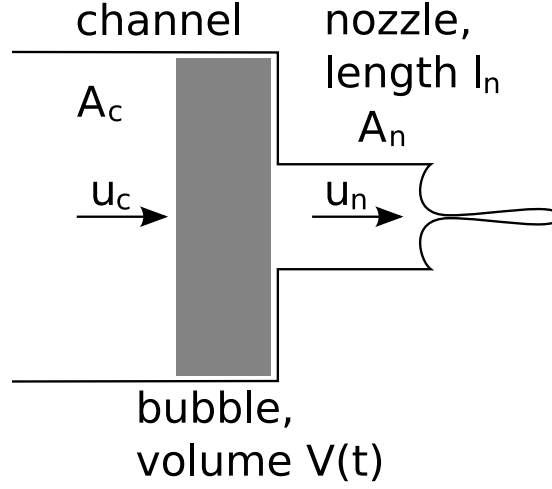


Figure 2.6: Sketch of the one-dimensional disk bubble model. Note that in spite of the (compressible) disk bubble we allow for an ink flow between channel and nozzle.

viscous friction, and the pressure drop through the nozzle between the bubble of pressure P_b and the ambient pressure P_0 , one obtains

$$\frac{du_n}{dt} = \frac{1}{\rho l_n} (P_b - P_0) - \frac{8\pi\nu}{A_n} u_n, \quad (2.1)$$

where ν is the kinematic viscosity and ρ the liquid density, assumed to be constant.

We now must connect the nozzle velocity u_n with the channel velocity u_c . In the absence of a bubble, continuity dictates that $A_n u_n = A_c u_c$. With the compressible bubble being present, one obtains

$$\frac{dV_b}{dt} = A_n u_n - A_c u_c. \quad (2.2)$$

The last ingredient is an assumed polytropic relation between the bubble volume $V_b(t)$ and its pressure $P_b(t)$:

$$P_b(t) = P_0 \left(\frac{V_0}{V_b(t)} \right)^\gamma. \quad (2.3)$$

Within the one-dimensional disk bubble model the bubble volume V_b can be transformed into an effective thickness $l_b(t) = V_b(t)/A_c$ and the equilibrium volume V_0 to an equilibrium thickness $l_0 = V_0/A_c$.

Upon combining the last two equations we get

$$\frac{dP_b}{dt} = -P_0 \gamma l_0^\gamma l_b^{(-\gamma-1)} \left(\frac{A_n}{A_c} u_n - u_c \right) \quad (2.4)$$

or, after linearization around the equilibrium volume (leading to $l_b = l_0$ in eq. (2.4)),

$$\frac{dP_b}{dt} = -\frac{P_0 \gamma}{l_0} \left(\frac{A_n}{A_c} u_n - u_c \right). \quad (2.5)$$

Equations (2.5) and (2.1) form a set of two linear first order differential equations for the bubble pressure $P_b(t)$ and the nozzle velocity $u_n(t)$. Upon eliminating P_b we obtain a forced harmonic oscillator equation for the nozzle velocity $u_n(t)$:

$$\ddot{u}_n + 2\beta\dot{u}_n + \omega_0^2(R_0)u_n = \omega_0^2(R_0)\frac{A_c}{A_n}u_c. \quad (2.6)$$

The forcing is due to the channel velocity $u_c(t)$. The bubble-size dependent eigenfrequency ω_0 is given by

$$\omega_0^2(R_0) = \frac{\gamma P_0}{\rho l_n} \frac{A_n}{A_c} = \frac{3\gamma P_0 A_n}{4\pi \rho l_n R_0^3} \quad (2.7)$$

and the damping coefficient is

$$\beta = \frac{4\pi\nu}{A_n}. \quad (2.8)$$

Both the normalized amplitude $\max_t(u_n(t, R_0))/\max_t(u_n(t, R_0 = 0))$ (see figure 2.7a) and the corresponding phase shift of roughly π (figure 2.7b) clearly show the resonance behavior. Here we have used $A_n = 1.3 \times 10^{-9} \text{ m}^2$ for the nozzle cross section, $\nu = 1.0 \times 10^{-5} \text{ m}^2\text{s}^{-1}$ for the kinematic viscosity, $l_n = 70 \text{ }\mu\text{m}$ for the nozzle length, $\rho = 1090 \text{ kg/m}^3$ for the ink density, $f_0 = \omega/(2\pi) = 60 \text{ kHz}$ for the dominant frequency, and $P_0 = 101.3 \text{ kPa}$ for the ambient pressure. Though the Peclet number $Pe = R_0^2 f/\kappa$ can approach 1 — for $R_0 = 10 \text{ }\mu\text{m}$, $f = 60 \text{ kHz}$, and the typical heat diffusivity of air $\kappa = 15 \times 10^{-6} \text{ m}^2/\text{s}$ one obtains $Pe = 0.4$ —, for simplicity the bubble has been assumed to behave isothermally throughout the cycle, $\gamma = 1$. Taking the adiabatic value $\gamma = 7/5$ only leads to a small shift of the maximum.

The location of the nozzle velocity maximum in figure 2.7a can straightforwardly be calculated, leading to the resonance radius

$$R_0^{res} = \left(\frac{3\gamma A_n^3 P_0}{4\pi \rho l_n (\omega^2 A_n^2 + 64\nu^2 \pi^2)} \right)^{\frac{1}{3}}. \quad (2.9)$$

Using above values for the parameters, we obtain $R_0^{res} \approx 13 \text{ }\mu\text{m}$, in agreement with figure 2.7a. The phase shift at resonance is not exactly π as a result of viscous friction in the nozzle.

2.5 Comparison

To compare the results of the model with the data, the resulting droplet velocity must be calculated from the nozzle velocity. This can be done with the method described by Dijkman [3].

The droplet formation is assumed to start when the nozzle velocity becomes positive, and to end when the kinetic energy density of the forming droplet becomes larger than the average kinetic energy density of the fluid flowing out of the nozzle. The ink that is outside the nozzle at that time is assumed to form the droplet. The droplet leaves the nozzle with a kinetic energy equal to the kinetic energy of the forming droplet at that time. The corrections for viscous and capillary effects during the formation of the tail are neglected. A parabolic flow profile is assumed.

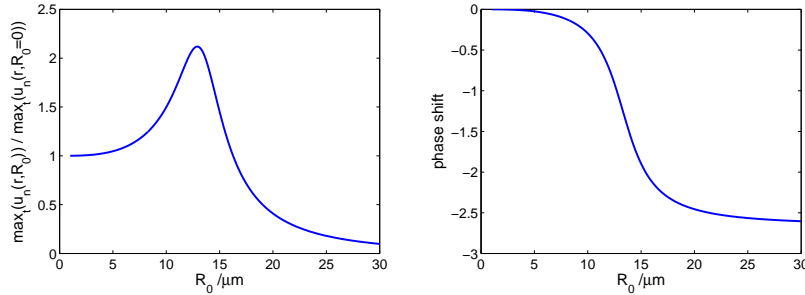


Figure 2.7: (a) Ratio of the maximal nozzle velocity $\max_t(u_n(t, R_0))$ for the case with an entrained bubble to the maximal nozzle velocity $\max_t(u_n(t, R_0 = 0))$ versus the equilibrium bubble radius R_0 within the one-dimensional disk bubble model. In (b) the respective phase shift is displayed, clearly signaling the resonance behavior.

For a sinusoidal driving velocity at a frequency of $f = 60 \text{ kHz}$ and the geometry of the experimental setup, the droplet velocity monotonously depends on the nozzle velocity amplitude, see figure 2.8. Therefore, a single peak in the nozzle velocity causes a single peak in the droplet velocity. Physically, the threshold observed in figure 2.8 of course reflects the finite amount of energy being necessary to form the surface of a drop.

Using this droplet formation model, the droplet velocity can be calculated as a function of the bubble radius, allowing for a direct comparison of the model results with the experimental ones, see figure 2.9. The amplitude of the channel flow was chosen to yield the experimentally determined droplet velocity in the absence of a bubble.

The bubble radius causing a maximum of 2.5 m/s in the droplet velocity was experimentally found to be $R_0 = 17 \pm 4 \mu\text{m}$. In contrast, the disk bubble model gives a maximum in the droplet velocity at $R_0 = 13 \mu\text{m}$ (for a mean nozzle radius of $20 \mu\text{m}$), quantitatively slightly off, but in reasonable agreement, considering the experimental systematic error of $4 \mu\text{m}$ in the estimate of the bubble radius and the simplifications of the model. The estimated maximum velocity is 5.3 m/s , about twice the measured value.

For a nozzle radius of $15 \mu\text{m}$, the calculated maximum in the droplet velocity shifts to $R_0 = 9 \mu\text{m}$, which is outside the uncertainty interval, see the dotted line in figure 2.9. However, the maximum droplet velocity of 3.0 m/s is closer to the measured velocity maximum.

The results of the model are sensitive to the exact value taken for the nozzle cross section. However, the shapes of the predicted and measured peaks are very similar. Even the sharp drop in droplet velocity for bubble sizes slightly below the size where droplet formation stops is represented in the one-dimensional disk model where it is caused by the infinite slope of the droplet velocity as a function of nozzle velocity.

Very small bubbles ($R_0 < 1 \mu\text{m}$) do not influence the droplet velocity. However, such bubbles are too small to be optically detected.

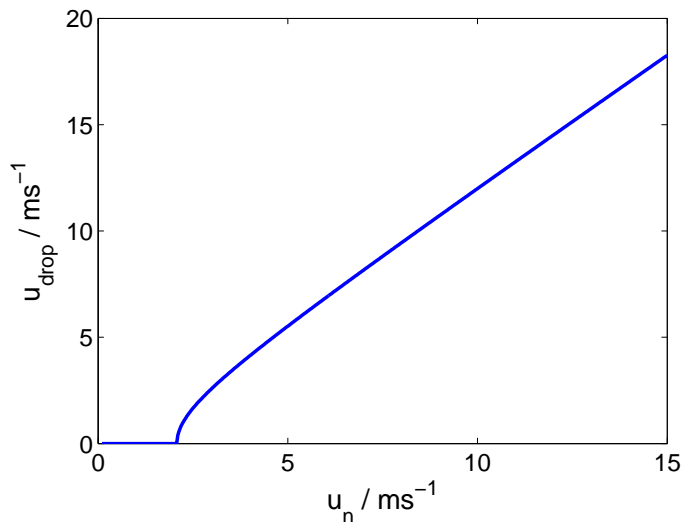


Figure 2.8: The droplet velocity calculated from the nozzle velocity according to Dijkstra [3] assuming a parabolic velocity profile. A nozzle velocity amplitude of at least $u_n = 2.0 \text{ m/s}$ is required to form a droplet.

2.6 Conclusions and outlook

The influence of the bubble size on the droplet velocity in an inkjet printhead was measured and modeled with a simple one-dimensional disk bubble model. As expected, *small* bubbles have no effect on the droplet velocity. The main finding of our work is that for *intermediate* bubble radii the droplet velocity is *increased* by the bubble. This remarkable phenomenon is caused by a resonance in the volume oscillations of the bubble, which are driven by the flow in the nozzle. *Large* bubbles cause nozzle failure. The droplet formation ceases abruptly as the bubble radius increases.

After these mechanisms have been understood, our research on the problem will go in several directions. First of all, we will extend the one-dimensional disk bubble model to a full, three-dimensional and two-way coupled numerical model. We hope that with such a model the effect of the bubble size and of its exact position on the droplet velocity can be quantitatively captured. Next, we would like to quantitatively understand the bubble growth by rectified diffusion and its dynamics in the ink channel. While rectified diffusion is quantitatively understood in still liquid in the bulk, both the liquid flow along the bubble and the constrained geometry in the nozzle strongly affect the bubble's growth and must be accounted for.

While we have revealed that small particles and an ink layer on the nozzle can lead to air entrainment [12], it is not yet clear why at certain frequencies and for certain shapes the nozzle is more vulnerable to air entrainment than at others. A resonance mechanism between the driving frequency and the eigenfrequency of the meniscus may be the origin for this observed strong dependence, and we plan to examine this conjecture.

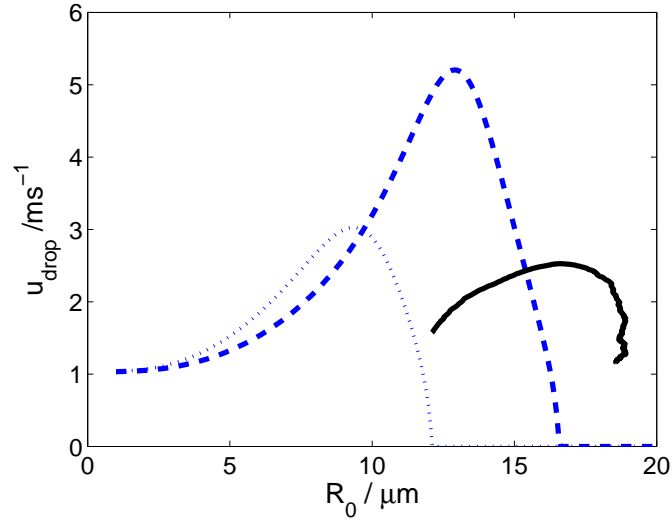


Figure 2.9: The droplet velocity u_{drop} as function of the equilibrium radius R_0 . The experimental results (solid) show a maximum in droplet velocity at $R_0 = 17 \mu\text{m}$. The numerical model displays a maximum at $R_0 = 13 \mu\text{m}$ (dashed) when the *average* nozzle radius $20 \mu\text{m}$ ($A_n = 1.3 \cdot 10^{-9} \text{ m}^2$) is taken as the relevant transversal length scale of the nozzle, and a maximum at $R_0 = 9 \mu\text{m}$ (dotted) when the *minimal* nozzle radius of $15 \mu\text{m}$ ($A_n = 7.1 \cdot 10^{-10} \text{ m}^2$) is taken instead.

From an application point of view the ultimate goal must of course be to avoid air entrainment or to immediately flush out the bubble once it has been entrained.

Bibliography

- [1] C. Williams, *Ink-jet printers go beyond paper*, Phys. World **19**, 24 (2006).
- [2] H. P. Le, *Progress and trends in ink-jet printing technology*, J. Imag. Sci. Tech **42**, 49 (1998).
- [3] J. F. Dijksman, *Hydrodynamics of small tubular pumps*, J. Fluid Mech. **139**, 173 (1984).
- [4] D. -Y. Shin, P. Grassia, and B. Derby, *Oscillatory limited compressible fluid flow induced by the radial motion of a thick-walled piezoelectric tube*, J. Acoust. Soc. Am. **114**, 1314 (2003).
- [5] J. M. Meacham, M. J. Varady, F. L. Degertekin, and A. G. Fedorov, *Droplet formation and ejection from a micromachined ultrasonic droplet generator: Visualization and scaling*, Phys. Fluids **17**, 100605 (2005).
- [6] W. Berggren, M. Westphall, and L. Smith, *Single-pulse nanoelectrospray ionization*, Anal. Chem. **74**, 3443 (2002).
- [7] A. U. Chen and O. A. Basaran, *A new method for significantly reducing drop radius without reducing nozzle radius in drop-on-demand drop production*, Phys. Fluids **14**, L1 (2002).
- [8] S. Elrod, B. Hadimioglu, B. Khuri-Yakub, E. Rawson, E. Richley, C. Quate, N. Mansour, and T. Lundgren, *Nozzleless droplet formation with focused acoustic beams*, J. Appl. Phys. **65**, 3441 (1989).
- [9] J. F. Dijksman, *Hydro-acoustics of piezoelectrically driven ink-jet print heads*, Flow, Turbulence, and Combustion **61**, 211 (1999).
- [10] J. D. Brock, I. M. Cohen, I. P. Ivanov, H. P. Le, and J. Roy, *Oscillations of an air bubble in an ink jet*, J. Imaging Sci. Technol. **10**, 127 (1984).
- [11] N. P. Hine, *Deaeration system for a high-performance drop-on-demand ink jet*, J. Imaging Technol. **17**, 223 (1991).
- [12] J. de Jong, H. Reinten, M. van den Berg, H. Wijshoff, M. Versluis, G. de Bruin, and D. Lohse, *Air entrapment in piezo-driven inkjet printheads*, J. Acoust. Soc. Am. **120**, 1257 (2006).
- [13] C. E. Brennen, *Cavitation and Bubble Dynamics* (Oxford University Press, Oxford, 1995).

- [14] M. M. Fyrillas and A. J. Szeri, *Dissolution or growth of soluble spherical oscillating bubbles*, J. Fluid Mech. **277**, 381 (1994).
- [15] S. Hilgenfeldt, D. Lohse, and M. P. Brenner, *Phase diagrams for sonoluminescing bubbles*, Phys. Fluids **8**, 2808 (1996).
- [16] T. G. Leighton, *The acoustic bubble* (Academic Press, London, 1994).
- [17] H. Tijdeman, *On the propagation of sound waves in cylindrical tubes*, J. Sound and Vibr. **39**, 1 (1975).
- [18] H. N. Oğuz and A. Prosperetti, *The natural frequency of oscillation of gas bubbles in tubes*, J. Acoust. Soc. Am. **103**, 3301 (1998).
- [19] Micronit Microfluidics B.V., P.O. Box 545, 7500 AM Enschede, The Netherlands.

Chapter 3

The effect of an entrained air bubble on the acoustics of an ink channel ¹

Piezo-driven inkjet systems are very sensitive to air entrapment. The entrapped air bubbles grow by rectified diffusion in the ink channel and finally result in nozzle failure. Experimental results on the dynamics of fully grown air bubbles are presented. It is found that the bubble counteracts the pressure buildup necessary for the droplet formation. The channel acoustics and the air bubble dynamics are modelled. For good agreement with the experimental data it is crucial to include the confined geometry into the model: The air bubble acts back on the acoustic field in the channel and thus on its own dynamics. This two-way coupling limits further bubble growth and thus determines the saturation size of the bubble.

3.1 Introduction

Drop-on-Demand inkjet printing [1] has been and will be applied to many industrial applications [2] which range from printing color filters for flat panel displays [3] to DNA microarrays [4]. Still, the most common application is the printing of text and graphics on paper. A small volume of ink is deposited on the paper in a very controlled way. The stability of the printing process is crucial, especially since the productivity and accuracy standards are continuously raised. The principle of a piezo printhead is a piezo element which deforms an ink channel, thereby building up pressure at the nozzle [5]. One of the biggest challenges in piezo-acoustic printing is the entrapment of air bubbles [6–8]. They disturb the pressure buildup at the nozzle and lead to nozzle failure. Therefore, the monitoring of the printing process while printing is crucial.

Air entrapment at the nozzle can be detected by using the actuating piezo

¹Published as: R. Jeurissen, J. de Jong, H. Reinten, M. van den Berg, H. Wijshoff, M. Versluis, D. Lohse, *Effect of an entrained air bubble on the acoustics of an ink channel*, J. Acoust. Soc. Am. **123**, 2496-2505 (2008).

as a sensor [8]. An entrapped bubble has to be removed as quickly as possible to continue the printing process. However, waiting for the dissolution of the bubble is very time consuming and decreases the productivity of the printhead. Therefore, it is desirable to actively get rid of the air bubble. To accomplish this, first the bubble dynamics have to be understood. This article focusses on the dynamics of fully grown air bubbles where the jetting of droplets has completely broken down. The entrapped air bubble oscillates in the acoustic field. During bubble compression, gas is pressed out of the bubble, while during expansion dissolved gas enters into the bubble. For a large enough driving pressure the second effect dominates and a net growth of the air bubble results (rectified diffusion, see refs. [9, 10]). Finally, the bubble reaches a dynamic equilibrium size.

The presence of an equilibrium radius signals the saturation: The bubble has become relatively large, thereby influencing the acoustic waves in the printhead, hence limiting its own oscillations and growth. During actuation, the bubble will then just remain in the ink channel oscillating around its equilibrium radius. By employing a glass connection channel and high speed imaging, the air bubble can be visualized and its dynamics can be resolved.

The dynamics of a bubble in a tube differ from the dynamics of a bubble in an infinite volume of liquid [11, 12]. Due to the finite size of the ambient liquid, the natural frequency of oscillation usually decreases when the bubble becomes larger with respect to the pipe [13, 14]. Qin et al showed that in some cases, the opposite occurs [15], indicating that the surrounding system and its behavior are relevant for the dynamics of the bubble. When the bubble touches the walls during expansion, the bubble can become non-spherical [16, 17]. Cui et al [18] found that for a bubble between two parallel plates, the acoustic field generated by the bubble is essential for the evolution of the bubble. For the saturated bubbles in an inkjet printhead, we find the two-way coupling effect, i.e., the backreaction of the bubble on the acoustic field, to be crucial, whereas for small bubbles this effect can be neglected [19]. To model the two-way coupling, the one dimensional disk bubble model of ref. [19] is extended to a fully coupled model. Moreover, the bubble itself is now modelled with a linearized Rayleigh-Plesset equation. We find that with such an extended model the experimental data can be described very well. The two-way coupling effect is found to be crucial. The pressure at the nozzle and the transfer function of the velocity in the nozzle over the actuator voltage are changed significantly by the entrained air bubble.

The article is organized as follows: First, in Section 3.2 the details of the experimental setup are discussed. Next, in Section 3.3, the experimental air bubble dynamics are presented. Section 3.4 is devoted to the bubble model. For readability, some technical details of the model are separated in an appendix. The comparison between the experiments and the model is given in Section 3.5. The paper ends with the conclusions and an outlook, Section 3.6.

3.2 Experimental setup

The setup consists of a side-shooter printhead [19], developed by Océ Technologies. In this printhead, a 5 mm long rectangular ink channel is deformed by a piezo element, thereby generating acoustic waves in the channel. The waves

result in a pressure and velocity field near the nozzle. To visualize the dynamics of the entrained air bubble, a glass connection channel was interposed between the ink channel and a glass nozzle plate, similar to [19]. This channel has a length of $400\ \mu\text{m}$ and an hourglass shape. The waist diameter is $80\ \mu\text{m}$ and the maximum diameter $250\ \mu\text{m}$ at the in- and outlet. On top of the connection channel a glass nozzle plate is glued. The conical nozzles have a diameter of $30\ \mu\text{m}$ at the exit and $50\ \mu\text{m}$ at the inlet. The pulse applied to the printhead is trapezoidal lasting $8\ \mu\text{s}$ ($2\ \mu\text{s}$ rise time, $4\ \mu\text{s}$ plateau, and $2\ \mu\text{s}$ fall time), with a repetition rate of $20\ \text{kHz}$.

After the bubble has been entrained, it is allowed to grow to its diffusive equilibrium. The droplet formation process has now ceased completely. The entrained air bubble is visualized by a Shimadzu HPV-1 high-speed camera (maximum frame rate of $1\ \text{Mfps}$) and a bright Olympus light source. The Shimadzu HPV-1 is capable of recording 100 frames and has an exposure time as short as $250\ \text{ns}$. A single frame showing the entrapped air bubble in the glass channel is depicted in figure 3.1. In this article we restrict ourselves to fully developed bubbles, so that the bubbles start every acoustic cycle with the same radius.

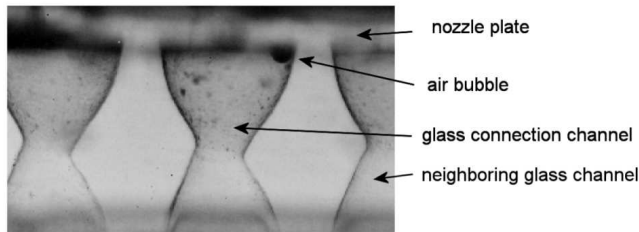


Figure 3.1: The entrapped air bubble is trapped in the glass connection channel. While actuating, the fully grown air bubble will just remain oscillating in the channel. Note the position of the air bubble: due to the Bjerknes forces it is pushed against the glass walls. (The bubble is larger than its resonance size). To the left and right of the channel with the bubble, the neighboring channels can be seen.

3.3 Experimental results: bubble oscillations

For a driving voltage of $190\ \text{V}$, the radius of the bubble is plotted in figure 3.2a. The equilibrium value was found to be $R_0 = 23\ \mu\text{m}$, the minimum radius was $15\ \mu\text{m}$ and the maximum radius was $26\ \mu\text{m}$. Two successive acoustic cycles ($50\ \mu\text{s}$ each) were captured by the camera with a frame rate of $1\ \text{Mfps}$. Plotting these acoustic cycles modulo the period $T = 1/f = 50\ \mu\text{s}$ shows the reproducibility of the oscillation, thereby confirming the assumption of a bubble in dynamical equilibrium, figure 3.2b. The error in the data is caused by the assumed sphericity of the air bubble and by the limited resolution of the images. The error is estimated to be $2\ \mu\text{m}$ in radius. Note that the expansion of the bubble is smaller than the compression. As we will see in the next section, this is due to the finite size of the ink channel. When reducing the actuating

voltage to 120 V, we see a decrease in the saturation size of the air bubble, from $R_0 = 23 \mu m$ to $R_0 = 18 \mu m$, see figure 3.3. The minimum bubble radius is now found to be $13 \mu m$, and its maximum is $22 \mu m$.

Note the position of the air bubble: it is pushed against the nozzle plate. We attribute this to the flow field generated by the bubble oscillations. This flow field pulls the bubble towards the walls. This effect is called the secondary Bjerknes force [20]. Inspection of the obtained images reveals the bubble shape. When walls are nearby, the bubble oscillates non-spherically. After a large expansion, the shape of the bubble is nearly a quarter of a sphere that is bounded by the nozzle plate and the channel wall. When the bubble is compressed, it becomes nearly spherical. At lower actuation amplitudes, the bubble oscillations are more spherical. This is expected to be caused by a decrease in secondary Bjerknes Force. By reducing the actuation voltage, the amplitude of the acoustic field is reduced, and so are the bubble oscillations. Therefore, when the bubble oscillations are decreasing, so is the secondary Bjerknes force that pulls the bubble towards the wall, resulting in a less deformed bubble and a reduction of the error introduced by the assumed sphericity of the bubble.

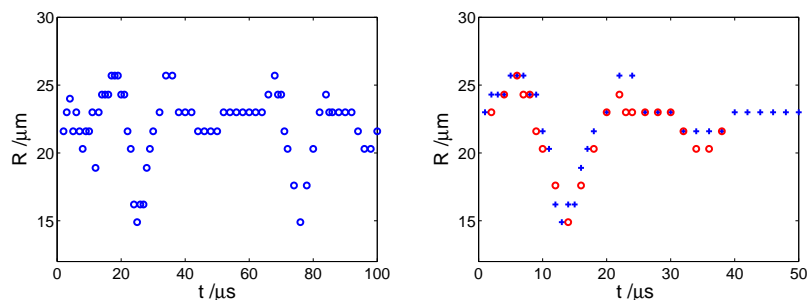


Figure 3.2: a) The radius $R(t)$ of the entrained bubble actuated with 190 V as a function of time. The actuation frequency is 20 kHz. b) To show the reproducibility of the bubble oscillations, the radius is plotted modulo its periodicity $T = 1/f = 50 \mu s$. The different cycles are denoted by different symbols.(color online)

The Fast Fourier Transform (FFT) is calculated to extract the frequencies present in the oscillations of the bubble, and is depicted in figure 3.4. To obtain a smooth spectrum, the bubble radius fluctuation $\Delta R(t)$ is padded with trailing zeros before calculating the FFT. At both the driving voltage of 120 V where $R_0 = 18 \mu m$, and at a driving voltage of 190 V where $R_0 = 23 \mu m$, the main frequency of the bubble oscillations is found to be 60 kHz.

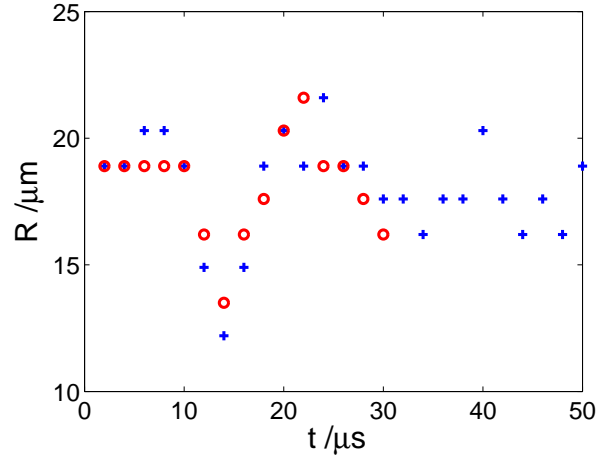


Figure 3.3: The radius $R(t)$ of the entrained bubble actuated with 120 V as a function of time. The actuation frequency is 20 kHz . Two acoustic cycles are displayed.(color online)

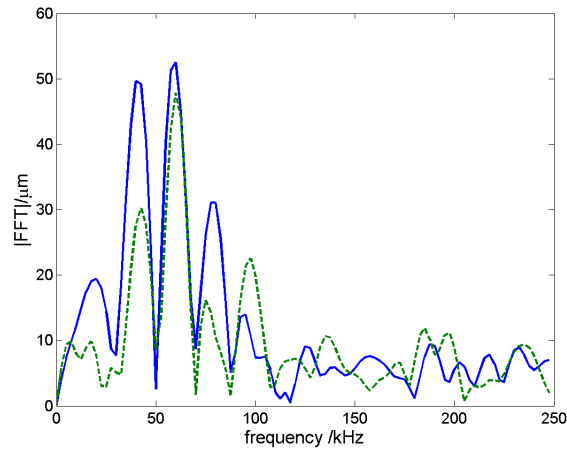


Figure 3.4: The FFT of $\Delta R(t)$ for a driving voltage of 190 V , where the saturated ambient bubble radius is $R_0 = 23\text{ }\mu\text{m}$ (solid), and for 120 V , where the saturated ambient bubble radius is $R_0 = 18\text{ }\mu\text{m}$ (dashed): The largest maximum remains nearly unchanged at 60 kHz , while the second largest maximum at 40 kHz is larger at 190 V .(color online)

3.4 Bubble model

3.4.1 Simplified geometry

To model the bubble oscillations in the ink channel, a one-dimensional model is used. The cylindrical channel is divided into 4 sections, see figure 3.5. Section 1 is the actuation channel, where the piezo is located. Section 2 is the standard connection channel. Section 3 is a model of the glass connection channel which we have included for visualization and section 4 is the nozzle. The interface between the sections is positioned at respectively, x_1 , x_2 , and x_3 . The channel acoustics, bubble dynamics, and nozzle flow are modelled. The bubble is located in the connection channel, and similar to the experiments it experiences the pressure at x_3 between the glass connection channel and the nozzle. The effect of the bubble on the channel acoustics is included in this model.

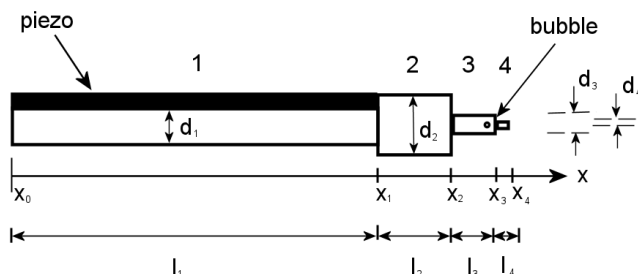


Figure 3.5: A schematic overview of the ink channel. It is divided into four sections. Section 1 is the channel where the piezo is located. Section 2 is the standard connection channel. Section 3 is a representation of the glass connection channel, and section 4 is the nozzle. The interfaces between the sections are positioned at respectively, x_1 , x_2 , and x_3 . The (undisturbed) diameters d_j for the four sections $j = 1, 2, 3, 4$ are $d_1 = 195 \mu\text{m}$, $d_2 = 250 \mu\text{m}$, $d_3 = 80 \mu\text{m}$, and $d_4 = 30 \mu\text{m}$, respectively.

The channel acoustics is first treated section by section. Then the channel sections are coupled through the matching of interface conditions. The channel deformations are only represented by the cross sectional variations.

3.4.2 Channel acoustics

The channel is actively deformed when applying a voltage to section 1, and passively by the pressure inside the channel. The channel cross sectional area $A_j(x, t)$ of section j can be written as

$$A_j(x, t) = A_{0,j} + a_{a,j}(t) + a_{p,j}(x, t). \quad (3.1)$$

Here x is the spatial coordinate in the channel direction, $A_{0,j}$ is the undisturbed, equilibrium, cross sectional area, $a_{a,j}(t)$ is the variation of cross sectional area due to the actuator voltage V_j (obviously being nonzero only for section 1), and $a_{p,j}(x, t)$ is the passive deformation of the channel in response to the pressure, $P_j(x, t)$, inside the channel. Note that $a_{a,j}(t)$ is constant over a channel section.

j	section	α_j / V^{-1}	β_j / $m^2 N^{-1}$	d_j / μm	$c_{eff,j}$ / ms^{-1}	l_j / μm
1	actuation channel	$-3.43 \cdot 10^{-6}$	$8.36 \cdot 10^{-10}$	195	803	5000
2	connection channel	0	0	250	1250	1000
3	glass connection	0	0	80	1250	149
4	nozzle	0	0	30	1250	42

Table 3.1: Parameters of the channel sections.

For frequencies below the Nyquist frequency $f_n = 500 \text{ kHz}$ of the measurements, the wavelength $\lambda > 2.5 \text{ mm}$ is much larger than the channel radius $d_j < 250 \mu m$, so the radial component of the pressure gradient and velocity become negligible with respect to the axial components. Linearize the channel deformations:

$$\begin{aligned} a_{a,j}(t) &= \alpha_j V_j(t) A_{0,j} \\ a_{p,j}(x,t) &= \beta_j P_j(x,t) A_{0,j} \end{aligned} \quad (3.2)$$

with:

$$\begin{aligned} \alpha_j &= \frac{1}{A} \left(\frac{\partial A}{\partial V} \right)_P \\ \beta_j &= \frac{1}{A} \left(\frac{\partial A}{\partial P} \right)_V \end{aligned} \quad (3.3)$$

α_j , β_j , $A_{0,j}$ and $V_j(t)$, for $j = 1, 2, 3, 4$, are assumed to be constant over a channel section. α_j and β_j are calculated with a plane-strain calculation in the commercial solid mechanics model ANSYS by Océ Technologies B.V. Each channel section is characterized by the magnitude of these quantities, and the length l_j of the channel section. In table 3.1 we have summarized the parameters characterizing the sections.

The wave equation for a deforming channel can be derived from the Navier-Stokes equation by a control volume analysis in the low reduced frequency approximation [21] where $R_c \ll \lambda$. Insert the linearized channel deformations, equation (3.2), into the wave equation for a deforming channel:

$$\partial_t^2 P_j = c_{eff,j}^2 \partial_x^2 P_j - \alpha_j \rho c_{eff,j}^2 \partial_t^2 V_j - c_{eff,j}^2 \frac{\mu}{A_{0,j}} \partial_x \oint_{\partial A_j} \partial_n u \, ds \quad (3.4)$$

where u is the axial velocity field, $\mu = 0.01 \text{ Nm}^{-2}\text{s}$ is the viscosity, $\rho = 1090 \text{ kgm}^{-3}$ is the density of the ink, and $c_{eff,j}$ the effective phase velocity, which is given by:

$$c_{eff,j} = \sqrt{\frac{c^2}{1 + \beta_j c^2 \rho}} \quad (3.5)$$

where $c = 1250 \text{ ms}^{-1}$ is the velocity of sound in the ink. Equation (3.4) is linear, and can be solved in the frequency domain, so that in each channel section the pressure is given by:

$$P_j(x,t) = p_{1,j} e^{i(\omega t - k_{1,j} x)} + p_{2,j} e^{i(\omega t - k_{2,j} x)} - \alpha_j c_{eff,j}^2 \rho v_j \quad (3.6)$$

where $p_{1,j}$ and $p_{2,j}$ are the amplitudes of the waves propagating in the negative and positive x -direction, respectively. The driving voltage is $V_j = v_j e^{i\omega t}$, where v_j is the amplitude and ω is the angular frequency. Note again that only section 1 experiences direct driving, $v_1 \neq 0$, whereas sections 2, 3, and 4 have $v_j = 0$. The angular frequency ω ranges from $-2\pi \cdot 10^7 \text{ rads}^{-1}$ to $2\pi \cdot 10^7 \text{ rads}^{-1}$. It is not to be confused with the drop-on-demand driving frequency $f_{DoD} = 5 \text{ kHz}$, which is chosen such that the acoustic field is completely damped at the end of the acoustic cycle. $k_{1,j}$ and $k_{2,j}$ are the wave numbers of the waves propagating in the negative and positive x direction, respectively. Inserting the velocity profile of a cylindrical pipe given by Womersley [23] and dropping the $e^{i\omega t}$ term leads to:

$$k_{n,j} = (-1)^n \frac{\omega}{c_{eff,j}} \left(1 + \frac{2\sqrt{i}J_1\left(\text{Wo}_j i^{\frac{3}{2}}\right)}{\text{Wo}_j J_0\left(\text{Wo}_j i^{\frac{3}{2}}\right)} \right)^{-\frac{1}{2}} \quad (n \in \{1, 2\}) \quad (3.7)$$

where $\text{Wo}_j = \frac{1}{2}d_j\sqrt{\frac{\omega\rho}{\mu}}$ is the Womersley number. The functions J_0 and J_1 are the ordinary Bessel functions of the first kind, of zeroth and first order, respectively. With (3.7) substituted into (3.6) one finally obtains a general expression for the pressure $P_j(x, t)$ in section j .

The glass connection channel ($j = 3$) and the nozzle ($j = 4$) are not cylindrical but have a more complicated shape. However, both sections can be modelled by an equivalent cylindrical section, as shown in Appendix A. For the glass connection channel an equivalent diameter of $d_3 = 80 \mu\text{m}$ and an equivalent length of $l_3 = 148 \mu\text{m}$ are found. The conical nozzle is described by a cylinder of equivalent diameter $d_4 = 30 \mu\text{m}$ and equivalent length of $l_4 = 42 \mu\text{m}$. Over most of their length, the radii of the real nozzle and glass connection channel are larger than the radii of the equivalent cylindrical sections. The equivalent lengths are chosen to keep the acoustic admittance constant. Since the acoustic admittance is proportional to the ratio of the cross sectional area over the length of the cylinder, see equation 3.26, the real lengths are also larger than the equivalent lengths.

The flow rate through the cylindrical nozzle is a function of the pressure drop over the nozzle in the frequency domain. The expression given by Womersley [23] for the amplitude of the volume flow rate q_j in a cylinder (the nozzle) is

$$q_j = p_j \frac{\pi d_j^2 i}{4l_j \omega \rho} \left(1 - \frac{2J_1\left(\text{Wo}_j i^{\frac{3}{2}}\right)}{i^{\frac{3}{2}} \text{Wo}_j J_0\left(\text{Wo}_j i^{\frac{3}{2}}\right)} \right) \quad (3.8)$$

3.4.3 Matching the channel sections

We now have to match the pressure fields $P_j(x, t)$ for the different sections j . The boundary conditions at the ends of each section are continuity of pressure and flow. The pressure should be continuous at the matching positions x_1, x_2, x_3 (figure 3.5),

$$P_j(x_j) = P_{j+1}(x_j), \quad (3.9)$$

$j = 1, 2, 3$.

Moreover, continuity requires that the volume flow rate should also be continuous:

$$A_j u_j(x_j) = A_{j+1} u_{j+1}(x_j) \quad (3.10)$$

for $j = 1, 2$. Here $u_j(x)$ is the velocity averaged over the cross section, $A_j(x_j)$. The effect of the bubble is included in the volume flow rate balance between section 3 and 4 where the bubble sits by explicitly considering the flux Q_b into the bubble,

$$A_3 u_3(x_3) = A_4 u_4(x_3) + Q_b \quad (3.11)$$

These boundary conditions together with equations (3.6) and (3.7) (the equation for the propagation of acoustic waves) provide a complete description of the channel acoustics.

3.4.4 Bubble volume oscillations

The behavior of spherical bubbles in large volumes is described by the Rayleigh-Plesset equation (see e.g. Brennen [20])

$$R\ddot{R} + \frac{3}{2}\dot{R}^2 = \frac{1}{\rho} \left[\left(P_0 + \frac{2\sigma}{R_0} - P_v \right) \left(\frac{R_0}{R} \right)^{3\gamma} + P_v - \frac{2\sigma}{R} - \frac{4\mu\dot{R}}{R} - P_\infty(t) \right] \quad (3.12)$$

Here $R(t)$ is the bubble radius. $\rho = 1090 \text{ kgm}^{-3}$ is the ink density, σ is the surface tension, $\sigma = 0.028 \text{ Nm}^{-1}$, R_0 is the bubble radius at ambient pressure $P_0 = 101325 \text{ Nm}^{-2}$, $P_v = 2400 \text{ Nm}^{-2}$ is the vapor pressure, $\mu = 0.01 \text{ Nm}^{-2}\text{s}$ is the viscosity, and γ is the polytropic index. The bubble is assumed to oscillate isothermally, i.e. $\gamma = 1$. $P(t)$ is the pressure fluctuation caused by the actuator so that far from the bubble the pressure is

$$P_\infty(t) = P_3(x_3) = P_0 + P(t) + \Delta P(t). \quad (3.13)$$

Here $\Delta P(t)$ is the pressure disturbance caused by the bubble. This term can be neglected for bubbles in an infinite volume of liquid. In a channel however, this term is significant. It reflects the coupling between the channel acoustics and the bubble volume oscillations. The pressure $P_\infty(t)$ is the pressure at locations so far from the bubble, that the pressure due to the inertia of the radial flow field is negligible with respect to the imposed pressure fluctuations.

For small fluctuations of the driving pressure $P(t) \ll P_0$ and bubble radius $\Delta R(t) \ll R_0$ the RP equation (5.32) can be linearized. The response of the bubble can be transformed to the frequency domain,

$$R(t) = \sum_{k=-\infty}^{\infty} r(\omega_k) e^{i\omega_k t}, \quad (3.14)$$

where $r(\omega)$ is the amplitude of the radius at frequency ω . Similarly:

$$P_\infty(t) = P_3(x_3) = \sum_{k=-\infty}^{\infty} p_3(\omega_k) e^{i\omega_k t}, \quad (3.15)$$

where $p_3(\omega)$ is the amplitude of the pressure at frequency ω at the position x_3 . In the notation we suppress the explicit dependance on ω_k for compactness of formulation. Upon linearization, the Rayleigh-Plesset equation (5.32) becomes:

$$-\omega^2 r = \frac{1}{R_0 \rho} \left(-r \left(P_0 + \frac{2\sigma}{R_0} - P_v \right) \left(\frac{3\gamma}{R_0} \right) + r \frac{2\sigma}{R_0^2} - \frac{4\mu i \omega r}{R_0} - p_3 \right). \quad (3.16)$$

The volume change of the bubble and thus the ink flow towards the position of the bubble center is:

$$Q_b(t) = -\frac{d}{dt} \left(\frac{4}{3} \pi R(t)^3 \right) = \sum_{k=-\infty}^{\infty} q_b(\omega_k) e^{i\omega_k t} \quad (3.17)$$

where $q_b(\omega)$ is the amplitude of the volume flow rate into bubble at frequency ω . Combining equations 3.16 and 3.17 yields an expression for the amplitude of the volume flow rate.

$$q_b = -4\pi i p_3 R_0^2 \omega \left(R_0 \rho \omega^2 - \left(P_0 + \frac{2\sigma}{R_0} - P_v \right) \left(\frac{3\gamma}{R_0} \right) + \frac{2\sigma}{R_0^2} - \frac{4\mu i \omega}{R_0} \right)^{-1}. \quad (3.18)$$

When inertia, vapor pressure, viscosity, and surface tension are neglected, equation (3.18) reduces to the expression for the disk bubble in De Jong et al. [19]. This shows that the dynamics obtained for the disk bubble in ref. [19] can be alternatively derived from the Rayleigh-Plesset equation.

3.4.5 Model Results

The model described in this section was developed to test the hypothesis that the two-way coupling between the bubble dynamics and channel acoustics is essential. The modification of the pressure fluctuation at the entrance of the nozzle by the bubble is significant, as shown in figure 3.6 for a bubble of $R_0 = 23 \mu m$, driven at 80 V.

The pressure fluctuations are reduced by a factor of 4 when a bubble is present. It is this pressure reduction which causes the nozzle to stop jetting droplets. Not only the pressure amplitude is reduced, also the higher frequencies in the signal are damped. This becomes evident when looking at the transfer function of the actuator voltage to the velocity in the nozzle, as shown in figure 3.7.

The velocity in the nozzle is reduced and the resonance peaks at 50 kHz and 110 kHz are shifted to 20 kHz and 60 kHz, respectively. Moreover, the higher frequencies are completely damped by the air bubble. The zeros in the transfer function are not shifted since they are caused by the properties of section 1. The zeros occur at frequencies $f = n \frac{c_{eff,1}}{l_1}$, where n is an integer.

The change in pressure fluctuation that the bubble experiences is accompanied by a change in bubble radius oscillation, as shown in figure 3.8. Here the bubble radius is shown, calculated with the described model, and calculated when neglecting the two-way coupling. Through the channel acoustics, the bubble loses energy, thus reducing the amplitude of the volume oscillations. When this effect is neglected, the bubble is driven beyond the linear regime, and the linearization is not justified. The bubble oscillations without two-way coupling

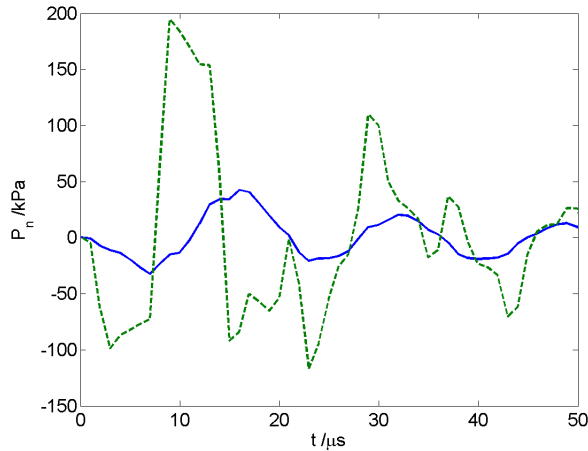


Figure 3.6: Pressure at the entrance of the nozzle $P_3(x_3)$ with (solid), and without (dashed) an entrained bubble of $R_0 = 23 \mu m$, as calculated by the model for a 2 – 4 – 2 pulse (2 μs rise time, 4 μs plateau, and 2 μs fall time), applied at 80 V. The pressure peak that starts at 10 μs would normally cause the formation of a droplet. With an entrained air bubble, this peak is reduced by a factor of four. The pressure reduction due to the bubble is strong enough to prevent the droplet formation.(color online)

were thus calculated with the full (nonlinear) Rayleigh-Plesset equation, equation 3.12, driven by the pressure that would occur in the absence of a bubble, see figure 3.6. As seen from figure 3.8, the effect of the two-way coupling is significant, and cannot be neglected.

The FFT is calculated from the oscillations of the $R_0 = 23 \mu m$ bubble and displayed in figure 3.9. The main frequency is 60 kHz. The same frequency is also found for the bubble of $R_0 = 18 \mu m$. This frequency does not depend on the bubble radius once it has reached a certain size. The reason for this is that once the bubble is large enough, it fully reflects the acoustic waves, acting like an open end of section 3 of the channel and decoupling it from the nozzle (section 4).

Air bubbles can be detected by monitoring the electric current through the piezo in the time domain, as it reacts to pressure fluctuations. This detection method has been described by de Jong et al. [8]. The proposed model predicts the changes in this signal due to the entrained air bubble, as shown in figure 3.10, for the system considered by de Jong et al [8]. This printhead has an 8 mm actuation channel and a 50 μm trumpet shaped nozzle. A 5 – 6 – 3 (5 μs rise time, 6 μs plateau, and 3 μs fall time) trapezoidal pulse is employed, at a voltage of 44 V. The bubble is placed at the nozzle entrance, and has a radius of $R_0 = 23 \mu m$.

In the first part the piezo is deformed by the pulse. After $t = 15 \mu s$, the piezo reacts to the pressure fluctuations in the ink channel. Since our interest is focused on the acoustical signal from the piezo, the scale on the vertical axis is chosen such that the pressure change in the ink channel and its modification due

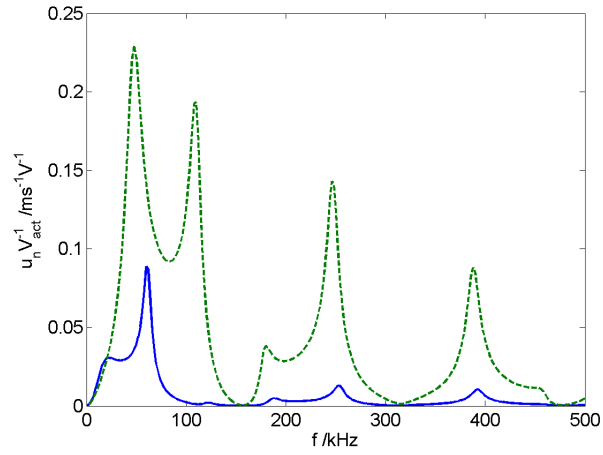


Figure 3.7: Transfer function amplitude of velocity in the nozzle over actuator voltage, with (solid) and without (dashed) an entrained bubble with a radius $R_0 = 23 \mu\text{m}$. Note the large reduction of the velocity, in particular at higher frequencies. The individual peaks are shifted as a result of the modification of the reflection at the nozzle. The bubble has a significant influence on the channel acoustics.(color online)

to the bubble are resolved. The air bubble causes the signal to have a higher amplitude, a faster oscillation, and less high frequency fluctuation.

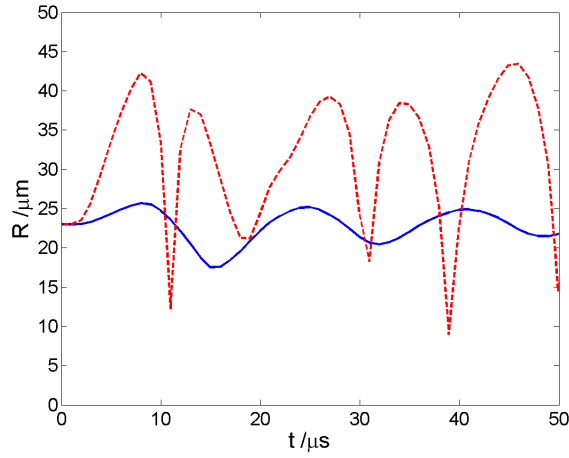


Figure 3.8: The bubble radius, neglecting the two-way coupling between bubble volume fluctuation and pressure (dashed), and with this two-way coupling taken into account (solid). The case with two-way coupling is calculated with the linearized analysis as described in the text for a trapezoidal 2-4-2 pulse and a driving of 80 V. The case where two-way coupling is neglected is calculated with the nonlinear Rayleigh-Plesset equation because in this case the bubble is driven beyond the linear regime. This is most evident in the violent collapse near $t = 10 \mu s$, where the bubble is compressed within 3 μs from 48 μm to 10 μm . (color online)

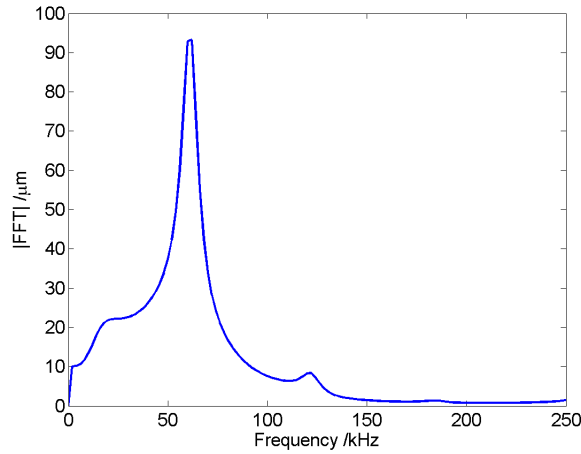


Figure 3.9: The FFT calculated from the bubble oscillations for the case of figure 3.8 with two-way coupling. The main frequency is $f = 60 kHz$. For this bubble radius, $R_0 = 23 \mu m$, the bubble reflects the acoustic waves in the ink channel. Therefore, the closed end (the nozzle) is replaced by an open end (the bubble). (color online)

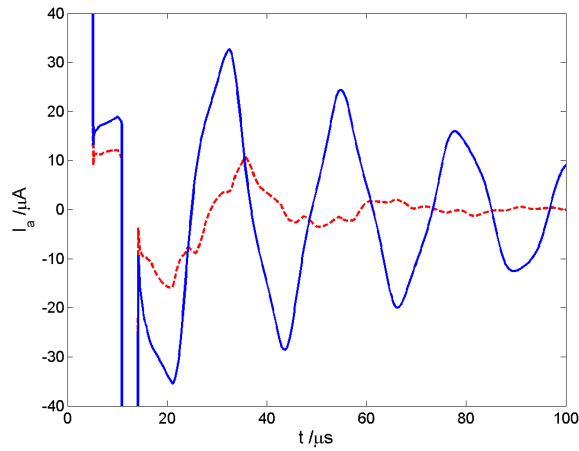


Figure 3.10: Piezo current with (solid) and without (dashed) an entrained air bubble of $23 \mu\text{m}$ radius. The printhead has an 8 mm actuation channel, a $50 \mu\text{m}$ trumpet shaped nozzle and is driven at 44 V with a $5 - 6 - 3$ ($5 \mu\text{s}$ rise time, $6 \mu\text{s}$ plateau, and $3 \mu\text{s}$ fall time) trapezoidal pulse. The signal is divided into two parts: first ($0 < t < 15 \mu\text{s}$), the piezo is deformed by a 44 V voltage, in the second part ($15 < t < 100 \mu\text{s}$), the piezo is only deformed by the pressure changes in the ink channel. Without a bubble, the piezo current is small after $t = 50 \mu\text{s}$. The bubble however reflects the acoustic waves travelling towards the nozzle. Since most damping is caused by the nozzle, the acoustic waves remain in the ink channel for a relatively long time. (color online)

3.5 Comparison between model and experiment

To compare the experimental data with the bubble model, the experimentally obtained equilibrium radius of the bubble is used in the model. A quantitative comparison can be seen in figure 3.11 for the 120 V and the 190 V driving. As mentioned before, only the amplitude of the acoustic pressure for a driving of 190 V is adjusted to the pressure in the experiments so that for a bubble of $R_0 = 23 \mu m$ the amplitude of the bubble oscillations fits to the experiment: The driving of 190 V in the experiments is found to be a driving of 80 V in the model. The difference in driving is assumed to be caused by the properties of the piezo, in particular the value of α_1 . Upon adjusting this absolute size, a good agreement of the shape of the signal can be seen, showing the importance of the confined geometry in our printhead channel. In particular, the relatively small expansion of the bubble compared to its large compression is well captured. After about $t = 30 \mu s$, the model slightly deviates from the experimental data. This is assumed to be due to the absence of thermal damping in the model, which is known to be relevant for bubbles of this size [20], in particular in closed systems [24].

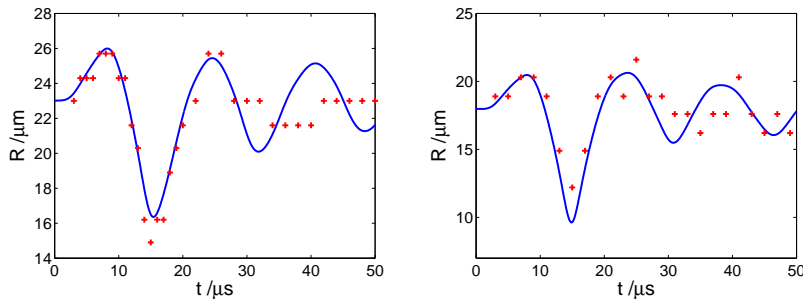


Figure 3.11: Comparison of the experimental bubble oscillations (crosses) with the numerical model (solid line). The air bubble of $R_0 = 23 \mu m$ (left) and $R_0 = 18 \mu m$ (right) is driven at 190 V (left) and at 120 V (right). The model driven at 80 V (left) and 51 V (right) captures the details of the initial expansion and the compression of the bubble. After $t = 30 \mu s$, the model deviates from the bubble oscillations. (color online)

The frequency spectrum (Fast Fourier Transform) is compared in figure 3.12. The bubble radius is $R_0 = 23 \mu m$ in the experiments and in the model. The main frequency component found in the experiments is 60 kHz, as in the model.

3.6 Conclusions and outlook

When an air bubble is entrapped in the ink channel, it grows by rectified diffusion up to some saturation size. The oscillations of this bubble of saturated size are measured and modelled. Due to the confined space the bubble acts back on the acoustic waves. It is this two-way coupling between the bubble and the channel acoustics results in the equilibrium size of the bubble. By employing a

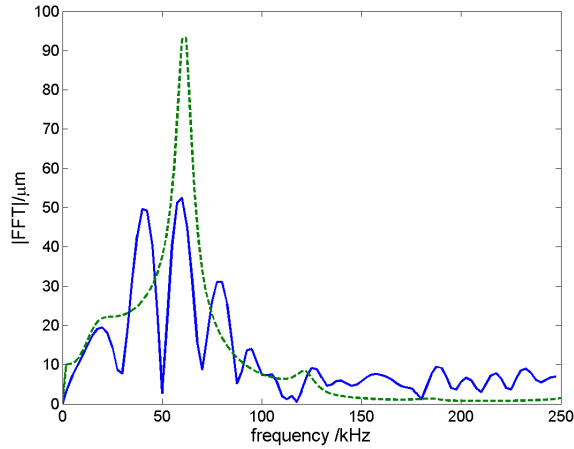


Figure 3.12: The Fast Fourier Transform (FFT) of the bubble oscillations in the experiments (dashed) and for the model (solid), for a bubble size of $R = 23 \mu m$ radius. The main frequency component at $f = 60 kHz$ agrees reasonably well. (color online)

glass window the oscillations are measured with high speed imaging. The channel acoustics and bubble dynamics are modelled with a one-dimensional model. This model incorporates coupling between the bubble and the ink channel. The bubble itself is modelled with a linearized Rayleigh-Plesset equation. It turns out that the confined geometry and therefore the two-way coupling is crucial. The result is a simple model that can be employed to study air bubble behavior and predict the effect of an entrapped air bubble on the acoustic field in the channel. In this way, air bubbles can be studied for different channel properties, $A_{0,j}$, l_j , α_j , β_j and acoustic driving protocols.

Appendix A.1: Nozzle representation

Conical nozzle representation

This appendix deals with the representation of the conical nozzle used in the experiments through the cylindrical nozzle that is employed in the model. A sketch of experimental nozzle and its cylindrical representation is shown in figure 3.13.

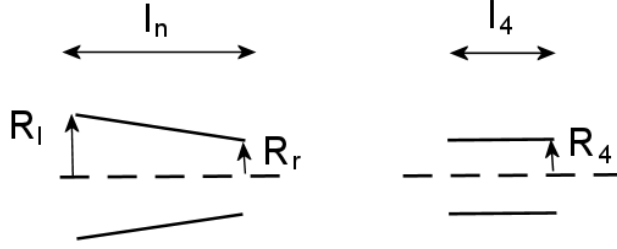


Figure 3.13: Left, the experimental nozzle, $R_l = 25 \mu m$, $R_r = 15 \mu m$, and $l_n = 70 \mu m$. Right, the cylindrical nozzle representation employed in the model, $R_4 = 15 \mu m$, and $l_4 = 42 \mu m$.

Two nozzle properties are important: the viscous friction on the walls, and the acoustic properties. The experimental nozzle can be described as a cylinder with an equivalent diameter and length. The equivalent diameter of the model nozzle, $d_4 = 2R_4$, is chosen equal to the minimum experimental nozzle diameter $30 \mu m$ in order to match the viscous friction in the nozzle. Now the correct equivalent length, l_4 , has to be determined based on the acoustic properties.

The volume flow rate of ink through the nozzle, Q_n , is defined as

$$\int_{A_n} u_n dA = Q_n = \sum_{k=-\infty}^{\infty} q_n(\omega_k) e^{i\omega_k t}, \quad (3.19)$$

where q_n is the amplitude of the volume flow rate through the nozzle.

The pressure can be obtained by integrating the linearized momentum equation over the axial coordinate

$$\partial_t u_j = \frac{-1}{\rho} \partial_x P_j \Rightarrow P_n(x) = P_n(x_3) + \int_{x_3}^x i\rho\omega \frac{q_n}{A_n(x)} dx. \quad (3.20)$$

Transforming P_n to the frequency domain gives

$$P_n = \sum_{k=-\infty}^{\infty} p_n(\omega_k) e^{i\omega_k t}. \quad (3.21)$$

After solving for the admittance (the volume flow divided by the pressure see e.g. [25, 26]) and imposing zero pressure at the meniscus one gets

$$\frac{q_n}{p_n} = \frac{-1}{i\rho\omega \int_0^{l_n} \frac{1}{A_n(x)} dx} \quad (3.22)$$

Equation (3.22) is a general solution depending on the geometry of the nozzle. This equation will now be evaluated for different nozzles and the glass connection channel.

The nozzle radius of the experimental conical nozzle is described by

$$R_n(x) = R_l \left(1 - \frac{x}{l_n}\right) + R_r \frac{x}{l_n} \quad (3.23)$$

R_l is the entrance radius (25 μm), and R_r is the exit nozzle radius (15 μm). The length of the experimental nozzle is $l_n = 70 \mu m$. Inserting eq. (3.23) into eq. (3.22) results in:

$$\frac{q_n}{p_n} = \frac{-\pi}{i\rho\omega \int_0^{l_n} \frac{1}{(R_l(1-\frac{x}{l_n})+R_r\frac{x}{l_n})^2} dx} = \frac{-\pi R_l^2}{i\rho\omega l_n \int_0^1 \frac{1}{(1+(\frac{R_r}{R_l}-1)x)^2} dx} \quad (3.24)$$

By evaluating the integral, the admittance of the experimental conical nozzle is obtained as

$$\frac{q_n}{p_n} = \frac{-\pi R_l R_r}{i\rho\omega l_n} \quad (3.25)$$

For the cylindrical nozzle of section 4, the admittance is

$$\frac{q_4}{p_n} = \frac{-\pi(R_4)^2}{i\rho\omega l_4}. \quad (3.26)$$

If we now match the admittance of the experimental nozzle and the modelled cylinder, we can calculate the equivalent length l_4 of the nozzle based on the minimum radius, $1/2d_4 = R_4 = R_r = 15 \mu m$.

$$\frac{q_4}{p_n} = \frac{-\pi(R_4)^2}{i\rho\omega l_4} = \frac{-\pi R_l R_r}{i\rho\omega l_n} \quad (3.27)$$

The equivalent length for the cylindrical nozzle is found to be:

$$l_4 = \frac{R_4^2}{R_l R_r} l_n = 42 \mu m. \quad (3.28)$$

Trumpet shaped nozzle representation

The nozzle considered for the calculation of the electric current through the piezo in figure 3.10 is a trumpet shaped nickel nozzle. A sketch of the experimental nozzle and the nickel nozzle is depicted in figure 3.14.

We describe the radius of the trumpet-shape nozzle of figure 3.14 by

$$R_n(x) = R_l - l_n \sqrt{1 - \left(1 - \frac{x}{l_n}\right)^2} \quad (3.29)$$

The trumpet shaped nozzle is specified by two parameters: the nozzle length $l_n = 50 \mu m$ and the ratio $\lambda = \frac{R_l}{l_n}$ where $R_l = 65 \mu m$ is the entrance radius. The smallest radius is $R_n(l_n) = R_r = R_l - l_n = 1/2d_4 = 15 \mu m$, and this is the radius at the meniscus. The radius is plotted as a function of x in figure 3.15.

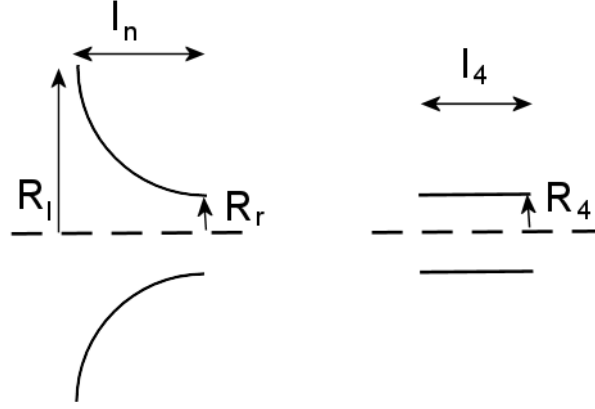


Figure 3.14: Left, the experimental nozzle, $R_l = 65 \mu m$, $R_r = 15 \mu m$, and $l_n = 50 \mu m$. Right, the cylindrical nozzle representation employed in the model, $R_4 = 15 \mu m$, and $l_4 = 26 \mu m$.

Insert this nozzle shape into equation (3.22) to obtain the admittance of the trumpet shaped nozzle:

$$\frac{q_n}{p_n} = \frac{-\pi l_n}{i\rho\omega} \frac{2(-1 + \lambda^2)^{\frac{3}{2}}}{\pi + 2 \arctan\left(\frac{1}{\sqrt{-1 + \lambda^2}}\right) + 2\sqrt{-1 + \lambda^2}} \quad (3.30)$$

This admittance is equal to the admittance of a cylindrical nozzle whose radius is equal to R_r and whose length is:

$$l_4 = l_n \frac{(\lambda - 1)^2}{F(\lambda)} \quad (3.31)$$

with $F(\lambda)$ equal to the second fraction on the right-hand side of equation (3.30).

Therefore, the equivalent cylinder has a diameter of $d_4 = 30 \mu m$ and a length of $l_4 = 26 \mu m$.

Appendix A.2: Glass connection channel representation

The method used to obtain equivalent cylindrical nozzles is also applied to the glass connection channel. The shape of the connection channel is approximately:

$$R_c(x) = R_{max} - (R_{max} - R_{min}) \left(\sin \frac{\pi x}{l_g} \right)^2 \quad (3.32)$$

where l_g is the length of the glass connection channel, R_{max} is the maximum channel radius, and R_{min} is the minimum channel radius. The approximated shape of Equation (3.32) is plotted in figure 3.16.

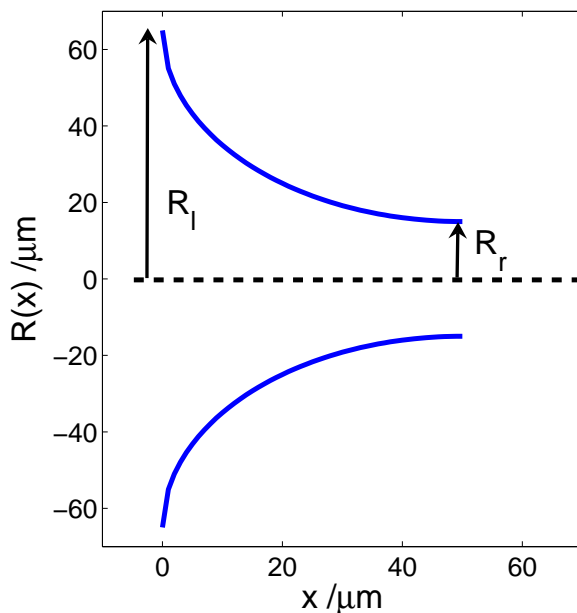


Figure 3.15: The approximation of the experimental nozzle radius. (color online)

Insert the channel cross-sectional area based on this radius into equation (3.22) to obtain:

$$\frac{q_g}{p_g} = \frac{-\pi R_{max}^2}{i\omega\rho l_g} \frac{2(1-\kappa)^{\frac{3}{2}}}{2-\kappa} \quad (3.33)$$

where p_g is the amplitude of the pressure drop over the glass connection channel, q_g is amplitude of the volume flow rate through the glass connection channel, and

$$\kappa = \frac{R_{max} - R_{min}}{R_{max}} = \frac{125 \cdot 10^{-6} - 40 \cdot 10^{-6}}{125 \cdot 10^{-6}} = 0.68 \quad (3.34)$$

The equivalent cylindrical connection channel with diameter $d_3 = 80 \mu m$ has a length of $l_3 = 149 \mu m$. The admittance of the glass connection channel and the conical nozzle can be compared to obtain an estimate of the relative influence of the connection channel. The conical nozzle is approximated by a cylindrical nozzle of $d_4 = 15 \mu m$, and equivalent length of $l_4 = 42 \mu m$. The maximum glass channel radius is $R_{max} = 125 \mu m$ and the channel length is $l_g = 400 \mu m$. The pressure drop ratio is $\frac{p_g}{p_n} = 0.5$. The pressure drop over the connection channel is significant, with respect to the pressure drop over the nozzle.

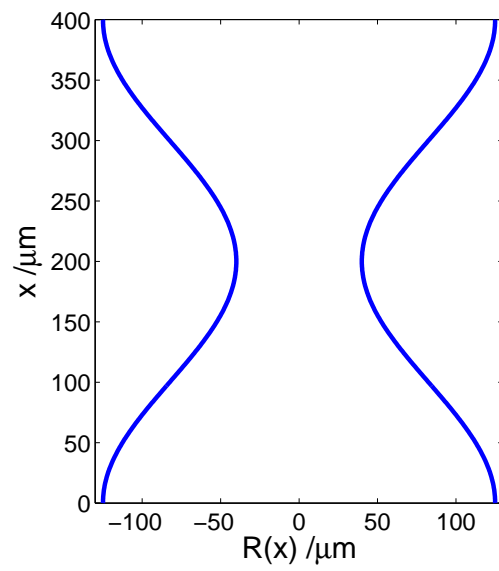


Figure 3.16: The approximation of the hour glass shape of figure 3.1. (color online)

Bibliography

- [1] H. P. Le, *Progress and trends in ink-jet printing technology*, J. Imag. Sci. Tech **42**, 49 (1998).
- [2] C. Williams, *Ink-jet printers go beyond paper*, Phys. World **19**, 24 (2006).
- [3] H. S. Koo, M. Chen, and P. C. Pan, *LCD-based color filter films fabricated by a pigment-based photo resist inks and printing technology*, Thin Solid Films **515**, 896 (2006).
- [4] O. A. Basaran, *Small-scale free surface flows with breakup: Drop formation and emerging applications*, AIChE J. **48**, 1842 (2002).
- [5] J. F. Dijksman, *Hydrodynamics of small tubular pumps*, J. Fluid Mech. **139**, 173 (1984).
- [6] J. D. Brock, I. M. Cohen, I. P. Ivanov, H. P. Le, and J. Roy, *Oscillations of an air bubble in an ink jet*, J. Imaging Sci. Technol. **10**, 127 (1984).
- [7] N. P. Hine, *Deaeration system for a high-performance drop-on-demand ink jet*, J. Imaging Technol. **17**, 223 (1991).
- [8] J. de Jong, H. Reinten, M. van den Berg, H. Wijshoff, M. Versluis, G. de Bruin, and D. Lohse, *Air entrapment in piezo-driven inkjet printheads*, J. Acoust. Soc. Am., **120**, 1257 (2006).
- [9] M. M. Fyrillas and A. J. Szeri, *Dissolution or growth of soluble spherical oscillating bubbles*, J. Fluid Mech. **277**, 381 (1994).
- [10] S. Hilgenfeldt, D. Lohse, and M. P. Brenner, *Phase diagrams for sonoluminescing bubbles*, Phys. Fluids **8**, 2808 (1996).
- [11] C. Caskey, D. Kruse, P. Dayton, T. Kitano, and K. Ferrara, *Microbubble oscillation in tubes with diameters of 12, 25, and 195 microns*, Appl. Phys. Lett. **88**, 033902 (2006).
- [12] P. Zhong, Y. Zhou, and S. Zhu, *Dynamics of bubble oscillation in constrained media and mechanisms of vessel rupture in SWL*, Ultrasound in Med. & Biol., **27** (1), 119 (2001).
- [13] E. Sassaroli and K. Hynynen *Resonance frequency of microbubbles in small blood vessels: a numerical study*, Phys. Med. Biol., **50** (22), 5293 (2005).

- [14] S. Qin and K. Ferrara The natural frequency of nonlinear oscillation of ultrasound contrast agents in microvessels, *Ultrasound in Med. & Biol.*, **33**(7), 1140 (2007).
- [15] S. Qin, Y. Hu, and Q. Jiang *Oscillatory Interaction Between Bubbles and Confining Microvessels and Its Implications on Clinical Vascular Injuries of Shock-Wave Lithotripsy*, *IEEE Trans. Ultras. Ferr. Freq. Contr.*, **53** (7), 1322 (2006).
- [16] E. Ory, H. Yuan, A. Prosperetti, S. Popinet, and S. Zaleski Growth and collapse of a vapor bubble in a narrow tube, *Phys. Fluids* **12** (6), 1268 (2000).
- [17] H. Yuan, H. Oguz, and A. Prosperetti *Growth and collapse of a vapor bubble in a small tube*, *Int. J. Heat Mass Transfer*, **42** (1999).
- [18] J. Cui, M. Hamilton, P. Wilson, and E. Zabolotskaya Bubble pulsations between parallel plates, *J. Acoust. Soc. Am.* **119** (4), 2067 (2006).
- [19] J. de Jong, R. Jeurissen, H. Borel, M. van den Berg, H. Wijshoff, H. Reintjen, M. Versluis, A. Prosperetti, and D. Lohse, *Entrapped air bubbles in piezo-driven inkjet printing: Their effect on the droplet velocity*, *Phys. Fluids*, **18**, 121511 (2006).
- [20] C. E. Brennen, *Cavitation and Bubble Dynamics* (Oxford University Press, Oxford, 1995).
- [21] H. Tijdeman, *On the propagation of sound waves in cylindrical tubes*, *J. Sound and Vibr.* **39**, 1 (1975).
- [22] H. N. Oğuz and A. Prosperetti, *The natural frequency of oscillation of gas bubbles in tubes*, *J. Acoust. Soc. Am.* **103**, 3301 (1998).
- [23] J. R. Womersley, *Method for the calculation of velocity, rate of flow and viscous drag in arteries when the pressure gradient is known*, *J. Physiol.* **127**, 553 (1955).
- [24] X. M. Chen and A. Prosperetti, *Thermal processes in the oscillations of gas bubbles in tubes*, *J. Acoust. Soc. Am.* **104**(3), 1389 (1998).
- [25] J. Billingham and A. C. King, *Wave motion* (Cambridge University Press, Cambridge, 2000).
- [26] J. Lighthill, *Waves in fluids* (Cambridge University Press, Cambridge, 1978).

Chapter 4

Acoustic measurement of bubble size in an inkjet printhead ¹

The volume of a bubble in a piezo inkjet printhead is measured *acoustically*. The method is based on a numerical model of the investigated system. The piezo not only drives the system, but it is also used as a sensor by measuring the current it generates. The numerical model is used to predict this current for a given bubble volume. The inverse problem is to infer the bubble volume from an experimentally obtained piezo current. By solving this inverse problem, the size and position of the bubble can thus be measured acoustically. The method is experimentally validated with an inkjet printhead that is augmented with a glass connection channel, through which the bubble was observed optically, while at the same time the piezo current was measured. The results from the acoustical measurement method correspond closely to the results from the optical measurement.

4.1 Introduction

The dynamics of a sound driven free bubble in infinite volume is well described by the Rayleigh-Plesset equation [1–3], whose validity even under the extreme conditions of single bubble sonoluminescence has been thoroughly established [4]. However, many important cases of bubble dynamics occur under constraint conditions, in finite volumes of liquid, rather than infinite volumes, such as in confined spaces and near a wall [5–8]. Examples include the behavior of gas bubbles in blood vessels, aiming at improving ultrasound diagnostics and treatment [9], or thermal inkjet printing and other microfluidic applications, where bubbles are used as actuators [10, 11]. However, bubbles can also disrupt

¹Published as: Roger Jeurissen, Arjan van der Bos, Hans Reinten, Marc van den Berg, Herman Wijshoff, Jos de Jong, Michel Versluis, Detlef Lohse, *Acoustic measurement of bubble size in an inkjet printhead*, J. Acoust. Soc. Am. (in press).

the operation of the printhead as was shown in earlier research [12–14]. Although inkjet printing is a robust process and billions of droplets can be printed without problems, there is a small chance that during actuation a small air bubble is entrapped at the nozzle of an ink channel. The bubble influences the channel acoustics, reducing the pressure buildup at the nozzle. The bubble grows by rectified diffusion until it reaches a diffusive equilibrium [12–14]. At this size, the pressure buildup at the nozzle is insufficient for droplet production, so that the nozzle fails. This malfunctioning can be detected acoustically [13], but until now the relation between bubble size and channel acoustics has not been shown quantitatively. In fact in many studies the bubble was assumed to behave as if it were in an unbounded liquid [15, 16].

The dynamics of a bubble in confined space is fundamentally different from that in an infinite volume of liquid where the far field is three dimensional. In contrast, in a compressible inviscid liquid, the far field of a bubble between two parallel infinite walls is two dimensional [17], and the far field of a bubble in an infinitely long pipe is one dimensional [18–20]. An incompressible liquid does not allow bubble volume fluctuations in either confined space, while the volume fluctuations in an unbounded volume of liquid are possible and governed by the Rayleigh-Plesset equation. Models that assume an unbounded volume of liquid are therefore inappropriate for a bubble in a confined space.

In this study, a model is used that captures the effect that a bubble has on the channel acoustics and vice versa. To validate the model, experimental results are presented which correlate the acoustic change inside the channel with optical measurements of an entrained air bubble.

4.2 Geometry of the inkjet printhead

The inkjet printhead that is used in this research is developed by Océ Technologies B.V. This experimental printhead consist of 256 similar ink channels where each channel has a rectangular shape and a length of 10 mm. A 8 mm long piezo element is placed onto the channel. This piezo generates the acoustic waves by applying a trapezoidal pulse of 13 μs (4 μs rise time, 5 μs plateau, 4 μs fall time) [21]. The generated waves travel through the channel and are reflected at the ink reservoir at one side, and at the nozzle at the other side. The result is a velocity and pressure build up at the nozzle which leads to a droplet being ejected [22, 23]. Typically, droplets of 30 pl are generated at a rate of 20 kHz with a velocity of 6 m/s.

To visualize the dynamics of the entrained air bubble, a 400 μm long glass connection channel [24] was interposed between the ink channel and the nozzle plate (figure 4.1), similarly as done in reference [13]. This channel was made by powder blasting which resulted in an hourglass shape with a waist diameter of 220 μm and a maximum diameter of 300 μm at the ends. In figure 4.2 the connection channel with an air bubble inside is shown. On top of the connection channel, a 100 μm thick nickel nozzle plate is glued. The trumpet shaped nozzles have a diameter of 30 μm at the exit and 130 μm at the inlet.

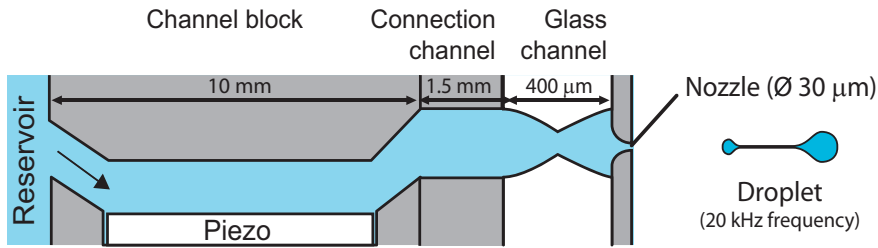


Figure 4.1: The channel inside the printhead is about 10 *mm* long and is actuated by a 8 *mm* long piezo. In between the channel block and the nozzle plate a 400 μm long glass connection channel is placed through which the bubble dynamics can be observed.

4.3 Experimental parameters

Besides visualizing the bubble dynamics, also the pressure variations inside the channel were measured. This was done by measuring the piezo current. This technique [25] has earlier been applied in [13]. Even small pressure fluctuations in the channel result in measurable current from the piezo. As this signal is only measured in between the actuation pulses, the time window where the current can be measured is 30 μs at a droplet production rate of 20 *kHz*. An example of this piezo current is shown in figure 4.3. This figure illustrates that the acoustic signal changes significantly when the channel acoustics are disturbed by air entrapment.

In this study, the piezo current was measured at a range of bubble volumes. To accomplish this, air entrapment was induced by physically blocking a channel while actuating. The actuation was continued until the entrapped bubble reached its diffusive equilibrium size, which is about 120 *pl*. Then, the actuation was stopped allowing the bubble to dissolve. The bubble dissolves at a rate of approximately 0.5 *pl/s*, so it takes about 4 minutes for a 120 *pl* bubble to fully dissolve. During the dissolution of the bubble, piezo current data were gathered by actuating at a frequency of 1 *Hz*. At this reduced actuation rate, rectified diffusion is not strong enough to sustain the bubble, so it dissolves. One microsecond before every actuation pulse, an image of the bubble was captured. In this way, motion blur due to volume oscillations was prevented.

4.4 Modeling the printhead

Deformation of a piezo gives rise to a deformation current I from the actuator. Such a deformation can be caused by varying the voltage over the electrodes. Thanks to this effect, the piezo can be used as an actuator. Another way in which the piezo can be deformed is caused by acoustic waves in the channel. Therefore the piezo element can be used also as a sensor. The piezo current is calculated by using the model developed in reference [14], which links the Rayleigh-Plesset equation to the equations that govern the propagation of acoustic waves in a viscous medium in a flexible pipe and the response of the piezo and channel to the actuator voltage.

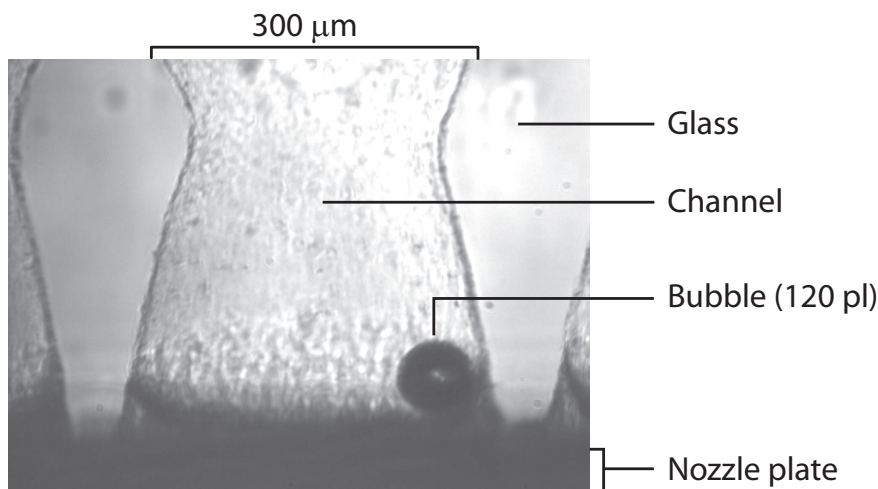


Figure 4.2: An optical measurement showing an entrapped air bubble in the glass connection channel. While actuating, the fully grown air bubble will just remain oscillating in the channel indefinitely. Note the position of the air bubble: due to the secondary Bjerknes force it is pushed against the glass wall where it stays fixed even after the actuation is stopped. On the left and right sides of the channel the neighboring channels can also be seen.

Acoustically, the print head consists of four linked sections of pipes as shown in figure 4.4. The properties of the channel are constant over each section. The relevant properties are the piezo electric expansion coefficient α_j , the wall flexibility β_j , the cross sectional area A_j , the velocity of sound in the liquid c , the liquid density ρ , the viscosity μ , and the length L_j of the channel section. The piezo electric expansion coefficient is defined as

$$\alpha \equiv \frac{1}{A} \left(\frac{\partial A}{\partial U} \right)_P, \quad (4.1)$$

where U is the voltage over the electrodes of the piezo element and P is the pressure in the channel. The wall flexibility is defined as

$$\beta \equiv \frac{1}{A} \left(\frac{\partial A}{\partial P} \right)_U. \quad (4.2)$$

These quantities can be determined with a solid mechanics calculation, provided that the geometry and material parameters are accurately known. They can also be determined by measuring the piezo current in the absence of a bubble.

The analysis is performed in the frequency domain. The discrete Fourier transform is defined through

$$f(t) = \sum_j F(\omega_j) e^{i\omega_j t}, \quad (4.3)$$

where $f(t)$ is the relevant quantity in the time domain, and $F(\omega)$ is the same quantity in the frequency domain. The explicit dependence on frequency not

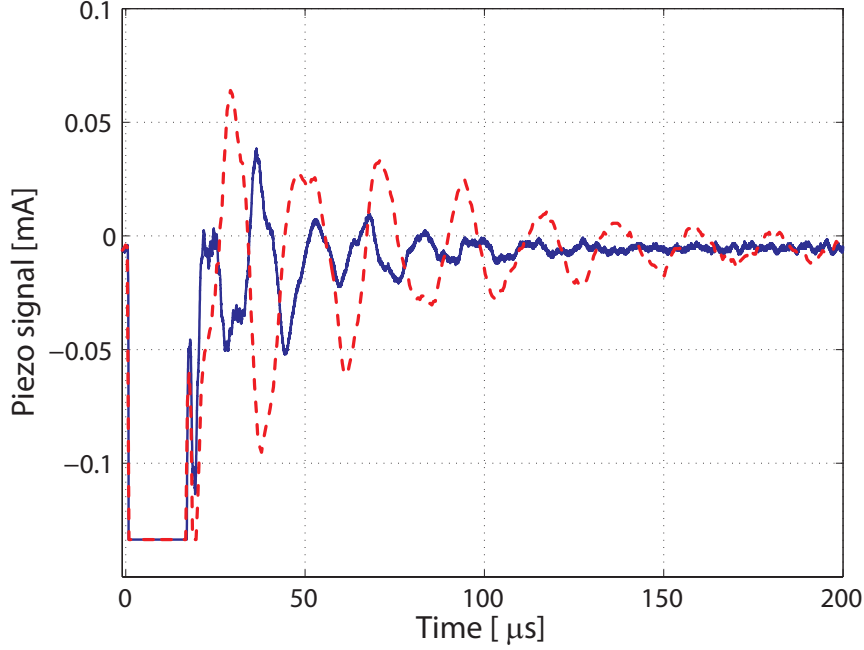


Figure 4.3: Piezo current of a normal operating nozzle (solid), and with an entrained air bubble with a volume of $V_b = 80 \text{ pl}$ (dashed) close to the nozzle plate. It can be seen in this figure that the volume oscillations of the entrapped bubble modify the piezo current significantly; the piezo current amplitude is less damped and the main frequency decreases.

spelled out for the remainder of the paper for the sake of brevity. The pressure P is decomposed into the waves propagating to the left P_l and right P_r . For each channel section, the amplitudes of the left and right propagating waves are calculated per frequency,

$$P = \sum_j P_r e^{i(\omega_j t - kx)} + P_l e^{i(\omega_j t + kx)} + P_s. \quad (4.4)$$

The pressure P_s due to the actuator depends only on the imposed actuator voltage. The wave number k is a complex quantity due to viscous dissipation. For a cylindrical pipe, a closed form expression can be obtained analytically [26], namely

$$k = \frac{\omega}{c_{eff}} \sqrt{\frac{1}{1 + \frac{2\sqrt{i}J_1(Wo i^{\frac{3}{2}})}{Wo J_0(Wo i^{\frac{3}{2}})}}}. \quad (4.5)$$

The functions J_0 and J_1 are the ordinary Bessel functions of the first kind, of zeroth and first order, respectively. The Womersley number Wo is the ratio of the inertia of the oscillating velocity field over the viscosity,

$$Wo_j = \frac{1}{2} d_j \sqrt{\frac{\omega \rho}{\mu}}, \quad (4.6)$$

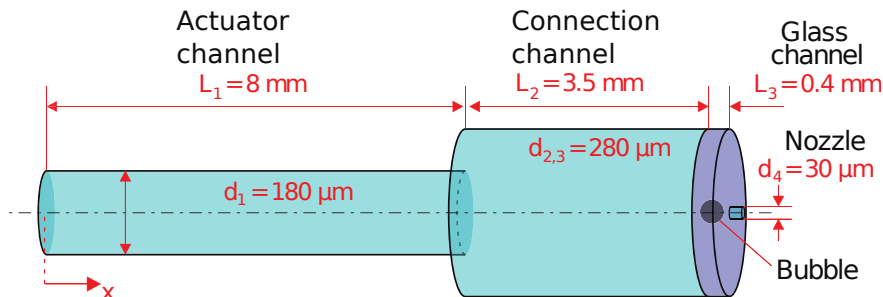


Figure 4.4: The print head as it is implemented in the model. From left to right: actuator channel, connection channel, glass connection channel and nozzle.

where d_j is the diameter of the section. The effective wave velocity is the inviscid phase velocity of acoustic waves. This quantity differs from the velocity of sound due to wall flexibility. It was derived by Young [27] and is given by

$$c_{eff} = \sqrt{\frac{c^2}{1 + \beta c^2 \rho}}. \quad (4.7)$$

The effective wave velocity is equal to the velocity of sound c , if the wall flexibility β vanishes, and smaller for nonzero wall flexibility. The wave number (4.5) has been the main result of the acoustical model [26]. The boundary conditions are continuity of pressure and volume flow rate. Equation (4.4) for the pressure, equation (4.5) for the wave number, and the boundary conditions describe the propagation of acoustic waves in a flexible channel filled with a viscous liquid.

Electrically, the piezo actuator is a capacitor in parallel with a variable current source. The piezo current depends on the capacitance of the actuator C_a , the coupling coefficient α , and the pressure in the channel. The coupling coefficient relates the voltage over the piezo to the deformation of the channel and has also been used in the calculation of the channel acoustics. The time derivative of the charge expresses the relation between the actuator voltage and the piezo current I ,

$$I = \frac{dQ}{dt} = \left(\frac{\partial Q}{\partial U} \right)_P \frac{dU}{dt} + \left(\frac{\partial Q}{\partial P} \right)_U \frac{dP}{dt}. \quad (4.8)$$

Here Q is the total charge on the piezo actuator and U the voltage over the piezo actuator. To calculate or interpret the piezo current, the isobaric capacitance and the relation between the channel pressure and current have to be determined. The isobaric capacitance is measured directly. The piezo current due to pressure fluctuations can be calculated from the thermodynamic fundamental equation of the actuator channel. The differential of the energy per unit length of channel is given by,

$$de = P dA + U dq, \quad (4.9)$$

where q is the charge per unit length and e is the energy of the channel per unit length. Note that only the structure is considered in this section.

The analysis is simplified when the Legendre transform [28] with respect to pressure and actuator voltage is used, because the mechanical properties of the channel are known in terms of the pressure and actuator voltage as independent parameters. The differential of the Legendre transform g (Gibbs the free energy per unit length) is

$$dg = de - d(AP) - d(Uq) = -A dP - q dU. \quad (4.10)$$

The isobaric capacitance is defined as the second derivative,

$$C_P \equiv \left(\frac{\partial Q}{\partial U} \right)_P = L_a \left(\frac{\partial q}{\partial U} \right)_P = -L_a \left(\frac{\partial^2 g}{\partial U^2} \right)_P, \quad (4.11)$$

where L_a is the actuator channel length and q is assumed to be constant. The coupling coefficient $\left(\frac{\partial Q}{\partial P} \right)_U$ is

$$\left(\frac{\partial Q}{\partial P} \right)_U = -L_a \left(\frac{\partial}{\partial P} \right)_U \left(\frac{\partial g}{\partial U} \right)_P = -L_a \left(\frac{\partial}{\partial U} \right)_P \left(\frac{\partial g}{\partial P} \right)_U = L_a \left(\frac{\partial A}{\partial U} \right)_P. \quad (4.12)$$

Combining equations (4.1) and (4.12) yields the coupling coefficient

$$\alpha A L_a = \left(\frac{\partial Q}{\partial P} \right)_U. \quad (4.13)$$

Combining equations (4.8), (4.11), and (4.13) yields the piezo current

$$I = C_p \frac{dU}{dt} + \alpha A L_a \frac{dP}{dt}. \quad (4.14)$$

In general, the pressure is a function of position. When the fluctuations are sufficiently slow for the system to come to rest locally, the piezo current can be obtained by integrating over the length of the actuator,

$$I = C_p \frac{dU}{dt} + \alpha A \int_0^{L_a} \frac{dP}{dt} dx. \quad (4.15)$$

This approximation is valid here, since the wavelength is much larger than the channel radius, ensuring that the system is in local equilibrium. The piezo current is now known in terms of the actuator voltage and the channel pressure.

From the Fourier transform of the pressure, the Fourier transform of the piezo current I_f can be calculated. Inserting the expression of the pressure into equation (4.15), applying the Fourier transform defined in equation (4.3), and dividing by $e^{i\omega t}$ yields an expression for the piezo current,

$$I_f = i\omega C_p U + \alpha A_j \frac{\omega}{k_j} (-P_{r,j} e^{-ik_j L_a} + P_{l,j} e^{ik_j L_a}) + \alpha_j A_j L_a i\omega P_s. \quad (4.16)$$

If the electric signal source were an ideal voltage source, the voltage over the actuator would now be prescribed and the electrical resistance would vanish. The piezo current would be determined and measured as an indication of the acoustics in the channel. In reality however, the signal generator is not an ideal voltage source but has an output impedance R_p . Therefore the voltage over the piezo actuator is not imposed, but is obtained as a part of the solution. The

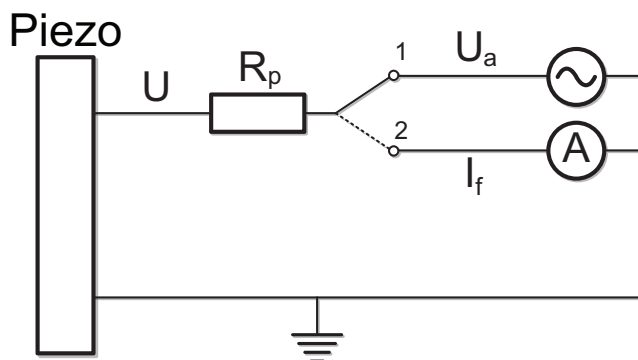


Figure 4.5: The simplified measurement circuit: The switch changes between 1, actuation and 2, when the piezo is used as hydrophone. The output impedance, R_p , is in reality distributed throughout the system. It consists of resistance at connections, in wires, in the amperemeter, and in the voltage source. The jet pulse U_a differs from the voltage U over the piezo electrodes due to this resistance. In reality, the voltage source consists of a number of linked devices: an arbitrary waveform generator, a switchboard, and amplifiers.

symbols that refer to electric properties of the measurement system are clarified in figure 4.5. The piezo voltage is the sum of the actuation pulse U_a and the voltage over the output impedance of the signal generator and the connections,

$$U = U_a - I_f R_p. \quad (4.17)$$

When equation (4.17) is inserted into equation (4.16), an expression for the piezo current with a nonideal voltage source is obtained,

$$I_f = i\omega C_p (U_a - I_f R_p) + \alpha A_j \frac{\omega}{k_j} (-P_{r,j} e^{-ik_j L_a} + P_{l,j} e^{ik_j L_a}) + \alpha A_j L_a i\omega P_s. \quad (4.18)$$

Upon rearranging, the piezo current for a finite output resistance is obtained as

$$I_f = \frac{1}{1 + i\omega C_p R_p} \left(i\omega C_p U + \dots + \alpha_j A_j \frac{\omega}{k_j} (-P_{r,j} e^{-ik_j L_a} + P_{l,j} e^{ik_j L_a}) + \alpha_j A_j L_a i\omega P_s \right). \quad (4.19)$$

This expression shows that a finite output resistance acts as a low-pass filter with a cutoff frequency of $\omega_c = \frac{1}{C_p R_p}$. Since the order of magnitude of the output impedance is typically $R_p = 100 \Omega$ and the capacitance of the piezo actuator is about 1 nF , the cutoff frequency is typically $\omega_c = 10 \text{ MHz}$, which is much larger than any relevant frequencies. Therefore, the output impedance can be neglected.

The coupling coefficient α_j and the wall flexibility β_j can be determined by comparison of the measured and calculated piezo current. Modifying the coupling coefficient changes the magnitude of the measured signal, but not its shape. So when the correct value of α_j is used in the model, the amplitudes of the measured and calculated piezo currents are equal. The wall flexibility changes

the resonance frequencies of the channel. Thus, when the correct value of β_j is used, the frequencies that are present in the calculated piezo current match those in the measured signal. These conditions were used to determine both parameters. Now that these parameters have been determined, the current from a printhead with a bubble can be modeled and compared with the experiment (see figure 4.6).

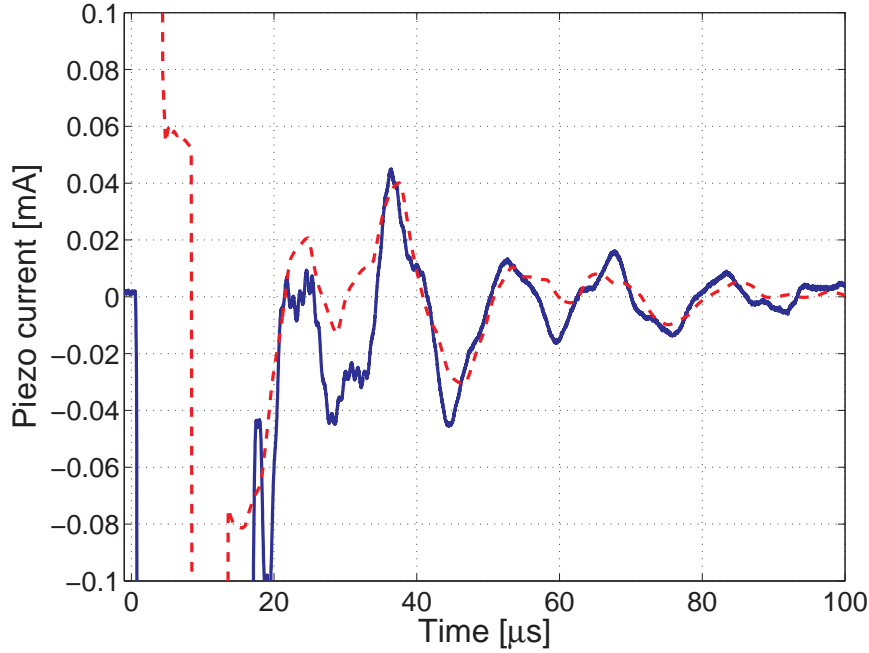


Figure 4.6: The measured (solid line) and calculated piezo currents (dashed line). Both amplitude and frequency match which indicates that both the wall flexibility and the piezo electric coupling coefficient are chosen correctly.

4.5 Comparing the model with experiments

In order to compare the model with the experiment, it is convenient to single out the change in the piezo current due to the bubble. Therefore, the piezo current of the undisturbed nozzle I_0 is subtracted from the piezo current obtained when a bubble is entrapped $I(V_b)$. This gives the differential piezo current

$$\tilde{I}(V_b) = I(V_b) - I_0. \quad (4.20)$$

We will distinguish between the experimental differential current \tilde{I}_e , with a corresponding optical measured bubble volume V_e , and the differential current resulting from the model $\tilde{I}_m(V_m)$, where V_m is the volume of the bubble assumed in the calculation. The undisturbed piezo current is obtained experimentally by measuring the piezo current in the absence of an entrained bubble. With the model, the undisturbed current can be obtained by setting the bubble volume to

zero. Figure 4.7 shows examples of experimentally obtained differential currents \tilde{I}_e . This figure illustrates again the pronounced change in the piezo current when an air bubble is present, compared to the current of an undisturbed channel. Moreover, it shows that even for very small bubbles, the change in the piezo current is still significant.

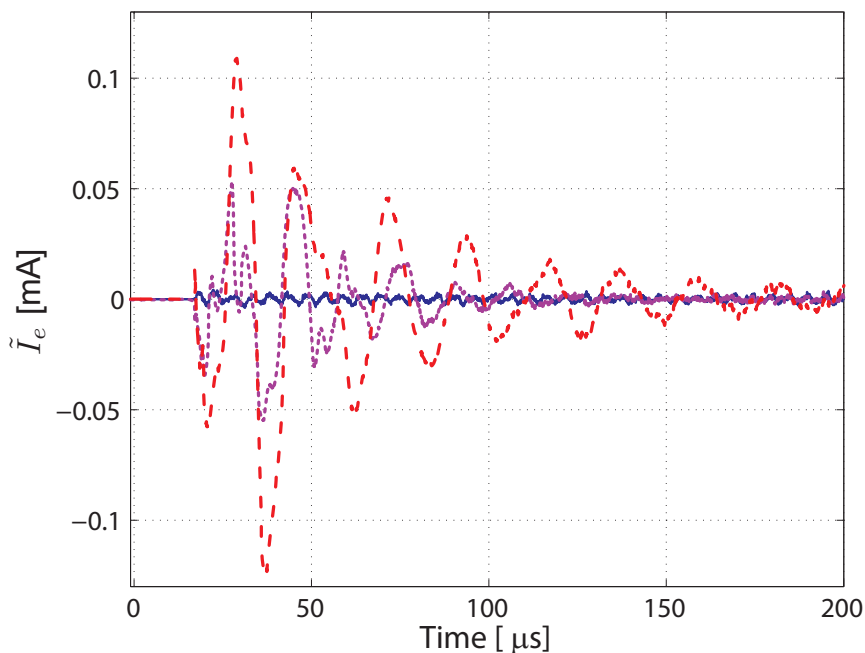


Figure 4.7: Experimentally obtained differential piezo currents $\tilde{I}_e = I_e - I_0$. The solid line shows the signal of an undisturbed channel, the dotted line shows the signal when a bubble of 5 pl is entrapped and the dashed line shows the signal when a bubble of 81 pl is entrapped. The signal from the undisturbed channel shows the magnitude of noise in the measurements. Obviously, in the absence of noise, the differential piezo current of the undisturbed channel would have vanished throughout.

The difference between the measured and calculated piezo current can be expressed as $\delta_i(V_m)$, the relative norm of the difference, defined as

$$\delta_i(V_m) = \frac{\|\tilde{I}_e - \tilde{I}_m(V_m)\|}{\|\tilde{I}_e\|}. \quad (4.21)$$

Here the L_2 norm is used, which is defined as

$$\|f(t)\|_2 \equiv \sqrt{\frac{1}{T} \int_0^T |f(t)|^2 dt}. \quad (4.22)$$

The norm of the difference is nondimensionalized using the norm of the measured differential current. When a bubble is entrapped, the value of $\delta_i(V_m)$ depends on the bubble volume V_m that is assumed in the calculation. The value of

$\delta_i(V_m)$ is close to zero when the differential current of the model matches the differential current of the experiment. Note that $\delta_i(V_m)$ is a positive definite function of the bubble volume that is assumed in the calculation. Therefore, when $\delta_i(V_m)$ reaches a minimum, the match between model and experiment should be optimal. The value V_m for which this minimum is reached should then correspond to the measured bubble volume. In figure 4.8, the relative norm of the difference is shown for 8 measured piezo currents as a function of the assumed bubble volume. The functions are smooth and well behaved, which facilitates the search for their minimum. In the domain used in the calculation only a single minimum is found for $\delta_i(V_m)$. To illustrate the agreement between

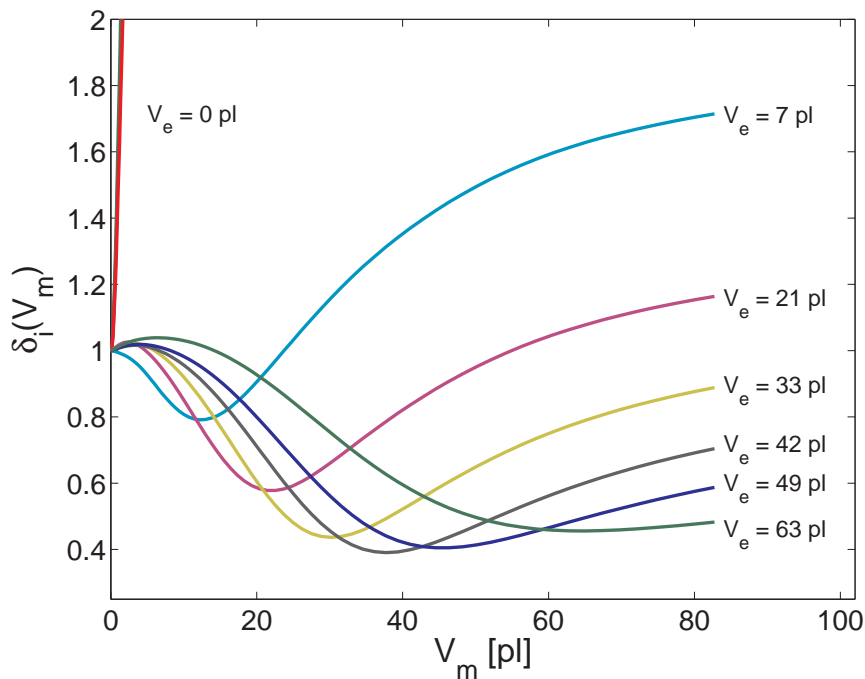


Figure 4.8: Norm of the difference between the measured and calculated disturbances. This function of the bubble volume has a distinct minimum where the agreement between the model and the experiment is the highest. The graphs where no bubble is present rise sharply from a value of $\delta_i(V_m) = 1$ at zero bubble volume. The optically found bubble volumes are shown on the right of the curves; it agrees with the position of the minimum, revealing the success of the employed model.

the model and experiment at this minimum, figure 4.9 shows the differential piezo current of a measurement with its modeled counterpart. In this example, the optically obtained bubble volume was 81 *pl*. By inserting the corresponding piezo current into the model the minimum in $\delta_i(V_m)$ was found for a bubble of 86 *pl*. As can be seen in figure 4.9, the calculated piezo current closely resembles the measured piezo current in both frequency and amplitude.

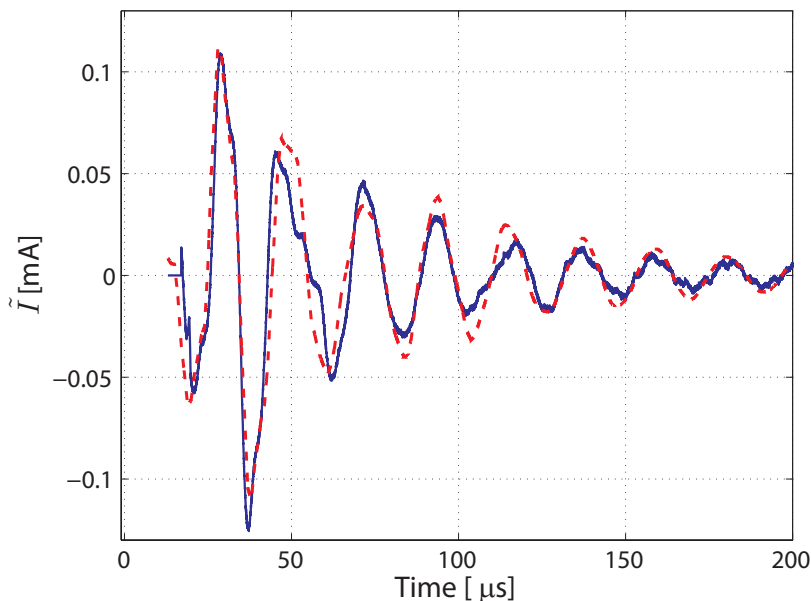


Figure 4.9: The calculated differential piezo current $\tilde{I}_m(V_m)$ (dashed) is compared with the experimentally obtained differential piezo current $\tilde{I}_e(V_e)$ (solid). For these currents the model finds a bubble volume of 86 μl , which is close to the value of 81 μl that was measured optically.

The quality of the model becomes even more convincing in figure 4.10, where V_e , gathered during the bubble dissolution process, is compared with V_m calculated by the model. For both methods, the absolute error is given by the colored area. The absolute error in the optically obtained bubble volume increases with the bubble volume. This originates from the measurement method, where the radius is extracted from the images with an accuracy of a few pixels. The absolute error is about $0.9 \mu\text{m}$, independent of the bubble size itself. As the bubble volume is $V_e = \frac{4}{3}\pi r_e^3$, where r_e is the bubble radius, the relative error in the bubble volume is three times the relative error in the radius; $\frac{\Delta V_e}{|V_e|} = 3 \frac{\Delta r_e}{|r_e|}$. Correspondingly, the absolute error $\Delta V_e = (4\pi r_e^2)\Delta r_e$, is quadratic in the bubble radius. Note that the error in the optical bubble volume does not affect the error in the calculated result, as V_e is not a parameter of $\delta_i(V_m)$, but only the current I_e which was measured simultaneously with V_e .

The error in the acoustic measurement ΔV_m is calculated from the minimum value in figure 4.8 by using

$$\Delta V_m = \frac{\left\| \tilde{I}_e - \tilde{I}_m(V_m) \right\|_2}{\frac{\partial}{\partial V_m} \left\| \tilde{I}_m(V_m) \right\|_1}. \quad (4.23)$$

Here the difference between the calculated piezo current and the measured piezo current is assumed to be Gaussian white noise. The derivative is evaluated by

a finite difference approximation.

In the inset of figure 4.10, the ratio of the acoustically measured bubble volume over the optically measured bubble volume is shown. This illustrates that for bubbles above 20 pl , the relative error is less than 12 percent. For small bubble the relative error diverges, and the acoustic measurement method becomes less accurate. This is attributed to nonlinear volume oscillations of the air bubble, which this linearized model cannot capture.

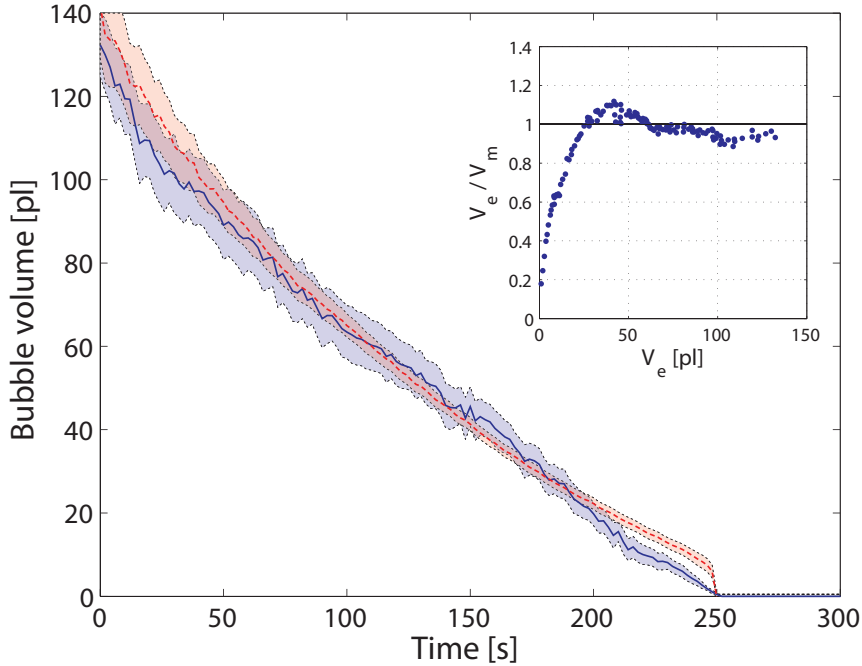


Figure 4.10: Acoustically measured bubble volume (V_m) is shown as a dotted line and the optically measured bubble volume (V_e) is shown as a solid line. The areas around the lines give the error margins in the results. In the inset, the ratio of the optically measured bubble volume over the acoustically measured bubble volume is shown. This illustrates that the relative error diverges for small bubbles. For larger bubbles, the relative error is less than 12 percent.

4.6 Summary & Outlook

A linear model is used to estimate the volume of a bubble in an inkjet channel. With this model it is shown how a bubble influences the channel acoustics of an inkjet printhead. The linear approximation in this model is valid for bubbles that are larger than 20 pl . Small bubbles exhibit nonlinear behavior, which the model cannot capture. Therefore, the acoustic measurement method is less accurate in this regime. To overcome this problem, the method can be extended by solving the full nonlinear equations. The two-way coupling with the channel acoustics turns the Rayleigh-Plesset equation into a delay differential equation.

This nonlinear equation can be solved numerically [29] at the cost of increased calculation time.

The model calculates the current through the actuator. By comparing the current with experimentally obtained currents, the model is able to accurately determine the bubble volume. In this way, an acoustic measurement method for the volume of entrapped air bubbles is obtained. This method was validated with optically measured bubble volumes. In addition, this shows that the linear regime of volume oscillations of an air bubble in an inkjet microchannel and the corresponding channel acoustics is well understood.

Bibliography

- [1] T.G. Leighton *The acoustic bubble*, Academic Press, (1997).
- [2] C.E. Brennen, *Cavitation and Bubble Dynamics*, Oxford University Press (1995).
- [3] M.S. Plesset, A. Prosperetti, *Bubble Dynamics and Cavitation*, Ann. Rev. of Fluid Mech. **9**, 145-185 (1977).
- [4] M.P. Brenner, S. Hilgenfeldt, D. Lohse, *Single-bubble sonoluminescence*, Rev. Mod. Phys. **74**, 425-485 (2002).
- [5] S. Qin, K.W. Ferrara, *Acoustic response of compliant microvessels containing ultrasound contrast agents*, Phys. Med. Biol. **51** 5065-5088 (2006).
- [6] S. Qin, K.W. Ferrara, *The natural frequency of oscillation of ultrasound contrast agents in microvessels*, Ultrasound in Med. & Biol. **33**, 1140-1148 (2007).
- [7] C.F. Caskey, S. M. Stieger, S. Qin, P.A. Dayton, K.W. Ferrara, *Direct observations of ultrasound microbubble contrast agent interaction with the microvessel wall*, J. Acoust. Soc. Am. **122**, 1191-1200 (2007).
- [8] V.S. Ajaev, G.M. Homsy, *Modeling Shapes and Dynamics of Confined Bubbles*, Annu. Rev. Fluid Mech. **38**, 277-307 (2006).
- [9] A. L. Klibanov, *Ultrasound contrast agents: Development of the field and current status*, Top. Curr. Chem. **222**, 73106 (2002).
- [10] R.J. Dijkink, J.P. van der Dennen, C.D. Ohl, A Prosperetti, *The 'acoustic scallop': a bubble-powered actuator*, J. Micromech. Microeng. **16**, 1653 (2006).
- [11] Kelly Siew Fong Lew, Evert Klaseboer, Boo Cheong Khoo, *A collapsing bubble-induced micropump: An experimental study*, Sensors and Actuators A: Physical. **133**, 161-172 (2007).
- [12] J. de Jong, R. Jeurissen, H. Borel, M. van den Berg, M. Versluis, H. Wijshoff, A. Prosperetti, H. Reinten, D. Lohse, *Entrapped air bubbles in piezo-driven inkjet printing: Their effect on droplet velocity*, Phys. Fluids **18**, 121511 (2006).
- [13] J. de Jong, G. de Bruin, H. Reinten, M. van den Berg, H. Wijshoff, M. Versluis, D. Lohse, *Air entrapment in piezo-driven inkjet printheads*, J. Acoust. Soc. Am. **120**, 1257-1265 (2006).

- [14] R. Jeurissen, J. de Jong, H. Reinten, M. van den Berg, H. Wijshoff, M. Versluis, D. Lohse, *Effect of an entrained air bubble on the acoustics of an ink channel*, J. Acoust. Soc. Am. **123**, 2496-2505 (2008).
- [15] B. Krasovitskia, E. Kimmel, *Gas bubble pulsation in a semiconfined space subjected to ultrasound*, J. Acoust. Soc. Am., **109**, 891-898 (2001).
- [16] P. Zhong, Y. Zhou, S. Zhu, *Dynamics of bubble oscillation in constrained media and mechanisms of vessel rupture in swl* Ultrasound in Med. & Biol., **27** 119134, (2001).
- [17] J. Cui, M. Hamilton, P. Wilson, E. Zabolotskaya *Bubble pulsations between parallel plates*, J. Acoust. Soc. Am. **119**, 2067-2072 (2006).
- [18] H. Oğuz, A. Prosperetti, *The natural frequency of oscillation of gas bubbles in tubes*, J. Acoust. Soc. Am. **103**, 3301 (1998).
- [19] E. Sassaroli, K. Hynynen, *Forced linear oscillations of microbubbles in blood capillaries*, J. Acoust. Soc. Am. **115**, 3235-3243 (2004).
- [20] E. Ory, H. Yuan, A. Prosperetti, S. Popinet, S. Zaleski *Growth and collapse of a vapor bubble in a narrow tube*, Phys. Fluids **12**, 1268-1277 (2000).
- [21] K.S. Kwon, W. Kim, *A waveform design method for high-speed inkjet printing based on self-sensing measurement*, Sensors and Actuators A, **140**, 75-83 (2007).
- [22] J.F. Dijksman, *Hydrodynamics of small tubular pumps*, J. Fluid Mech. **139**, 173-191 (1984).
- [23] D.B. Bogy, F.E. Talke, *Experimental and Theoretical Study of Wave Propagation Phenomena in Drop-on-Demand Ink Jet Devices*, IBM J. Res. Develop. **28**, 314-321 (1984).
- [24] Micronit Microfluidics B.V., P.O. box 214, 7500 AE Enschede, The Netherlands, info@micronit.com.
- [25] M.A. Groninger, P.G.M. Kruijt, H. Reinten, R.H. Schippers and J.M.M. Simons, *A method of controlling an inkjet printhead, an inkjet printhead suitable for use of said method, and an inkjet printer comprising said printhead*, European Patent, EP 1 378 360 A1 (2003).
- [26] J.R. Womersley, *Method for the calculation of velocity, rate of flow and viscous drag in arteries when the pressure gradient is known*, J. Physiol., **127**, 553-563 (1955).
- [27] T. Young, *Hydraulic investigations, subservient to an intended Croonian Lecture on the motion of the blood*, Philos. Trans. R. Soc. Lond. **98**, 164186 (1808).
- [28] H. Callen *Thermodynamics and an introduction to thermostatistics*, second edition John Wiley and Sons (1985).
- [29] L.F. Shampine, S. Thompson, *Solving DDEs in MATLAB*, Appl. Num. Math. **37**, 441-458 (2001).

Chapter 5

Regimes of bubble volume oscillations

Productivity of an inkjet printer is limited by the effect on the acoustics of air bubbles that are entrained into ink channels. When a bubble is entrained, it is very small. However, due to the volume oscillations of the bubble, gas diffuses towards the bubble so that the bubble grows. Eventually, the printing process is disrupted. As a step towards solving this problem, bubble volume oscillations are studied in the complex situation of an inkjet printhead, which is basically a bubble in a long pipe with a nozzle. In this paper, a complete set of dimensionless groups for all the parameters that specify a bubble in a pipe is derived and interpreted. The regimes of bubble volume oscillations are predicted theoretically with these dimensionless groups. A numerical model is developed to test these predictions. For this model, the Rayleigh-Plesset equation is extended to include the influence of the bubble volume oscillations on the acoustic field and vice versa. This modified Rayleigh-Plesset equation is coupled to a channel acoustics calculation and a Navier-Stokes solver for the flow in the nozzle. The theoretical predictions are confirmed by the results from the numerical simulations.

5.1 Introduction

The dynamics of volume oscillations of a bubble in a pipe are important in the application of bubbles as ultrasound contrast agents in blood vessels to diagnose and treat cardiovascular diseases [1–3]. To investigate the behavior of these ultrasound contrast bubbles and their coating, some researchers place the bubble inside a capillary to keep it in place [4, 5]. In microfluidic applications, a bubble in a capillary can be used as an actuator [6]. Another application where the behavior of a bubble in a pipe is relevant is in inkjet printing. Entrained air bubbles in the ink channel of an inkjet print head are harmful to the jetting process [7]. These applications are fairly recent, and the available literature on this problem is still scarce. However, the investigations of the individual components, pipe acoustics and bubble dynamics, are venerable subjects of

research.

The study of pipe acoustics started more than two centuries ago. In the early nineteenth century, Young derived the influence of wall flexibility on the propagation velocity of pressure disturbances in a flexible pipe. In the latter half of the nineteenth century, just 20 years after the introduction of viscosity to account for internal friction in deforming liquids, Korteweg derived the influence of viscosity on the propagation of acoustic waves in a rigid pipe. Both derivations were limited to wavelengths that are much larger than the pipe radius. A general analysis of the propagation of acoustic waves in a rigid pipe, where the influence of thermal damping and viscosity are taken into account, was derived by Kirchhoff in the form of a transcendental equation. Kirchhoff also provided an approximate solution to this equation for large wave numbers. Womersley [8] applied these equations to the flow of blood in arteries in animals. He showed that the dimensionless group that indicates the magnitude of inertia over viscosity is constant for many different mammals, even though the radii are very different. This dimensionless group is now called the Womersley number, although it was already known by Korteweg 70 years earlier. An overview of the different approximate solutions to Kirchhoff's solution is given by Tijdeman [22]. Tijdeman showed that the entire problem is governed by three dimensionless groups, one dimensionless group for the magnitude of thermal effects, the shear wave number or Womersley number for the magnitude of viscosity, and the reduced frequency for the allowed modes of propagation of acoustic disturbances.

The study of bubble dynamics started over a century ago with the study by Lord Rayleigh of what later turned out to be cavitation damage on ship propellers. Many researchers after Lord Rayleigh have extended this work, culminating in what is now known as the Rayleigh-Plesset equation. This equation is discussed extensively in textbooks [9,10]. The Rayleigh-Plesset equation couples the gas pressure inside a bubble to the radial flow field that results from volume oscillations of that bubble. In this flow field, inertia, viscous friction, and surface tension lead to a difference in pressure between the interior of the bubble and the pressure far away from the bubble. These effects are taken into account in the Rayleigh-Plesset equation.

The study of the interaction between pipe acoustics and volume oscillations of a bubble in a finite volume of liquid is very recent. The case of a bubble near a flat wall has been studied earlier [11]. See also [12] for a more recent study. The method of images can be employed to obtain the volume oscillations for a bubble near a flat infinite wall. The spherically symmetric case of a bubble in a spherical liquid-filled flask was studied by Nigmatulin et al. [13]. The effect of reverberation in a rectangular tank was studied both experimentally and analytically by Leighton et al. [14]. They note that the method of images yields a solution that grows in time. By taking into account damping of the acoustic waves in the tank, they were able to obtain a physically relevant solution. Oguz and Prosperetti were the first to analytically study the behavior of an air bubble in a pipe [15]. Their model is a potential flow calculation of a bubble on the axis of a finite pipe. They determined the natural frequency of oscillation and the thermal damping. This model was validated experimentally by Sassaroli and Hynnen [16]. Cui et al determined the natural frequency of oscillation of a bubble between two parallel plates [17] by a similar analysis. The nucleation and growth of a large vapor bubble in a pipe were determined by Ory et al [18], by solving the full Navier-Stokes equation numerically. The bubble volume

oscillations in an inkjet printhead were predicted theoretically and validated experimentally by Jeurissen et al [20]. They showed that in the complicated geometry of an ink jet printhead, with the coupling to the induced acoustics, the small-amplitude volume oscillations could be predicted by a modified Rayleigh-Plesset equation. We now extend this method to large amplitude oscillations, and provide the criteria that indicate the regimes where this approach is valid and necessary.

5.2 Dimensionless groups

For the case of a bubble in a pipe, criteria for comparison of acoustic effects with effects of bubble volume oscillations, have not yet been established. These relations are quantified in this section by identifying the corresponding dimensionless groups. Dimensionless groups that compare acoustic effects with each other, and dimensionless groups that compare effects in bubble volume oscillations with each other have been described at length in the literature. They are included in the list of dimensionless groups for completeness.

A systematic procedure for obtaining a complete set of dimensionless groups is suggested by Buckingham's Pi theorem. The smallest number of dimensionless groups that contain all independent parameters is equal to the number of dimensional parameters minus the number of different base units in those parameters. To compile a complete list of the parameters that specify the flow, all effects are considered individually.

In pipe acoustics, compressibility is relevant. It introduces the velocity of sound c as a relevant parameter. Unsteady inertia introduces the density of the liquid ρ_l , the angular frequency ω , and the sound pressure P_a , although the pressure amplitude drops out since channel acoustics per se is linear. The length L and the radius R_c of the pipe further determine how the sound can propagate. Viscous friction introduces the dynamic viscosity μ_l . Thermal conduction introduces the thermal conductivity of the liquid κ_l and the isobaric specific heat capacity $C_{P,l}$ of the liquid. The wall flexibility introduces the relaxation time of the wall τ and the wall compliance β , defined as

$$\beta = \frac{1}{A_c} \left(\frac{\partial A_c}{\partial P} \right) \quad (5.1)$$

where $A_c = \pi R_c^2$ is the cross-sectional area of the pipe. In the case of a capillary tube embedded in a liquid, wall relaxation arises due to acoustic radiation losses into the ambient environment. From these parameters, the kinematic viscosity ν_l and the thermal diffusivity D_l of the liquid are derived.

$$\nu_l = \frac{\mu_l}{\rho_l} \quad (5.2)$$

$$D_l = \frac{\kappa_l}{C_{P,l}\rho_l} \quad (5.3)$$

Both material parameters have dimensions of surface area over time.

Bubble volume oscillations imply compression of the gas in the bubble. This compression influences the pressure in the bubble. This introduces the equilibrium bubble radius R_0 , the saturated vapor pressure P_v , the isobaric specific heat capacity of the bubble gas $C_{P,g}$, and the thermal conductivity of the gas

κ_g . The pressure difference over the bubble wall is the Laplace pressure. This introduces the surface tension σ . The equilibrium pressure P_0 and the pressure fluctuation constitute the pressure in the liquid adjacent to the wall. Further, the angular frequency ω , the pressure amplitude P_a , the liquid density ρ_l , the gas density ρ_g , and the liquid viscosity μ_l are also relevant for the bubble dynamics.

The units of the dimensional parameters are listed below. Subscripts are dropped in this list.

$$\begin{aligned}
 [c] &= \frac{m}{s} \\
 [\rho] &= \frac{kg}{m^3} = \frac{Ns^2}{m^4} \\
 [\omega] &= \frac{1}{s} \\
 [P] &= \frac{N}{m^2} \\
 [L] &= m \\
 [R] &= m \\
 [\mu] &= \frac{Ns}{m^2} \\
 [\kappa] &= \frac{W}{mK} = \frac{N}{sK} \\
 [C] &= \frac{J}{kgK} = \frac{m^2}{s^2K} \\
 [\tau] &= s \\
 [\beta] &= \frac{m^2}{N} \\
 [\sigma] &= \frac{N}{m}
 \end{aligned} \tag{5.4}$$

To obtain a complete set of dimensionless groups, Buckingham's Pi theorem is applied to the obtained list of parameters. There are 18 dimensional parameters with 4 different base units. A total number of 14 dimensionless groups is therefore required to specify the problem. The choice of nondimensional groups is somewhat arbitrary. In general, they compare the magnitudes of two effects. The following set of dimensionless groups is chosen so that effects whose relevance is in question can be compared to an effect that is expected to be significant in most cases. For instance, various pressure terms are compared to the ambient pressure because ambient pressure is not expected to be dominated by any of the other terms in most applications. The corresponding dimensionless groups are expected to be either small, or of order unity. If one of the terms dominates the ambient pressure, the significance of other effects is more readily estimated from a different set of dimensionless groups. For example, in the case of cavitation nuclei, which are very small bubbles, Laplace pressure is dominant. At cavitation inception, the pressure amplitude is larger than Laplace pressure. A criterium for cavitation inception is therefore more readily expressed in the ratio of pressure amplitude over Laplace pressure. In such extreme cases, a different set of dimensionless groups can be obtained from the ones that are presented here as ratios of these groups.

The 10 dimensional parameters that specify channel acoustics can produce 6 independent dimensionless groups.

$$\begin{aligned}
 \text{Pr}_l &= \frac{\nu_l}{D_l} = \frac{C_{P,l}\mu}{\kappa_l} \quad \text{viscosity over heat conduction (Prandtl number)} \\
 \text{Wo} &= R_c \sqrt{\frac{\omega\rho_l}{\mu}} \quad \text{square root of inertia over viscosity (Womersley number)} \\
 \Pi_1 &= \beta c^2 \rho_l \quad \text{wall flexibility over liquid compressibility} \\
 \Pi_2 &= \tau\omega \quad \text{wall relaxation time over acoustic period} \\
 \Pi_3 &= \frac{\omega R_c}{c} \quad \text{pipe radius over wave length (reduced frequency)} \\
 \Pi_4 &= \frac{\omega L}{c} \quad \text{pipe length over wave length}
 \end{aligned}$$

When the product Pr Wo^2 is large, adiabatic conditions are obtained while isothermal conditions are obtained for small values of this product [23]. In either fully isothermal or fully adiabatic conditions, thermal damping in the channel can be neglected. When the Womersley number is large, the viscous boundary layer is thin and the acoustic waves can propagate over many wavelengths before they are damped significantly. In the limit of small Womersley number, the flow reduces to Poiseuille flow and the pressure disturbances are governed by a parabolic equation, more akin to diffusion than to wave propagation. When Π_1 is large, the flow is nearly incompressible. The potential energy is then stored in the pipe wall, instead of in the liquid. When Π_2 is small, the pipe is locally at rest at all times and wall relaxation provides little damping. When Π_2 is very large, wall relaxation limits the wall movement. In this case, the magnitude of wall relaxation damping depends on the ratio of Π_1 over Π_2 . A small value of this ratio indicates that the walls are too slow to follow the pressure, thus most of the potential energy is stored in the compressibility of the liquid where it is not damped by wall relaxation. This leads to little damping. When the reduced frequency Π_3 is small, no transverse modes of acoustic propagation are admitted. As shown by Beltman [23], the reduced frequency is small in many applications, which greatly simplifies the analysis. When Π_4 is small, compressibility effects are small and the flow becomes incompressible.

The 11 dimensional parameters that specify the bubble dynamics, of which 4 were already encountered in the channel acoustics, produce 7 independent dimensionless groups. The 4 dimensional parameters that also pertain to the acoustics specify a length scale, a time scale, and a force scale. The liquid properties and the frequency provide all scales. The pressure amplitude could have been expressed as the Mach number, which is the ratio of liquid velocity over the velocity of sound. This would not be very useful since in linear acoustics, the Mach number is small per definition. Therefore, the pressure amplitude is nondimensionalized in the context of the bubble dynamics, where it provides a

useful comparison.

$$\begin{aligned}
\text{Pe} &= \frac{R_0^2 \omega \rho_g C_{P,g}}{\kappa_g} \quad \text{oscillation over heat conduction (Péclet number)} \\
\text{Re} &= \frac{R_0^2 \rho_l \omega}{\mu} \quad \text{unsteady inertia over viscosity (bubble Reynolds number)} \\
\Pi_5 &= \frac{\sigma}{P_0 R_0} \quad \text{Laplace pressure over ambient pressure} \\
\Pi_6 &= \frac{P_v}{P_0} \quad \text{vapor pressure over ambient pressure (boiling threshold)} \\
\Pi_7 &= \frac{P_a}{P_0} \quad \text{pressure fluctuation amplitude over ambient pressure} \\
\Pi_8 &= \frac{4R_0^3 \omega \rho_l c}{3R_c^2 P_0} \quad \text{acoustic coupling from bubble to pipe} \\
\Pi_9 &= \frac{\rho_g}{\rho_l} \quad \text{density ratio}
\end{aligned}$$

The group Π_8 follows from analysis. The acoustic coupling is determined by Π_8 , which compares the bubble size with the size of the pipe. This parameter follows from reflection of an acoustic wave at a bubble in a pipe. Neglect pipe wall flexibility, viscous and thermal damping, inertia of the radial flow field from the bubble, vapor pressure, and surface tension. Assume small amplitudes and a polytropic relation for the pressure in the bubble.

$$P_b V_b^\gamma = \text{constant} \quad (5.5)$$

A power series expansion of this equation yields a relation between the respective pressure and volume fluctuations, which are marked with a tilde.

$$\tilde{P}_b = -\tilde{V}_b \frac{\gamma P_0}{V_0} \quad (5.6)$$

where γ is the polytropic index, which is $\gamma = 1$ for isothermal volume oscillations and $\gamma = \frac{7}{5}$ for adiabatic volume oscillations of a diatomic gas.

To obtain a relation between the bubble volume oscillations and the acoustic waves, we introduce the volume of an acoustic wave. Consider a monochromatic inviscid acoustic wave of amplitude P_a that propagates through a rigid pipe in the z direction. The pressure due to this wave is

$$P(z, t) = \frac{1}{2} P_a e^{i(\omega t - kz)} + \frac{1}{2} P_a e^{-i(\omega t - kz)}. \quad (5.7)$$

The velocity due to this wave is

$$u(z, t) = P_a \frac{k}{2i\omega \rho_l} \left(e^{i(\omega t - kz)} + e^{-i(\omega t - kz)} \right). \quad (5.8)$$

The volume flow rate due to this wave is the product of the velocity and the cross sectional area A_c of the pipe. The volume V that has flown through a cross-section of the pipe is obtained by integrating the volume flow rate over time.

$$V(z, t) = P_a \frac{k A_c}{2i\omega^2 \rho_l} \left(e^{(\omega t - kz)} - e^{-i(\omega t - kz)} \right) \quad (5.9)$$

The volume amplitude is

$$V_a = P_a \frac{A_c}{\rho_l c \omega}. \quad (5.10)$$

This volume shall be called the volume of the acoustic wave.

The amplitude of the incident wave is P_i , the amplitude of the reflected wave is P_r , and their sum equals the pressure fluctuation at the bubble.

$$P_i + P_r = -\tilde{V}_b \frac{\gamma P_0}{V_0} \quad (5.11)$$

The bubble emits waves in both directions, one wave is the reflected wave, and the other is the modification of the incident wave into the transmitted wave. Thus, the volume fluctuation of the bubble is twice the volume of the reflected wave.

$$\frac{2A_c}{\rho c \omega} P_i = \tilde{V}_b \quad (5.12)$$

combine equations 5.11 and 5.12 to obtain the reflected wave amplitude.

$$P_i = - \left(1 + \frac{2A_c \gamma P_0}{\rho c \omega V_0} \right) P_r = - \left(1 + \frac{2}{\Pi_8} \right) P_r \quad (5.13)$$

The bubble volume oscillation is driven by the pressure in the pipe, but the bubble volume oscillation also acts back on the pressure in the pipe. If the bubble is large, $\Pi_8 \gg 1$, the incident wave is completely reflected, and the transmitted wave vanishes. If the bubble is small, $\Pi_8 \ll 1$, the reflected wave vanishes and the influence of the bubble volume oscillations on the pressure in the pipe can be neglected. For large Π_8 , this two-way coupling is dominant.

The bubble volume oscillations are also small when the bubble is large with respect to the acoustic field in the pipe. The ratio $\frac{\Pi_7}{\Pi_8}$ is the ratio of the acoustic volume over the bubble volume. When $\frac{\Pi_7}{\Pi_8}$ is small, the bubble can absorb the acoustics with small volume oscillations. When both $\frac{\Pi_7}{\Pi_8}$ and Π_7 are large, the volume and pressure of the acoustic wave are both large enough to drive the bubble into nonlinear volume oscillations.

When the Péclet number is large, thermal conduction in the bubble is small, so that the bubble compression and expansion is nearly adiabatic. A small Péclet number indicates isothermal volume oscillations. Neither limiting case exhibits thermal damping. Thermal damping only occurs at intermediate Péclet numbers. When the bubble Reynolds number is small, bubble volume oscillations are hardly damped by the viscosity of the radial flow field from the bubble. When Π_5 is large, the bubble is mostly held together by Laplace pressure, instead of ambient pressure. The ratio of vapor pressure over ambient pressure Π_6 is the threshold above which the liquid starts to boil. When $\Pi_6 > 1$, any bubble can be made to explode by a large enough finite size perturbation. When $\Pi_7 > 1$ and both $\Pi_5 \ll 1$ and $\Pi_6 \ll 1$, cavitation can occur as the pressure at the bubble can become negative. For small values of the actuation pressure, $\Pi_7 > 1$, the bubble volume oscillations are small except at resonance. A small density ratio Π_9 , as in the case of a gas bubble in a liquid, indicates that the inertia of the bubble gas is negligible with respect to the inertia of the radial liquid flow field from the bubble.

Of the 14 independent dimensionless groups that are required to completely specify the complete system, 6 compare the magnitude of effects in the channel

acoustics, and 7 compare the magnitude of effects in the bubble volume oscillations. The remaining dimensionless group is the ratio of heat capacities of the thermal boundary layers in the liquid and in the bubble gas.

$$\Pi_{10} = \frac{\kappa_g C_{P,g} \rho_g}{\kappa_l C_{P,l} \rho_l} \quad (5.14)$$

For most combinations of gas and liquid, this ratio is small, indicating that the temperature of the liquid in the bubble wall is nearly constant, irrespective of the temperature in the bulk of the bubble.

The dimensionless groups that specify the system of a bubble in a pipe have been determined. The parameter Π_8 , that determines the importance of two-way coupling is arguably the most valuable of the constructed dimensionless groups. With this criterion, researchers can determine whether they can neglect the influence of the pipe and treat the bubble as if it were in an infinite volume of liquid, driven by the pressure that would be present in the absence of the bubble, or whether they need to take this influence into account.

5.3 Case study: a bubble in an inkjet print head

The developed theory is now used to analyse a bubble in an inkjet printhead. First, the printhead is described and the relevant parameter values are given. Second, the dimensionless groups are evaluated with these parameter values to predict which effects are relevant.

The considered inkjet print head consists of a few hundred ink channels. Each channel is terminated by the ink reservoir at one end, and a nozzle at the other end as shown in figure 5.1. The pressure in the reservoir is constant. The channel consists of a few sections where the equilibrium cross-sectional area is constant over its length. The channel section closest to the reservoir is flexible and it can be deformed actively by a piezo actuator. The cross-sectional area change due to the actuator is small with respect to the transverse dimensions. The nozzle cross-sectional area is much smaller than the channel cross-sectional area. The nozzle length is of the same order of magnitude as the channel radius. In reality, this channel section is rectangular, but it is modelled as a cylindrical channel with the same cross-sectional area.

The relevant parameter values are given below for a typical system.

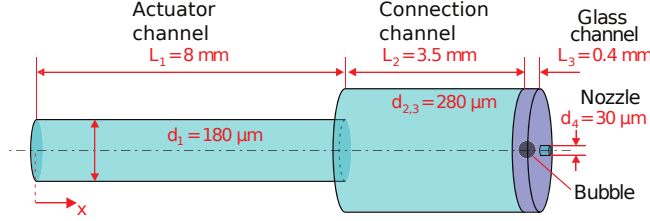


Figure 5.1: The print head as it is implemented in the model. From left to right: the actuator channel to which the piezo is attached, the connection channel, the glass connection channel, and the nozzle.

$$\begin{aligned}
 c &= 1250 \text{ m s}^{-1} \\
 \rho_l &= 1090 \text{ kg m}^{-3} \\
 \rho_g &= 1.2 \text{ kg m}^{-3} \\
 \omega &= 5 \cdot 10^5 \text{ s}^{-1} \\
 L &= 10^{-2} \text{ m} \\
 R_c &= 125 \cdot 10^{-6} \text{ m} \\
 \mu_l &= 0.01 \text{ Pa s} \\
 \kappa_l &= 0.15 \text{ W m}^{-1} \text{ K}^{-1} \\
 C_{P,l} &= 2 \cdot 10^3 \text{ J kg}^{-1} \text{ K}^{-1} \\
 \tau &= 5 \cdot 10^{-8} \text{ s} \\
 \beta &= 5 \cdot 10^{-10} \text{ Pa}^{-1} \\
 P_v &= 2400 \text{ Pa} \\
 C_{P,g} &= 10^3 \text{ J kg}^{-1} \text{ K}^{-1} \\
 \kappa_g &= 0.025 \text{ W m}^{-1} \text{ K}^{-1} \\
 \sigma &= 0.024 \text{ N m}^{-1} \\
 P_0 &= 10^5 \text{ Pa} \\
 P_a &\in [10^3, 10^6] \text{ Pa} \\
 R_0 &\in [0.01, 100] \mu\text{m}
 \end{aligned}$$

Except for the relaxation time τ and the frequency, all parameters are geometrical parameters or material parameters. The relaxation time given by electric coupling of actuator electrodes. The capacitance C of the piezo actuator and the resistance R with which it is coupled to the voltage source, be it a signal generator or ground, set the relaxation time.

$$\tau = RC = 100 \Omega \cdot 500 \text{ pF} = 5 \cdot 10^{-8} \text{ s} \quad (5.15)$$

The cutoff frequency of the system is chosen as the frequency scale. The actuation pulses that are used in normal operation of this printhead generate a pressure spectrum near the nozzle that is dominated by this resonance. The dominant frequency doubles when a large bubble is present, but the order of magnitude remains the same. See [7] for details.

All of the dimensional parameters of the system are now specified. The dimensionless groups are evaluated and the implications of their values are discussed. First, consider the situation where the bubble radius is $R_0 = 10^{-5} m$ and the pressure fluctuation amplitude is $P_a = 10^5 Pa$, which is the pressure amplitude at normal operating conditions. Later, these parameters will be varied to study their effect on the bubble dynamics.

$$\text{Pr}_l = 130 \quad (5.16)$$

The large Prandtl number indicates that viscous friction dominates dissipation due to heat conduction. Thermal effects in the acoustics can be neglected.

$$\text{Wo} = 20 \quad (5.17)$$

The large Womersley number indicates that unsteady inertia dominates viscosity in the acoustics. Damping of the acoustics occurs only after many wave lengths. Viscous effects can be neglected in the channel. Note that the nozzle radius is an order of magnitude smaller than the channel radius. In the nozzle, inertia and viscosity are comparable.

$$\Pi_1 = 0.5 \quad (5.18)$$

Wall flexibility and liquid compressibility are about equally important in the acoustics. Both have to be taken into account.

$$\Pi_2 = 0.025 \quad (5.19)$$

The wall relaxation time is much smaller than the acoustic period. Damping due to relaxation in the wall can be neglected.

$$\Pi_3 = 0.04 \quad (5.20)$$

The small value of the reduced frequency indicates that the pipe radius is much smaller than the wave length, so that the low reduced frequency approximation can be applied. The pressure is nearly constant over the cross-section of the pipe. Transverse acoustic modes can be neglected.

$$\Pi_4 = 4 \quad (5.21)$$

The pipe length is about equal to the wave length. Reflections arrive within a few periods of oscillation. The flow can not be approximated by incompressible flow, nor can the pipe be considered infinitely long. Both compressibility and reflections have to be taken into account.

$$\text{Pe} = 20 \quad (5.22)$$

The large bubble Péclet number indicates that bubble volume oscillations are nearly adiabatic.

$$\text{Re} = 5 \quad (5.23)$$

The moderate bubble Reynolds number indicates that unsteady inertia is somewhat larger than viscosity, but viscosity cannot be neglected with respect to the inertia of the radial flow field from the bubble.

$$\Pi_5 = 0.024 \quad (5.24)$$

Laplace pressure is much smaller than the ambient pressure. The ambient pressure is the dominant force that keeps the bubble from exploding. This criterion is the same as a criterion given by Hilgenfeldt et al. [24] for small bubbles in an unbounded liquid.

$$\Pi_6 = 0.024 \quad (5.25)$$

Vapor pressure is much smaller than ambient pressure. This indicates that the ink in the printhead is not boiling.

$$\Pi_7 = 2 \quad (5.26)$$

The large bubble limit that Hilgenfeldt et al. [24] give is based on the pressure fluctuation amplitude, which we capture in Π_7 . If this dimensionless group is of order unity or larger, the pressure amplitude of the acoustics is large enough to drive the bubble into nonlinear volume oscillations.

$$\frac{\Pi_7}{\Pi_8} = 2 \quad (5.27)$$

The volume displacement of the acoustic waves in the channel are of the some order of magnitude as the bubble volume. The volume of the acoustics is large enough to drive the bubble into the nonlinear regime of volume oscillations. Since both the volume and the pressure amplitude of the acoustics are large enough to drive the bubble into nonlinear oscillations, nonlinearity cannot be neglected.

$$\Pi_8 = 1 \quad (5.28)$$

The acoustic coupling from bubble to pipe is significant, but not dominant. Some of the acoustics will be reflected by the bubble, and some will be transmitted. The two-way coupling between the bubble volume oscillations and the channel acoustics cannot be neglected.

When the bubble volume is varied, a number of regimes are encountered, demarcated by one of the dimensionless groups becoming large or smaller than unity. The novel elements in the analysis are $\frac{\Pi_7}{\Pi_8}$ for the volume of the acoustic field over the bubble volume, and Π_8 for the magnitude of two-way coupling between the acoustics and the bubble volume oscillations. These dimensionless groups depend on the bubble volume. For large bubbles, both groups become large, making the two-way coupling dominant, but the bubble volume oscillations are restricted to small amplitudes.

At a bubble radius of $R_0 \ll 13 \mu m$, $\frac{\Pi_7}{\Pi_8}$ becomes large and Π_8 becomes small. This indicates that two-way coupling can be neglected, but the volume of the acoustic field is large enough to drive the bubble into the nonlinear regime. As the bubble explodes during a period of low pressure, it again becomes large enough to make two-way coupling significant. Both dimensionless groups change at nearly the same time since the pressure amplitude is of the same order of magnitude as the ambient pressure. For smaller actuation amplitudes, there is an intermediate region where two-way coupling is small while the bubble volume oscillations are in the linear regime.

For very small bubbles, where $\Pi_5 \gg 1$ is large, Laplace pressure dominates ambient pressure. If the ratio of pressure amplitude over ambient pressure $\Pi_7 \sim 1$ is still of order unity, the pressure amplitude is small with respect to Laplace pressure for such small bubbles. The bubble volume oscillations become


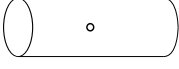
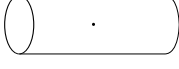

bubble radius	interaction type	
100 μm	small oscillations two-way coupling	
10 μm	large oscillations two-way coupling	
1 μm	large oscillations one-way coupling*	
0.1 μm	-----	
0.01 μm	small oscillations one-way coupling	

Figure 5.2: The different regimes of bubble volume oscillations and the corresponding equilibrium bubble radius. Large bubbles are not only driven by the acoustics, but their volume oscillations also act back on the acoustics. This two-way coupling between bubble volume oscillations and pipe acoustics is not present for smaller bubbles.

(*) Two-way coupling is also relevant for bubbles whose equilibrium radius is smaller than 1 μm , if the pressure and volume amplitude of the acoustics are large enough to cause the bubble to expand into the two-way coupling regime.

small again. This regime corresponds to a bubble radius of $R_0 \ll 250 \text{ nm}$, which is very small indeed. Since bubbles usually dissolve at a rate of 1 pl s^{-1} between actuations, this bubble would dissolve in $65 \mu\text{s}$. This regime of very small bubbles, where Laplace pressure limits volume oscillations, will not be encountered in most applications.

When both the pressure amplitude and the bubble size are varied, the phase diagram, figure 5.3 shows 3 major regions:

2-way coupled, large volume oscillations Both pressure amplitude and volume amplitude are large ($\frac{\Pi_7}{\Pi_8} > 1$ and $\Pi_7 > 1$), and Laplace pressure is small ($\Pi_5 < 1$) so that the bubble volume oscillations are large with respect to the bubble volume. Even if 2-way coupling is small at the equilibrium bubble radius ($\Pi_8 \ll 1$), the bubble can expand to a size where this 2-way coupling is important due to the large acoustic field. An analysis of the bubble dynamics in this regime will have to take into account both 2-way coupling and nonlinear volume oscillations.

2-way coupled, small volume oscillations The volume amplitude of the acoustic field is too small to induce large volume oscillations ($\frac{\Pi_7}{\Pi_8} < 1$). In a part of this regime ($\Pi_7 > 1$), the pressure fluctuation amplitude is also too small to induce large volume oscillations. In this regime, 2-way coupling cannot be neglected, but the bubble volume oscillation is linear.

1-way coupled, small volume oscillations In the region where the pressure fluctuation amplitude is small ($\frac{\Pi_7}{\Pi_8} < 1$), and/or Laplace pressure is large ($\Pi_5 >$

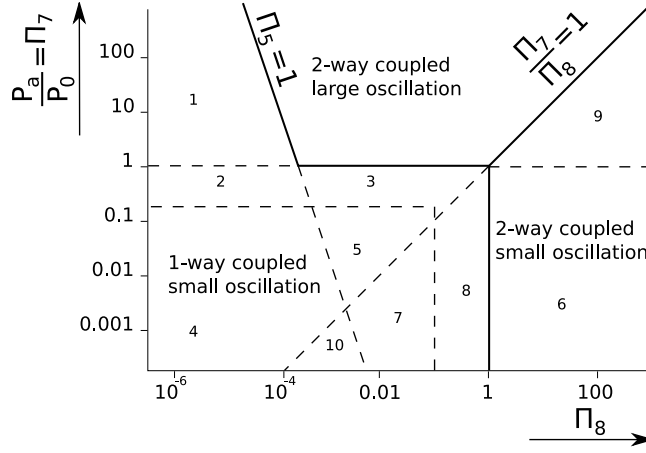


Figure 5.3: Phase diagram of the type of bubble volume interaction versus equilibrium bubble radius and actuation amplitude. There are 3 major regimes: 2-way coupling is important and volume oscillations are large, 2-way coupling is important and volume oscillations are small, and 2-way coupling is not important and volume oscillations are small. The boundaries between different regimes are the locus where one of the dimensionless groups is becomes equal to one. For different geometries and materials, the boundaries between the regimes can change. Usually, all the other parameters are fixed by the design and fabrication of system. The bubble radius and actuation amplitude are the variables that are most easily modified. See the main text for an explanation of the numbered regions.

1), and 2-way coupling at the equilibrium radius is small ($\Pi_8 < 1$), the bubble volume oscillations are small and 2-way coupling is small.

More than one criterion for small volume oscillations can be satisfied simultaneously besides the criteria that determine the boundary of the regime. For instance, viscous friction in the radial flow field from the bubble can limit oscillations if the Reynolds number is small $Re < 1$ and

$$\frac{\Pi_7}{\Pi_8} \cdot Re^{\frac{3}{2}} < 4\Pi_3 \cdot Wo. \quad (5.29)$$

The small Reynolds number and the small two-way coupling ensure that the pressure amplitude is balanced by viscous friction in the radial flow field from the bubble. The second condition is obtained by balancing the viscous term in the Rayleigh-Plesset equation with the imposed pressure amplitude. In dimensional parameters, this condition is simpler.

$$\frac{P_a}{4\mu\omega} < 1 \quad (5.30)$$

This extra restriction on the volume oscillations is irrelevant for the parameters of the considered inkjet printhead since even if it weren't fulfilled, volume oscillations would still be small due to the small pressure amplitude. For higher

frequencies or higher viscosities, this condition can extend the region where bubble volume oscillations are small. The numbered subregions in figure 5.3 differ in which the conditions for small volume oscillations are satisfied.

1. Laplace pressure is large
2. pressure amplitude is small and Laplace pressure is large
3. pressure amplitude is small
4. viscous damping is large and Laplace pressure is large and pressure amplitude is small
5. viscous damping is large and pressure amplitude is small
6. pressure amplitude is small and volume of the acoustic waves is small
7. pressure amplitude is small and volume of the acoustic waves is small and viscous friction is large
8. pressure amplitude is small and volume of the acoustic waves is small
9. volume of the acoustic waves is small
10. all of the above

An effect is only negligible where the corresponding dimensionless group is large or small, whichever is appropriate. The given boundaries of the regimes are the locations where the corresponding dimensionless group is equal to one. Therefore, there is a transitional region, around the indicated regime boundaries. The width of this transitional region cannot be assumed *ex ante* to be constant in the given presentation and should, if necessary, be determined by experiments or further analysis.

5.4 Numerical model

The predicted regimes in the phase space of a bubble in a pipe are examined with a numerical model of a bubble in an inkjet printhead. A model is developed that can cover the entire phase space of driving amplitude and bubble size that experimental conditions permit to study. In particular, this model should neither be restricted to linear oscillations, nor to bubbles that are so small that their influence on the pressure in the channel is negligible.

The response of the parts of the system that exhibit linear behavior can be efficiently calculated in the frequency domain. Linear volume oscillations of a bubble in the regime where two-way coupling is relevant can be calculated with the linearized model of Jeurissen et al. [20], where a formulation in the frequency domain is used. However, the nonlinear case cannot be solved as conveniently in the frequency domain, since the nonlinearity in the governing equations introduce coupling terms between the various frequency components. Only the channel acoustics remain linear in character. Correspondingly, the channel acoustics are still calculated with the linear model of Jeurissen et al. The Rayleigh-Plesset equation, that describes the bubble volume oscillations, is

not linearized. The nozzle flow is not linearized either.¹ The nonlinear equations for the bubble volume and the nozzle flow are solved in the time domain, while the channel acoustics are calculated in the frequency domain.

The flow field in the nozzle is decomposed into a part due to the bubble volume oscillations and the flow due to the pressure drop over the nozzle, the nozzle flow. The flow field due to the bubble is approximated by a modified Rayleigh-Plesset equation. The nozzle flow is axisymmetric, and this symmetry is used in the calculation of this flow. The nozzle flow calculation takes the pressure at the interface with the channel as an input, and gives the flow rate through this interface due to the nozzle flow as an output. The flow rate due to the nozzle flow and the flow rate from the bubble constitute the total flow through the interface. This flow is coupled to the channel acoustics to obtain the boundary condition at the channel.

Channel acoustics The channel acoustics impose a relation between the pressure and volume flow rate at the interface between the domains of the nozzle flow and the channel acoustics. This relation depends on the parameters of the channel and the acoustic waves that arrive at the nozzle. The interaction of the nozzle flow and the channel generates acoustic waves that enter the channel. These waves propagate in the channel, they attenuate, and they reflect off the interface between the actuation channel and the connection channel, and the end of the actuation channel where it is connected to the reservoir. These reflections also attenuate and, after a finite period of time, they reach the interface between the channel and the nozzle. This is one part of the acoustic waves that arrive at the nozzle. The other part consists of the acoustic waves that are generated by the actuator.

The acoustic wave field is decomposed into two Riemann invariants.

$$\begin{aligned} R_1 &= \frac{1}{2}P - \frac{1}{2}\rho_l c u \\ R_2 &= \frac{1}{2}P + \frac{1}{2}\rho_l c u \end{aligned}$$

The first Riemann invariant is the wave that travels into the channel. The second is the wave that arrives at the nozzle from the channel. If the second Riemann invariant and the velocity are known, the first Riemann invariant is also known. The velocity into the channel is obtained from the nozzle flow and the bubble dynamics. The objective of the channel acoustics calculation is to determine the second Riemann invariant.

The second Riemann invariant consists of waves that are generated by the actuation P_a , and of waves that originated from the nozzle. The channel acoustics are calculated in the frequency domain. In the frequency domain, analytical expressions of the transfer functions are available in closed form [20]. The transfer function can be converted to an impulse response by a Fourier transform. With this impulse response, the acoustic waves that arrive at the nozzle are given by a convolution integral.

$$R_2 = P_a + \int_{-\infty}^t R_1(t - \tau) f(\tau) d\tau \quad (5.31)$$

¹This resembles the procedure of efficient spectral methods for the Navier-Stokes equation.

This convolution integral is evaluated numerically in the numerical model.

Many different choices of impulse response are available. The impulse response from waves that are emitted into the channel to waves that arrive at the nozzle from the channel is chosen because of two advantages. First, this impulse response is the only one where the instantaneous component vanishes. All other impulse responses for this system have a dirac delta impulse at $t = 0$. This instantaneous component can be removed by incorporating it into the boundary condition as an algebraic term, but the present method is simpler. Second, this impulse response is the most compact impulse response since there are no reflections from the interface with the nozzle flow calculation domain. This boundary absorbs all of the energy that it receives, damping the acoustic waves as fast as possible.

The presented analysis for the boundary condition is exact in the inviscid limit. In the calculation of the impulse response, viscosity is taken into account, but viscosity was neglected in the definition of the Riemann invariants. Since the Womersley number is large in the channel, the error that is introduced by this approximation is expected to be small.

Bubble radius The Rayleigh-Plesset equation is an ODE for the bubble radius and its time derivatives, for a given pressure P_∞ far away from the bubble. The Rayleigh-Plesset equation balances the pressure in the bubble with inertia, viscosity, and surface tension.

$$R\ddot{R} + \frac{3}{2}\dot{R}^2 = \frac{1}{\rho} \left(\left(P_0 + \frac{2\sigma}{R_0} - P_v \right) \left(\frac{R_0}{R} \right)^{3\gamma} + P_v - \frac{2\sigma}{R} - \frac{4\mu\dot{R}}{R} - P_\infty \right) \quad (5.32)$$

Two distinct finite size effects might be relevant. The first is the influence of the bubble volume oscillations on the pressure far away from the bubble. In the Rayleigh-Plesset equation, this is absorbed in the P_∞ term, and it is the result of the interaction between the bubble volume oscillations, the nozzle flow, and the channel acoustics. It is obtained by interpolating the pressure field from the nozzle flow calculation at the location of the bubble. The importance of the influence of the component of the pressure that is generated by the bubble volume oscillations, can be estimated from the magnitude of Π_8 as shown in the previous section. The second finite size effect is the influence of the radial flow field from the image of the bubble in the channel wall. The pressure due to the radial flow from the bubble is small at a distance that is twice the bubble radius. The pressure that accompanies the radial flow from the bubble consists of two components. The first component is proportional to the velocity gradient, which scales as r^{-3} . The second component is proportional to the square of the velocity, which scales as r^{-4} . Doubling the distance to the center of the bubble reduces the pressure due to the radial flow field by a factor 8. Note that the image bubble is twice as far away as the wall. Unless the bubble is very close to the wall, the effect of the image bubble on the volume oscillations is negligible. Only the coupling with the channel acoustics is expected to be relevant in this case.

The channel acoustics and the bubble volume oscillations are coupled via the nozzle flow. The flow into the channel is the sum of the flow from the nozzle and the flow from the bubble. The pressure far away from the bubble P_∞ is obtained by evaluating the pressure field from the nozzle flow calculation at the

location of the bubble. The pressure at the channel is a boundary condition for the nozzle flow. This constitutes the full two-way coupling between the bubble volume oscillations, nozzle flow, and channel acoustics.

Nozzle flow The nozzle flow is calculated with a Navier-Stokes solver. This solver uses

- axisymmetry
- a staggered cartesian grid
- first order upwind differencing for the advection term (finite volume formulation)
- second order central differencing for the viscous term
- a projection method to project the imperfect time derivative due to advection and viscosity onto a solenoidal velocity field
- second order central differencing for the pressure term (finite volume formulation)
- a direct solver for the discretized pressure poisson equation, where the velocity at wall cells is set to zero to satisfy zero normal flow and no-slip simultaneously
- a standard fourth order Runge-Kutta ODE solver with an adaptive step size

At the interface between the channel and the nozzle flow domain, an inlet boundary condition is imposed at the pressure that is imposed by the channel acoustics calculation. At the end of the nozzle, where the meniscus is located, an inlet boundary condition is imposed at a pressure that follows from Laplace pressure and inertia, as described in the next paragraph. Since the geometry is fixed, the discretization of the pressure Poisson equation is also fixed. The discretized pressure poisson equation is solved with an LU decomposition with column reordering. This LU decomposition is calculated once, at the start of the simulation. With this LU decomposition of the pressure Poisson equation, the nozzle flow can be calculated in $O(N^2)$ flops, where N is the total number of cells.

Boundary condition at nozzle end At the meniscus, a Dirichlet boundary condition is imposed on the pressure. Since the meniscus is not stationary in reality, a full free surface treatment is necessary to completely capture the dynamics of the meniscus evolution. The added complexity of such a free surface treatment would increase the calculation time. However, the details of the meniscus evolution are not the object of study in this research. An approach that retains only the effects that are relevant to the bubble volume oscillations is more efficient. An approximation of the pressure at the end of the nozzle, that retains the effects of the meniscus that are relevant to the bubble dynamics but does not increase the complexity or calculation time, is sought.

The meniscus influences the volume oscillations mostly through its effect on the pressure. When a constant pressure is imposed at the end of the nozzle, the

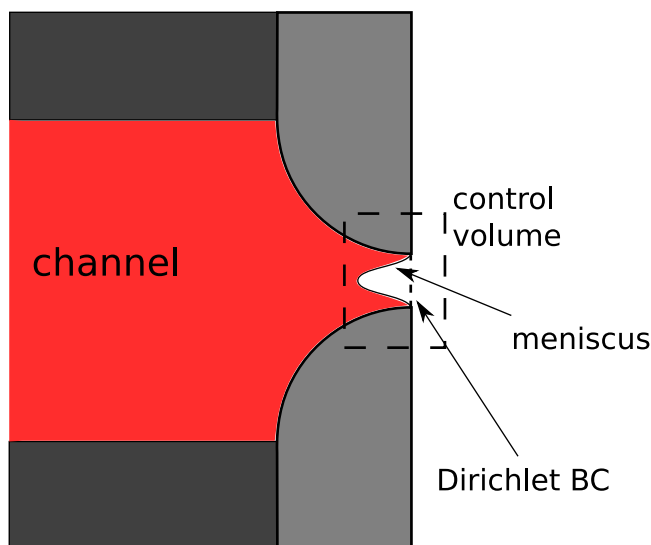


Figure 5.4: The nozzle, with the control volume

effect of the meniscus dynamics is neglected. There are two components of the meniscus dynamics that influence the pressure in the nozzle. The first component is the pressure at the meniscus which is determined by the meniscus shape through the Laplace pressure. The other component is the difference between imposing this pressure at the meniscus interface and imposing the pressure at the end of the nozzle. Both effects can be approximated by analysis of the control volume that contains the region where the meniscus oscillates, as shown in figure 5.4. The force on the ink in this control volume by surface tension is applied by the nozzle wall at the contact line. Only the axial component of the surface tension yields a nonzero contribution when integrated over the contact line.

$$F_{cap} = -2\pi R_n \sigma \sin(\arctan(\partial_r z_m)) \quad (5.33)$$

The axial position of the meniscus z_m is a function of radial position and time. This force is proportional to the nozzle radius R_n , so that the Laplace pressure P_l , which is force per area, is inversely proportional to the nozzle radius.

$$P_l = -\frac{2}{R_n \sigma} \sin(\arctan(\partial_r z_m)) \quad (5.34)$$

The slope of the meniscus at the contact line scales with the ratio of average meniscus position over nozzle radius. Higher order eigen modes of meniscus oscillation are neglected, so that the meniscus is a paraboloid.

$$\partial_r z_m = 2 \frac{\langle z_m \rangle_{A_n}}{R_n} \quad (5.35)$$

The average meniscus velocity is the ratio of the volume flow rate of ink volume, over the nozzle cross-sectional area. This follows from geometry.

$$\frac{d}{dt} \langle z_m \rangle_{A_n} = \frac{1}{A_n} \int_{A_n} u_z da \quad (5.36)$$

In this expression, the nozzle cross-sectional area is evaluated at the meniscus position. Droplet formation removes ink from the nozzle, therefore it causes meniscus retraction. This is modelled by limiting the meniscus position so that it does not protrude more from the nozzle than the specified distance. In this investigation, the meniscus position is limited to a distance equal to the nozzle radius. When the meniscus position is determined, the Laplace pressure can be calculated by equation 5.34. This completely specifies the Laplace pressure.

The influence of the meniscus position on inertia is a correction to the inertia in the calculation with a fixed meniscus position. The void that is present when the meniscus is retracted decreases the inertia of the ink in the nozzle. The inertia of the part of the meniscus that is occupied by the void should be subtracted. The inertia of the nozzle can be calculated with the same method as used by Jeurissen et al. [20], but extended to include the effect of advection. The pressure drops due to unsteady inertia P_i and due to advection ΔP over a length of nozzle between $z = 0$ and $z = z_m$ can be analytically calculated if advection and viscous friction are neglected, using Bernouilli's equation.

$$P_i = -\frac{dq}{dt} \rho \int_0^{z_m} \frac{1}{A_n} dz \quad (5.37)$$

The flowrate q is the integral of the axial velocity.

$$q = \int_{A_n} u_z da \quad (5.38)$$

Viscosity cannot be completely neglected, as indicated by the Womersley number, which is about $Wo = 3$ in the nozzle. However, the correction to the inertia is only relevant when the liquid that will form the droplet is ejected. This liquid is ejected at a velocity of about $u = 20 \text{ m s}^{-1}$, which yields a nozzle Reynolds number of about $Re_n = 30$, indicating that advection is dominant when the correction to inertia is significant. The entrance length is about $0.24R_n Re = 7R_n$, which is larger than the nozzle length. Advection cannot be neglected in the correction to the pressure, but viscosity can be neglected.

To take into account the effect of advection in the correction on the meniscus pressure, this effect is expressed in terms of the nozzle shape and the nozzle flow. Using the same approach as in the calculation of inertia, the velocity in the nozzle is determined by the nozzle flow and shape.

$$u_z = \frac{q}{A_n} \quad (5.39)$$

The pressure drop due to advection is given by Bernouilli's equation.

$$\Delta P = \frac{1}{2} \rho (u(0)^2 - u(z)^2) = \frac{1}{2} \rho q^2 \left(\frac{1}{(A_n(0))^2} - \frac{1}{(A_n(z_m))^2} \right) \quad (5.40)$$

In the pressure that is imposed at the end of the nozzle, the corrections for Laplace pressure and inertia are absorbed into the imposed pressure. The individual contributions are given by equations 5.34 and 5.37.

$$P_m = P_l + P_i + \Delta P \quad (5.41)$$

This specifies the pressure that is imposed at the end of the nozzle. For convenience, this equation is also given with the inertia terms inserted.

$$P_m = bP_l + \frac{1}{2}\rho q^2 \left(b(A_n(z_m))^{-2} - (A_n(0))^{-2} \right) + (1-b) \left(P_c - \frac{1}{2}\rho q^2 (A_n(z_c))^{-2} \right) \quad (5.42)$$

The pressure at the channel P_c follows from the channel acoustics calculation. The auxiliary function b is a geometrical quantity that describes the nozzle shape.

$$b = \frac{\int_{z_c}^0 \frac{1}{A_n} dz}{\int_{z_c}^{z_m} \frac{1}{A_n} dz} \quad (5.43)$$

Note that for very large meniscus retractions, this auxiliary function has a singularity. This cannot be avoided with this method, but since the singularity lies at a meniscus retraction that equals the length of the domain of the nozzle calculation, a full free surface treatment would also fail at these conditions. The meniscus must not retract all the way through the nozzle calculation domain. If this occurs, the nozzle calculation domain must be increased. The cause for this singularity serves to illustrate the method. From the pressure at the interface with the channel and the pressure at the meniscus, the pressure that would arise if the nozzle were completely filled is extrapolated. If the meniscus is located at the interface, the two abscissa coincide so that no extrapolation can be done.

The obtained set of delay differential equations that govern a bubble in an inkjet printhead is solved numerically. The method for solving delay differential equations that was described by Champine and Thompson [21] is not directly applicable in this case. The discretized equations for the nozzle flow constitute a large set of nonlinear equations, while the delayed influence is a single scalar. Storing the entire previous history is not necessary. In the model of bubble dynamics in an inkjet printhead, the evolution of the system is calculated over a small period at time, a period that is smaller than the time between the generation of acoustic waves and the arrival of the first reflection. The waves that arrive at the nozzle from the channel during the next period, are calculated from the flow rate into the channel during the previous period. Note that this flow rate is a single scalar function of time. The arriving waves determine the relation between the flow rate and the pressure. This relation is used as a boundary condition for the nozzle flow. This completes the description of the numerical model.

5.5 Validation

The theoretical predictions were tested with the developed numerical model. First, the bubble volume oscillations are examined in detail, at the actuation amplitude of normal operating conditions of the printhead and over a range of equilibrium bubble volumes. Second, the amplitude of volume oscillations and its influence on the pressure was calculated over a wide range of bubble volume and actuation amplitude, providing a direct validation of the theoretical predictions based on the dimensionless groups.

The prediction of the magnitude of volume oscillations and the relevance of two-way coupling was verified by calculating the evolution of a bubble in an inkjet printhead at 4 different bubble radii. The printhead is driven by

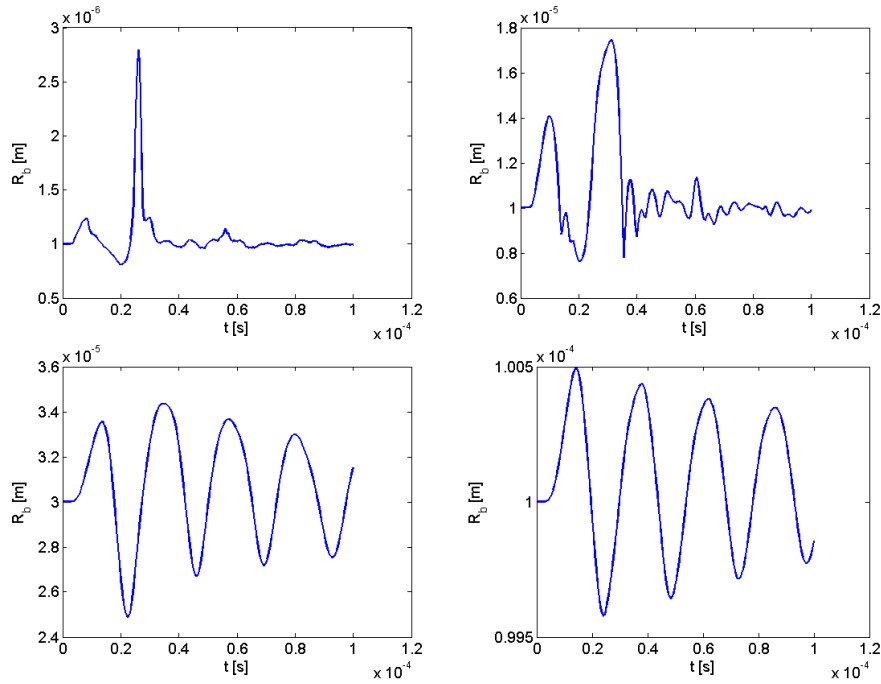


Figure 5.5: Radius versus time for bubbles of different sizes in an inkjet print-head. The equilibrium radius of the bubble is $R_0 = 1 \mu m$ (top left), $R_0 = 10 \mu m$ (top right), $R_0 = 30 \mu m$ (bottom left), and $R_0 = 100 \mu m$ (bottom right). The $R_0 = 30 \mu m$ radius bubble exhibits volume oscillations of the same order of magnitude as the bubble volume. The volume oscillations of the $R_0 = 100 \mu m$ bubble are negligible with respect to the bubble volume, while the volume oscillations of the smaller bubbles, with $R_0 = 1 \mu m$ and $R_0 = 10 \mu m$, are an order of magnitude larger than the bubble volume. The $R_0 = 1 \mu m$ bubble exhibits one explosion when the second low pressure wave arrives. The $R_0 = 10 \mu m$ bubble exhibits the large expansions, violent collapses, and afterbounces that are well known from the strongly nonlinear response of the Rayleigh-Plesset equation. The large bubbles oscillate smoothly at a frequency of about $40 kHz$, which corresponds closely to $44 kHz$, the lowest eigen frequency of the channel acoustics. The Minnaert angular frequencies of these bubbles are $3 MHz$, $300 kHz$, $100 kHz$, and $30 kHz$, respectively. The largest bubble's volume oscillations are very small, even though it is driven at a frequency close to its resonance frequency in an infinite volume of liquid.

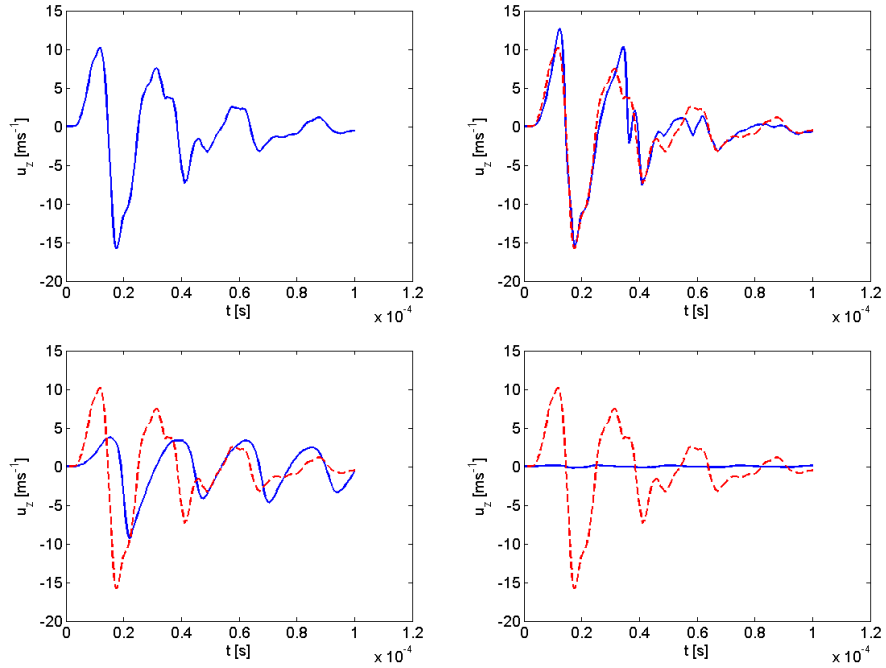


Figure 5.6: Velocity of the ink in the nozzle versus time, when bubbles of different sizes are present (solid line) and in the undisturbed situation where no bubble is present (dashed line). This nozzle velocity is the velocity of the ink averaged over the cross section of the nozzle. The equilibrium radius of the bubble is $R_0 = 1 \mu\text{m}$ (top left), $R_0 = 10 \mu\text{m}$ (top right), $R_0 = 30 \mu\text{m}$ (bottom left), and $R_0 = 100 \mu\text{m}$ (bottom right). The disturbance of the pressure by volume oscillations of a $R_0 = 1 \mu\text{m}$ bubble is so small that the graph of the nozzle velocity with a bubble completely obscures the graph of the undisturbed nozzle velocity. The $R_0 = 10 \mu\text{m}$ bubble exerts a noticeable, but not dominant influence on the nozzle velocity. A $R_0 = 30 \mu\text{m}$ bubble strongly influences the nozzle velocity. In the presence of a $R_0 = 100 \mu\text{m}$ bubble, the nozzle velocity becomes negligible with respect to the undisturbed nozzle velocity.

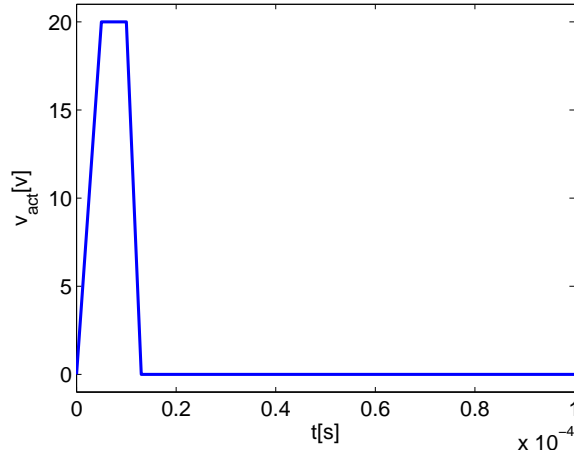


Figure 5.7: Driving pulse: voltage versus time. This pulse is typically repeated at a rate of 10 kHz , so that the portion shown is exactly one cycle. This pulse generates acoustic waves in the channel with an amplitude of $P_a = 10^5\text{ Pa}$, when applied to the described printhead.

a single trapezoidal pulse with a rising slope, high time, and falling slope of $5\ \mu\text{s} - 5\ \mu\text{s} - 3\ \mu\text{s}$, respectively, as shown in figure 5.7. Before and after the pulse, the actuator voltage is zero. The volume oscillations are shown in figure 5.5. For bubble radii of $R_0 = 1\ \mu\text{m}$ and $R_0 = 10\ \mu\text{m}$, large volume oscillations were predicted, as summarized in figure 5.2. The bubble radius changes from $R = 1\ \mu\text{m}$ to almost $R = 3\ \mu\text{m}$, and from $R = 10\ \mu\text{m}$ to $R = 20\ \mu\text{m}$. These radius fluctuation amplitudes correspond to volume fluctuation amplitudes of $\Delta V = 22V_0$ and $\Delta V = 6V_0$. These are large volume fluctuations, as predicted. A bubble radius of $R_0 = 30\ \mu\text{m}$ is at the boundary of small and large predicted volume oscillations. The radius fluctuation amplitude is $R = 5\ \mu\text{m}$, which is small with respect to the equilibrium radius. The volume fluctuation amplitude is $\Delta V = 1.6V_0$ which is neither large nor small. A bubble radius of $R_0 = 100\ \mu\text{m}$ is well within the range where small volume oscillations are predicted. The amplitude of the radius fluctuation is $R = 0.5\ \mu\text{m}$, which is small with respect to the equilibrium radius. The volume fluctuation amplitude is $\Delta V = 0.015V_0$ which is very small, as predicted. These numerical simulations confirm the theoretical predictions of the volume oscillation amplitude at the standard operating actuation amplitude of the inkjet printhead.

The relevance of two-way coupling between the channel acoustics and the bubble volume oscillations was also verified with the presented numerical simulations. This influence can be evaluated by comparing the velocity of the ink in the end of the nozzle when a bubble is present to the undisturbed velocity. The average over the cross-section at the end of the nozzle, of the axial velocity of the ink is used as a metric for comparison. This average velocity u_z is called the nozzle velocity. For low frequencies, the nozzle velocity can be considered proportional to the pressure in the channel for purposes of inspection. The nozzle velocity is driven by the pressure in the channel. The pressure drop

over the nozzle is balanced by inertia and viscous friction. The nozzle acts as a low-pass filter from pressure in the channel to velocity in the nozzle. At the cutoff frequency, viscous friction and inertia are of the same order of magnitude. This is indicated by a Womersley number of unity. The cutoff frequency is $\omega_c \sim 400 \text{ kHz}$. At frequencies below this cutoff frequency, the nozzle velocity is a good metric for the channel pressure.

The nozzle velocity versus time is shown in figure 5.6. The influence of a $R_0 = 1 \text{ }\mu\text{m}$ bubble on the nozzle velocity is negligible. Thus, the influence on the channel acoustics of such small bubbles is also negligible and two-way coupling can be neglected, in agreement with the theoretical prediction. At a bubble radius of $R_0 = 10 \text{ }\mu\text{m}$, two-way coupling is significant, but not dominant. At a bubble radius of $R_0 = 30 \text{ }\mu\text{m}$, the nozzle velocity is strongly influenced by the bubble volume oscillations. At a bubble radius of $R_0 = 100 \text{ }\mu\text{m}$, the nozzle velocity is negligible with respect to the undisturbed nozzle velocity. These numerical simulations confirm the theoretical predictions of the relevance of two-way coupling at the standard operating actuation amplitude of the inkjet printhead.

The theoretical predictions that are summarized in the phase diagram of figure 5.3 are now verified over a range of both actuation amplitude and bubble radius. As before, the bubble radius fluctuation amplitude and the nozzle velocity are evaluated to assess the volume fluctuation amplitude and the relevance of two-way coupling between the bubble volume oscillations and the channel acoustics, respectively. The ratio v of the L_2 norm of the volume fluctuation over the equilibrium volume is used as a metric for the amplitude of the bubble volume fluctuations.

$$v = \frac{\sqrt{\frac{1}{T} \int_0^T (V - V_0)^2 dt}}{V_0} \quad (5.44)$$

The value $v = 0.5$ is used as threshold. The ratio Tw is used as a metric for the relevance of two-way coupling and the value $\text{Tw} = 0.2$ is used as threshold.

$$\text{Tw} = \frac{\sqrt{\frac{1}{T} \int_0^T (u_z - u_{z,R=0})^2 dt}}{\sqrt{\frac{1}{T} \int_0^T (u_{z,R=0})^2 dt}} \quad (5.45)$$

This metric is small when the bubble volume oscillations have no significant effect on the pressure, and of order unity when the influence of the bubble volume oscillations on the pressure is significant. Note that a value of $\text{Tw} = 1$ indicates a large influence. This metric is exactly unity when the acoustic field is completely absorbed by the bubble so that the pressure fluctuation amplitude vanishes.

Both the Tw and v were calculated from the results of the numerical simulation for a range of bubble volumes and actuation amplitudes. The results are plotted into the relevant part of the phase diagram, see figure 5.8. The numerical results confirm the theoretical predictions based on the dimensionless groups. For very small bubbles, two-way coupling is insignificant for all actuation amplitudes that were simulated, even though the pressure amplitude is large enough for large bubble expansions. In these cases, the bubble volume remains small with respect to the volume of the acoustic field during the entire droplet formation cycle, although it becomes at least 1.5 times as large as the

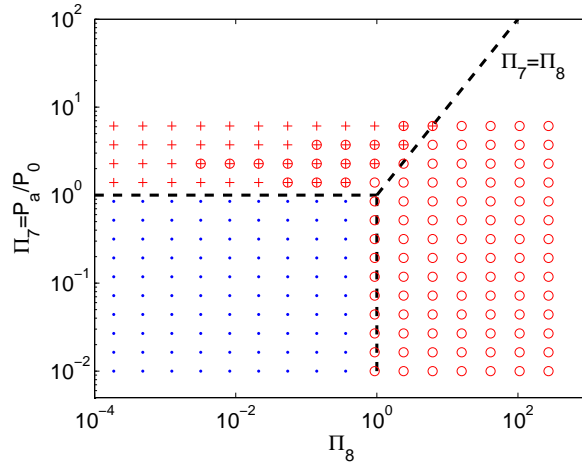


Figure 5.8: Locations where the amplitude of bubble volume oscillations is larger than $\frac{1}{2}$ (+ signs) and locations where the relevance of two-way coupling is significant (larger than $\frac{1}{5}$, circles), obtained from the results of the numerical calculations. Where two-way coupling was not found to be significant and the bubble volume oscillations were small, dots are drawn. The lines indicate where the transitions between different regimes were predicted by the dimensionless groups. In the top left region, volume oscillations were predicted to be large and as a result, two-way coupling was also predicted to be large if the bubble expands to a large volume. Volume oscillations are indeed large in this region, and two-way coupling is significant in a large part of this regime. For very small bubbles, two-way coupling is small. In these cases, the bubble does not expand to a volume that is large enough to influence the pressure, although the volume oscillations are large with respect to the equilibrium bubble volume. In the lower right region, two-way coupling was expected to be important, but small volume oscillations were predicted. These predictions are confirmed. In the lower left region, small volume oscillations and small two-way coupling were predicted. These predictions are also confirmed.

equilibrium volume. With the chosen threshold values, the transitions between regimes are within 20% of where they were predicted.

5.6 Conclusion

Bubble volume oscillations in an inkjet printhead are driven by an acoustic field. When the bubble in turn influences the acoustic field, there is two-way coupling between the bubble and the acoustic field. The relevant regimes of volume oscillations of a bubble in a pipe have been identified. Theoretical predictions of the magnitude of bubble volume oscillations in a pipe and the relevance of two-way coupling were derived analytically and verified with numerical simulations. The predictions were confirmed. For a bubble in an inkjet print head, this two-way coupling is nearly always significant. Only for small actuation amplitudes ($P_a \ll 10^5 \text{ Pa}$) and small bubbles ($R_0 \ll 12 \mu\text{m}$) can two-way coupling be neglected.

Bibliography

- [1] S. Qin, K.W. Ferrara, *Acoustic response of compliant microvessels containing ultrasound contrast agents*, Phys. Med. Biol. **51** 5065-5088 (2006).
- [2] C.F. Caskey, S. M. Stieger, S. Qin, P.A. Dayton, K.W. Ferrara, *Direct observations of ultrasound microbubble contrast agent interaction with the microvessel wall*, J. Acoust. Soc. Am. **122**, 1191-1200 (2007).
- [3] S. Qin, K.W. Ferrara, *The natural frequency of oscillation of ultrasound contrast agents in microvessels*, Ultrasound in Med. & Biol. **33**, 1140-1148 (2007).
- [4] K. Chetty, E. Stride, C.A. Sennoga, J.V. Hajnal, R.J. Eckersley *High-Speed Optical Observations and Simulation Results of SonoVue Microbubbles at Low Pressure Insonation*, IEEE trans. ultras., ferroel., and freq. control **55**, 1333-1342 (2008).
- [5] J. Sijl, E. Gaud, P.J.A. Frinking, M. Arditi, N. de Jong, D. Lohse, M. Versluis *Acoustic characterization of single ultrasound contrast agent microbubbles*, J. Acoust. Soc. Am. **124**, 40914097 (2008).
- [6] R.J. Dijkink, J.P. van der Dennen, C.D. Ohl, A Prosperetti, *The 'acoustic scallop': a bubble-powered actuator*, J. Micromech. Microeng. **16**, 1653 (2006).
- [7] J. de Jong, R. Jeurissen, H. Borel, M. van den Berg, M. Versluis, H. Wijs-hoff, A. Prosperetti, H. Reinten, D. Lohse *Entrapped air bubbles in piezo-driven inkjet printing: Their effect on droplet velocity*, Phys. Fluids **18**, 121511 (2006).
- [8] J.R. Womersley, *Method for the calculation of velocity, rate of flow and viscous drag in arteries when the pressure gradient is known*, J. Physiol., **127**, 553-563 (1955).
- [9] C.E. Brennen, *Cavitation and Bubble Dynamics*, Oxford University Press (1995).
- [10] T.G. Leighton *The acoustic bubble*, Academic Press, (1997).
- [11] K. Sato, Y. Tomira, A. Shima *Numerical analysis of a gas bubble near a rigid boundary in an oscillatory pressure field*, J. Acoust. Soc. Am. **95**, 2416-2424 (1994).

- [12] S. Popinet, S. Zaleski *Bubble collapse near a solid boundary: a numerical study of the influence of viscosity*, J. Fluid Mech. **464**, 137163 (2002).
- [13] R.I. Nigmatulin, I.S. Akhatov, N.K. Vakhitova *Forced oscillations of a gas bubble in a spherical volume of a compressible liquid* J. Appl. Mech. Tech. Phys. **40** 285-291 (1999).
- [14] T.G. Leighton, P.R. White, C.L. Morfey, J.W.L. Clarke, G.J. Heald, H.A. Dumbrell, K.R. Holland *The effect of reverberation on the damping of bubbles* J. Acoust. Soc. Am. **112** 1366-1376 (2002).
- [15] H. Oğuz, A. Prosperetti, *The natural frequency of oscillation of gas bubbles in tubes*, J. Acoust. Soc. Am. **103**, 3301 (1998).
- [16] E. Sassaroli, K. Hynynen, *Forced linear oscillations of microbubbles in blood capillaries*, J. Acoust. Soc. Am. **115**, 3235-3243 (2004).
- [17] J. Cui, M. Hamilton, P. Wilson, E. Zabolotskaya *Bubble pulsations between parallel plates*, J. Acoust. Soc. Am. **119**, 2067-2072 (2006).
- [18] E. Ory, H. Yuan, A. Prosperetti, S. Popinet, S. Zaleski *Growth and collapse of a vapor bubble in a narrow tube*, Phys. Fluids **12**, 1268-1277 (2000).
- [19] J. Billingham, A.C. King, *Wave motion*, Cambridge university press (2000).
- [20] R. Jeurissen, J. de Jong, H. Reinten, M. van den Berg, H. Wijshoff, M. Versluis, D. Lohse *Effect of an entrained air bubble on the acoustics of an ink channel*, J. Acoust. Soc. Am. **123**, 2496-2505 (2008).
- [21] L.F. Shampine, S. Thompson, *Solving DDEs in MATLAB*, Appl. Num. Math. **37**, 441-458 (2001).
- [22] H. Tijdeman, *On the propagation of sound waves in cylindrical tubes*, J. Sound and Vibr. **39**, 1 (1975).
- [23] W.H. Beltman, *Viscothermal wave propagation including acousto-elastic interaction, part I: Theory*, J. Sound and Vibr. **227**, 555-586 (1999).
- [24] S. Hilgenfeldt, M.P. Brenner, S. Grossmann, D. Lohse, *Analysis of Rayleigh-Plesset dynamics for sonoluminescing bubbles*, J. Fluid Mech. **365**, 171-204 (1998).

Chapter 6

Translation of a bubble in an inkjet printhead¹

The evolution of a bubble that has been entrained into an inkjet printhead is revealed using numerical simulations. To this end, a numerical model is developed, based on the Rayleigh-Plesset equation, full coupling with the flow field in the nozzle and the channel acoustics, and convection-diffusion for the gas exchange between the bubble and the ambient liquid. We show that the evolution of the bubble critically depends on its initial position. There are regions where bubbles that are entrained can be ejected within several droplet formation cycles. In other regions, the bubble moves towards a corner in the printhead, where it grows towards a stable diffusive equilibrium. Even before the bubble has reached this equilibrium, it has become so large that it disrupts the droplet formation process.

6.1 Introduction

In inkjet printing, nozzle failure must be dealt with to increase productivity [1]. Nozzle failure is caused by an air bubble that has been entrained into the nozzle. When a bubble is entrained, it is initially too small to significantly disturb the droplet formation. If the bubble remains in the channel for a few hundreds of actuations, it grows by rectified diffusion of dissolved air towards the bubble. Eventually, it is large enough to disrupt the droplet formation. This disruption of the droplet formation is called nozzle failure. Nozzle failure does not occur when the bubble is ejected from the nozzle before it is large enough to cause nozzle failure. To predict when such a recovery by bubble ejection can occur, we need to understand how a bubble moves through a printhead towards the meniscus where it can be ejected, and how a bubble grows in a printhead.

The application of analytical techniques is complicated by the large number of forces that act on the bubble. Experimental observations of the bubble motion are complicated by the small size of the bubble, the small time scales, and

¹This chapter will evolve towards a manuscript to be submitted to J. Fluid Mech.: Roger Jeurissen, Arjan van der Bos, Hans Reinten, Marc van den Berg, Herman Wijshoff, Michel Versluis, Detlef Lohse, *Translation of a bubble in an inkjet printhead*.

the fact that a normal printhead is made of opaque material. Therefore, we extend the numerical model of chapter 5 to study the motion and growth of an air bubble in an inkjet printhead. The printhead is also described in chapter 5. This model is used to predict the translation of the bubble per droplet formation cycle, for a range of axial positions, radial positions, and bubble sizes. These results are analyzed to extract the translation maps of the bubble for different bubble sizes. This information can be used to design future studies that do include experimental observations, and to interpret the results from those studies. The present study consists entirely of numerical modeling.

6.2 Numerical model

The objective of the numerical model that is described in this chapter is to calculate the motion and growth of a bubble in an inkjet printhead. A rigorous hydrodynamic treatment of such a bubble would require solving the two-phase flow problem by a surface tracking or surface capturing method. Although the accuracy and validity of such a rigorous approach is desirable, such an approach is not feasible because of the calculation time that a parameter study with these methods would require. The results would also be harder to interpret in terms of the distinct effects. Therefore, the interaction between the bubble and the ambient liquid is approximated with point force models, even when the bubble is not small with respect to the distance between the bubble and a wall. Since detailed experimental results are not available and full numerical simulations are not yet feasible, these approximations are necessary.

In our model, the motion of a bubble in an inkjet printhead follows from a force balance. The mass of the bubble itself is negligible so all the forces must sum to zero. The forces on the bubble that are considered are drag, lift, pressure gradient forces, and added mass. The viscous drag force is decomposed into a steady component called steady drag, and an unsteady component called history force. Added mass, reflects the momentum in the velocity field over the bubble. The pressure gradient forces are the Bjerknes forces, which arise from the pressure gradient of the ambient flow.

The forces on a bubble in an infinite volume of liquid have been studied extensively [4, 6, 11–14]. The forces on a bubble near a flat wall have recently been studied, [5, 7] to some extent. A wall influences drag, added mass, and lift. The presence of a wall also introduces a new force, secondary Bjerknes force. Originally, Bjerknes studied the acoustic force between two bubbles, but the same results have been applied to a bubble near a flat wall [3]. In that case, secondary Bjerknes force is the force between a bubble and its image in the wall [16]. When the wall is not flat, an image bubble cannot be defined so that all the boundary conditions are satisfied, but secondary Bjerknes force is present nonetheless. The secondary Bjerknes force on a bubble that arises in a finite space has not been studied as extensively. However, knowledge of this force is necessary for the simulation of the motion of an air bubble in an inkjet printhead. Therefore, the secondary Bjerknes force that arises in a finite space is derived by a potential flow analysis.

History force is hard to calculate in the low Reynolds number regime [12] since the force is nonlocal in time. The history force reflects the interaction between the bubble and its wake field. In the high Reynolds number regime,

this force is even harder to calculate since it is now not only nonlocal in time, but also subject to nonlinear evolution. In this regime, a complete calculation of the full 3-dimensional flow is necessary to calculate history force. It is, however, negligible in this case. The mean flow is of the same order of magnitude as the fluctuation. This mean flow convects the wake field away from the bubble, precluding any interaction with the bubble. The only interaction between the bubble and the wake field is the generation of the wake field. The time-dependent radius can have a significant effect on the drag, as shown by Magnaudet and Legendre [13], but the drag remains finite even when the bubble collapses. Therefore, the total momentum that is transferred by viscous friction to the bubble during a violent collapse is small due to the small time scale. The drag coefficient is taken equal to the steady flow value. For the entire range of expected Reynolds numbers $Re < 20$, Michaelides [11] gives an expression for the drag coefficient.

$$c_d = \frac{16}{Re_d} (1 + 0.1Re_d) - 0.02Re_d \ln(Re_d) \quad (6.1)$$

where the Reynolds number is based on the diameter of the bubble.

$$Re_d = \frac{2R_b u}{\nu} \quad (6.2)$$

This expression is valid for small Eotvos numbers. The Eotvos number Eo is the ratio of pressure gradient over surface tension.

$$Eo = \frac{2|\nabla P|R_b}{\sigma} \quad (6.3)$$

When the Eotvos number is small, surface tension is dominant, so the bubble remains nearly spherical. The maximum pressure gradient scales as the pressure fluctuation amplitude over the nozzle length. The pressure fluctuation amplitude is at most of the same order of magnitude as atmospheric pressure. When this magnitude of the pressure gradient is used, the Eotvos number is not small.

$$Eo = \frac{4P_0 R_b^2}{L_n \sigma} = 10 \quad (6.4)$$

In the nozzle, the small Eotvos number expression is not valid. In the channel, the relevant length scale is the wave length, which is about $\lambda = 1 \text{ cm}$. This gives a Eotvos number of $Eo = 0.05$. In the channel, the small Eotvos number expression is valid.

Added mass is the result of the displacement flow around an object. When an object moves through a fluid, the fluid must flow away at the front and flow towards the rear of the object to accommodate the change in location of the displacement of the fluid by the object. To induce a displacement flow to accommodate for the velocity $d\mathbf{u}$ of the object with respect to the ambient fluid, an amount of momentum $d\mathbf{p}$ must be applied to the fluid. The added mass is defined as the ratio of this momentum over the velocity of the object.

$$m_a \mathbf{u} = \mathbf{p} \quad (6.5)$$

In general, the added mass is a tensor. In the case of a sphere, it is a scalar.

$$m_a = \frac{1}{2} \rho_l V_b \quad (6.6)$$

The symbol V_b denotes the volume of the bubble, and ρ_l denotes the density of the ambient fluid. The force on the bubble due to added mass F_m is the time derivative of the momentum that is transferred onto the bubble from the ambient fluid.

$$\mathbf{F}_m = -\frac{d}{dt}(m_a \mathbf{u}) \quad (6.7)$$

Added mass can give rise to a force when the velocity of the bubble with respect to the ambient fluid changes, and when the bubble volume changes. The effect of volume fluctuations on the added mass has been known for quite some time on theoretical grounds. Recently, this prediction has been verified experimentally [19]. Added mass can be corrected for the presence of walls in the same way as the secondary Bjerknes force, as described in the next paragraph. However, since added mass is also present in the absence of walls, the expression of added mass in an infinite volume of liquid can be used as an approximation to the added mass in an inkjet printhead.

Bjerknes forces are the unsteady buoyancy of a bubble. This force is decomposed into primary Bjerknes force and secondary Bjerknes force. These forces are distinguished by the effect that gives rise to the pressure gradient. The magnitude of the force F_{bj} on a bubble due to a given pressure gradient ∇P is given by Archimedes' law.

$$\mathbf{F}_{bj} = -V_b \nabla P \quad (6.8)$$

The pressure gradient that is not induced directly by the bubble volume oscillations gives rise to primary Bjerknes force. This pressure gradient is obtained by solving the axisymmetric Navier-Stokes equation numerically. The pressure gradient that is induced directly by the bubble volume oscillations gives rise to the secondary Bjerknes force. This pressure gradient is calculated by a three-dimensional potential flow calculation. The radial flow field that is generated by a bubble at position \mathbf{x}_b is characterized by the potential φ_d of a source singularity, which is modified by the walls.

$$\varphi_d(\mathbf{x}) = \frac{1}{4\pi(\mathbf{x}_b - \mathbf{x})^2} \frac{d}{dt} V_b \quad (6.9)$$

The total potential is the sum of the potential φ_d that is directly generated by the bubble expansion, and the modification to the potential φ_w by the walls and the free surfaces.

$$\varphi = \varphi_d + \varphi_w \quad (6.10)$$

The boundary conditions are imposed on the total potential, so that the boundary conditions on φ_w are inhomogenous. The field equation, Laplace's equation, is now solved for the potential by finite differencing, using second order central differences. The pressure gradient is then obtained from Bernoulli's equation.

$$P = P_0 - \rho \frac{d}{dt} \varphi_w - \frac{1}{2} \rho (\nabla \varphi_w)^2 \quad (6.11)$$

By separating the spatial part from the temporal part, a large part of the expression can be precomputed.

$$\varphi_w(\mathbf{x}, t) = \phi_w(\mathbf{x}) \frac{d}{dt} V_b(t) \quad (6.12)$$

With this decomposition, the pressure gradient can be written as the product of a vector field and the time derivatives of the bubble volume.

$$\nabla P = -\rho(\nabla\phi_w)\frac{d^2}{dt^2}V_b - \frac{1}{2}\rho\left(\nabla(\nabla\phi_w)^2\right)\left(\frac{d}{dt}V_b\right)^2 \quad (6.13)$$

The two spatial terms, both vectors with nonzero radial and axial terms, are only required at the bubble location. They are calculated at regularly spaced points prior to the main calculation, and interpolated during each time step for the location of the bubble to calculate the secondary Bjerknes force.

Lift is the result of the rotation of the velocity field, and the shear. When a bubble moves through a liquid, the liquid must flow around the bubble. This flow is a dipole in the potential flow approximation. Changes of this dipole field give rise to added mass. Since the bubble mass is negligible with respect to this added mass, the inertia of the bubble is completely contained in this dipole field. Rotation of the velocity field rotates the dipole field, and thus the bubble velocity, with the same rate. To maintain the direction of the bubble velocity with respect to an inertial reference frame, the velocity must be changed back to its original direction before the rotation. This velocity change requires a force to balance added mass. This force contributes to lift. The other contributions to lift arise due to the shedding of vorticity. Lift is characterized by the lift coefficient c_l , which is implicitly defined by the equation for lift.

$$\mathbf{F}_l = c_l\rho_l V_b \mathbf{u} \times \nabla \times \mathbf{u} \quad (6.14)$$

The competition between the two contributions results in a complex dependence of the lift coefficient on rotation rate, shear rate, and Reynolds number. The lift coefficient can even change sign. See van Nierop et al. [14] for a recent detailed treatment of lift for spherical bubbles, and Bluemink et al. [15] for a detailed study of lift on solid spheres. When the bubble is no longer spherical, the value of lift becomes even more complex. Lift is also very sensitive to surfactant concentration. These two complications have been studied extensively [17, 18]. These complications, and the nonavailability of a suitable expression for the lift force, require that the importance of lift should be established before this force is accurately included in the calculation. For now, we neglect lift. This approximation is checked by assuming a lift coefficient of $c_l = \frac{1}{2}$, and estimating the magnitude of lift with respect to the other forces from the calculated flow field. If lift turns out to be significant, an accurate expression is required.

Lubrication force \mathbf{F}_{lub} is a viscous force between the bubble and the wall. It is a result of the viscous friction in the layer of liquid between the bubble and the wall. When the bubble approaches a wall, the liquid in between is being pushed out, as shown in figure 6.1. This flow is governed by the standoff distance δ as shown in figure 6.1, the time derivative of the standoff distance, the bubble radius, and the viscosity. The pressure can be calculated by assuming lubrication flow and balancing viscous friction with the pressure gradient.

$$\mathbf{F}_{lub} \sim -\frac{\mu R^4}{\delta^3} \mathbf{e}_n \frac{d\delta}{dt} \quad (6.15)$$

The pressure is inversely quadratic in the standoff distance δ , so it is not necessary to derive the prefactor. A small change in standoff distance causes a large change in lubrication force. Therefore, the only effect of a different prefactor is

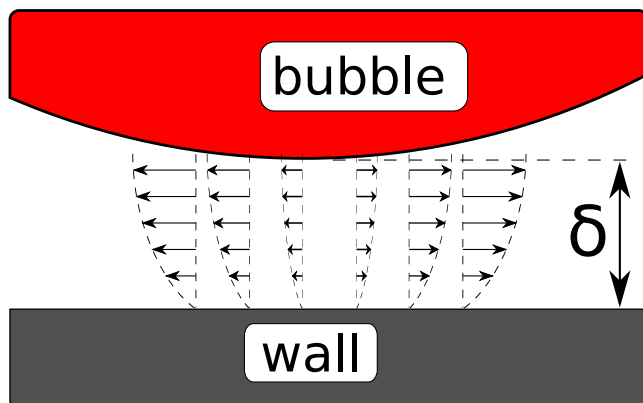


Figure 6.1: A bubble approaches a wall. Liquid flows radially outward from the region between the bubble and the wall. The standoff distance δ is the distance from the bubble to the wall.

a minute change in standoff distance. Since an accurate determination of the standoff distance itself is not the objective of this analysis, we will not derive the dimensionless prefactor.

The long term evolution of an air bubble in an inkjet printhead is dominated by the growth of the bubble due to rectified diffusion of gas towards the bubble. During most of its evolution, a bubble in an inkjet printhead is stationary. However, the bubble growth during the first few actuation cycles after air entrapment determines whether the bubble will grow, dissolve, or whether it is ejected. This growth is calculated in the numerical model. For the calculation of the bubble growth during these first few cycles, an expression for the gas exchange between the bubble and the ambient liquid was required. For the considered case, where the bubble translates and exhibits volume oscillations, such an expression was not available from the literature. Therefore, an expression for convection-diffusion from a sphere of a constant radius is modified to take the effect of the volume oscillations into account in the numerical model.

An approximate expression for gas exchange is derived by modifying an expression for diffusion and convection from a sphere in steady flow to incorporate the effect of volume oscillations. The Sherwood number Sh is a measure of the gas exchange.

$$Sh = \frac{1}{2\pi R_b D_m \Delta C} \frac{dN}{dt} \quad (6.16)$$

Feng and Michaelides [11] obtained an expression for the Nusselt number, which is completely analogous to the Sherwood number, for small but finite Reynolds numbers $Re < 1$ and large Péclet numbers $Pe > 10$ so that the diffusion boundary layer is thin.

$$Sh = 0.651\sqrt{Pe} \left(1.032 + \frac{0.61Re}{Re + 21} \right) + 1.60 - \frac{0.61Re}{Re + 21} \quad (6.17)$$

The number of moles of molecules in the bubble is denoted N , the mass diffusivity is denoted D_m , and ΔC is the difference in concentration between the

liquid in contact with the bubble wall and the liquid far away from the bubble. When the velocity vanishes, the Sherwood number $Sh_0 = 2$ can be calculated analytically. The expression by Feng and Michaelides is equal to $Sh_0 = 1.6$ for zero Reynolds number and zero Péclet number, which is fairly close to $Sh_0 = 2$, the exact value.

When the convective time scale is much smaller than the period of oscillation, the boundary layer is flushed away much quicker than the oscillation can modify it. In this limit, the diffusive boundary layer, and thus the mass transport, approaches the steady state value. Equation 6.17 can be used in this limit without modification for unsteady effects. The ratio of convective time scale over the period of oscillation is St , the Strouhal number.

$$St = \frac{R\omega}{u} \quad (6.18)$$

Equation 6.17 is valid in the limit of a small Strouhal number.

In the small Strouhal number limit, rectified diffusion can vanish completely. When the Reynolds number is small and the Péclet number is large, some terms in equation 6.17 can be neglected.

$$Sh = 0.651 \cdot 1.032\sqrt{Pe} \quad (6.19)$$

Insert the definition of the Sherwood number and the Péclet number to obtain a direct expression for the mass transfer rate.

$$Q = 2\pi\sqrt{D}h(P_0 - P_g + P_v)0.651 \cdot 1.032\sqrt{R^3u} \quad (6.20)$$

When added all the forces other than added mass are negligible, the force balance dictates that added mass is also negligible.

$$\mathbf{F}_m = -\frac{2}{3}\pi\rho_l \frac{d}{dt}(R^3\mathbf{u}) = 0 \Rightarrow R^3\mathbf{u} = R_0^3\mathbf{u}_0 \quad (6.21)$$

The velocity u_0 is the velocity of the bubble when its radius is $R = R_0$. Insert this expression into equation 6.20 to obtain a more convenient expression for the mass transfer.

$$Q = 2\pi\sqrt{D}h(P_0 - P_g + P_v)0.651 \cdot 1.032\sqrt{R_0^3u_0} \quad (6.22)$$

This expression shows that the mass transfer rate is independent of the radius fluctuation. The effect of the velocity on the mass transfer rate leads to enhanced dissolution. The growth due to the area effect is countered exactly by this enhanced dissolution, resulting in exactly the dissolution rate that would occur if the bubble would exhibit no volume oscillations at all. In the absence of volume oscillations, a bubble in a saturated or sub-saturated liquid dissolves.

The small Strouhal number limit might be irrelevant for a bubble in an inkjet printhead, except during the first few droplet formation cycles after its entrainment. When the bubble radius is $R = 10^{-5} m$, the frequency of oscillation is $\omega = 10^5 s^{-1}$, and the velocity is $u = 1 ms^{-1}$, the Strouhal number $St = 1$ is of order unity. Bubbles are expected to be smaller when they are entrained, perhaps by an order of magnitude. In the nozzle, the velocity is an order of magnitude larger. However, when the bubble enters the channel, the

velocity decreases by two orders of magnitude as a result of the smaller cross-sectional area. Since the radius eventually increases up to $R \sim 10^{-4} m$, the bubble is expected to grow to a radius of order $R \sim 10^{-5} m$ relatively early in its evolution. The expected result is that the small Strouhal number limit of quasisteady gas diffusion is relevant only during the first few droplet formation cycles after entrainment. Since the equilibrium volume change per cycle is very small - bubble growth to the diffusive equilibrium takes seconds - only the large Strouhal number regime is relevant. Unsteady effects will have to be taken into account.

The expression for convection-diffusion can be modified to take unsteady effects into account. The Péclet number is large, indicating the presence of a diffusion boundary layer. When the bubble expands, this boundary layer is stretched, so that it thins. This thinning increases the concentration gradient. The magnitude of this effect can be derived from the convection equation. Consider only the radial velocity and concentration derivative in spherical coordinates.

$$\partial_t C + u_r \partial_r C = 0 \quad (6.23)$$

The objective of this part of the analysis is the radial derivative of the concentration. Therefore, the radial derivative of this equation is taken.

$$\partial_r \partial_t C + \partial_r u_r \partial_r C = \frac{D}{Dt} \partial_r C + (\partial_r C) (\partial_r u_r) = 0 \quad (6.24)$$

The velocity field is the result of the bubble expansion.

$$u_r = \frac{1}{4\pi r^2} \frac{d}{dt} V_b = \frac{R_b^2}{r^2} \frac{d}{dt} R_b \quad (6.25)$$

The radial derivative of this velocity field can be evaluated at the bubble wall to obtain the radial derivative at the bubble wall.

$$\partial_r u_r = \frac{-2}{R_b} \frac{d}{dt} R_b \quad (6.26)$$

With this result, equation 6.24 can be solved for the normal derivative of the concentration as a function of the bubble radius.

$$\frac{\partial_r C(R_b)}{\partial_r C(R_0)} = \frac{R_b^2}{R_0^2} \quad (6.27)$$

If the volume fluctuations are fast with respect to the convective timescale, the constant radius gas flux per surface area can be multiplied with this factor to obtain the gas flux per surface area for the fluctuating radius. First calculate the constant radius Sherwood number $\widehat{\text{Sh}}$ that expresses the same gas flux per surface area, but with another reference length. This expresses a total gas flux that is larger by a factor $\frac{R_b^2}{R_0^2}$, which is the result of the area effect. The factor is the ratio of surface areas.

$$\widehat{\text{Sh}}(R_b) = \frac{R_b}{R_0} \text{Sh}(R_0) \quad (6.28)$$

Now multiply this constant radius Sherwood number by the correction factor for the thinning of the boundary layer.

$$\text{Sh}(R_b) = \frac{R_b^2}{R_0^2} \widehat{\text{Sh}}(R_b) = \frac{R_b^3}{R_0^3} \text{Sh}(R_0) \quad (6.29)$$

In the channel, the Strouhal number is expected to be large. This can be inferred from the magnitude of the velocity fluctuation in the channel. If the bubble were driven only by primary Bjerknes force and added mass, its velocity is of the same order of magnitude as the velocity of the liquid. This velocity is about $\tilde{u}_c \sim 0.1 \text{ m s}^{-1}$, so the convective timescale is about $100 \mu\text{s}$, which is much larger than $\omega^{-1} \sim 1 \mu\text{s}$, the time scale of the pressure fluctuations. In the nozzle near the meniscus, these time scales are equal. However, when the bubble is that close to the meniscus, the pressure fluctuation is very small, so that the bubble volume oscillations are small and the correction is small, so that the inaccuracy in the correction for this case is irrelevant. An as yet unresolved issue is whether the unsteadiness in the concentration difference is correctly taken into account. An indication that this is indeed the case is that for vanishing Péclet numbers, the expression agrees with the result by Fyrillas and Szeri [21] insofar as that the gas exchange per cycle is a weighted average of the gas pressure in the bubble with $\frac{R^4}{R_0^4}$ as weighing factor. Equation 6.29 specifies a correction to the Sherwood number for the effect of bubble volume oscillations that is expected to be valid for all conditions that will be encountered in an inkjet printhead.

The obtained ODE's are integrated numerically with a Runge-Kutta method, in conjunction with the channel acoustics, nozzle flow and volume oscillations that were described in chapter 5. This yields the position and velocity in cylindrical coordinates as a function of time, where $z = 0$ is defined at the end of the nozzle and the positive direction is towards the channel.

6.3 Theoretical predictions

The order of magnitude of the forces are estimated by analytical methods. These predictions are used to interpret the results of the numerical model, and to evaluate the validity of assumptions. First, the magnitude of Bjerknes forces over viscous friction is estimated. Second, the assumption that lift is small is checked.

For smaller bubbles, the magnitude of acoustic forces with respect to viscous drag is smaller. The force on the bubble is $F_p = \frac{4}{3}\pi R^3 \partial_x P$ due to the pressure gradient. The viscous drag can be estimated with Stokes drag $F_d = 4\pi\mu R u$. The ratio of viscous drag over primary Bjerknes force is large for small bubbles.

$$\frac{F_d}{F_p} = \frac{3\mu}{R^2\omega\rho} \quad (6.30)$$

Viscous friction dominates primary Bjerknes force for small bubbles $R \ll 10 \mu\text{m}$, where a frequency of $\omega = 3 \cdot 10^5 \text{ s}^{-1}$ was assumed.

To estimate the magnitude of secondary Bjerknes force, consider the velocity field due to a bubble near a flat, infinite wall. The secondary Bjerknes force on this bubble can be calculated with the method of images. The component of the velocity field at the bubble due to the image bubble is spherically symmetric about the location of the image bubble.

$$u_n = \frac{\pi}{\delta^2} \frac{d}{dt} V_b \quad (6.31)$$

In this expression, u_n is the velocity of the liquid in the normal direction. The finite size of the bubble is neglected, so that the distance δ is the distance from the center of the bubble to the wall. The bubble volume V_b is the only time-dependent quantity in this analysis. Since this estimate is mostly relevant for small bubbles, assume that the bubble volume fluctuation is of the same order of magnitude as the bubble volume. The pressure consists of the unsteady pressure, the component of the pressure that is linear in the velocity amplitude, and the steady pressure that is quadratic in the velocity amplitude. Far from the wall, $\omega\delta \gg u$ so that the unsteady pressure dominates. This condition can be inserted into equation 6.31 to obtain an explicit condition on the distance to the wall.

$$\delta \gg R \sqrt[3]{\frac{16}{3}\pi^2} \approx 4R \quad (6.32)$$

This condition is assumed to be satisfied, so the steady pressure is neglected.

$$\partial_n P = -\frac{\pi\rho}{\delta^2} \frac{d^2}{dt^2} V_b \quad (6.33)$$

Multiply this pressure gradient with the bubble volume to obtain an order of magnitude estimate of the ratio of drag over secondary Bjerknes force.

$$\frac{F_d}{F_{\text{sec}}} = \frac{4\mu R u \delta^2}{\rho \omega^2 V_b^2} \quad (6.34)$$

Similar to primary Bjerknes force, the ratio of viscous drag force over secondary Bjerknes force is large for small bubbles. When the bubble volume oscillations are not limited by the volume of the acoustics, the ratio of viscous drag over secondary Bjerknes force is proportional to R^{-5} , which is a fairly large power. Therefore, the transition between dominance of viscous drag to dominance of secondary Bjerknes force is likely to be very sharp.

$$R > \sqrt[5]{\frac{3\mu u \delta^2}{\pi\rho\omega^2}} \approx 10 \mu m \Rightarrow F_d \ll F_{\text{sec}} \quad (6.35)$$

In the numerical evaluation of the estimate, the channel radius was used as the magnitude of the distance to the wall. For bubbles larger than $R = 10 \mu m$, acoustic forces dominate viscous drag.

Lift was neglected, and this assumption is now tested. The importance of lift can be determined from the calculated velocity field in the nozzle. Assume a lift coefficient of $c_l = \frac{1}{2}$ in this order of magnitude estimate. The ratio of lift over added mass is equal to the ratio of vorticity over angular frequency of the flow.

$$\frac{F_l}{F_{am}} = \frac{\nabla \times u}{\omega} \quad (6.36)$$

The magnitude of this quantity is shown in figure 6.2. Where this quantity is of order unity or larger, lift is relevant. Lift is relevant in the boundary layer at the nozzle wall and in a region that protrudes from the nozzle to about $z = 50 \mu m$. Within these regions, the behavior of an air bubble might be different from the results of the simulation. Outside of these two regions, the model is expected to be valid.

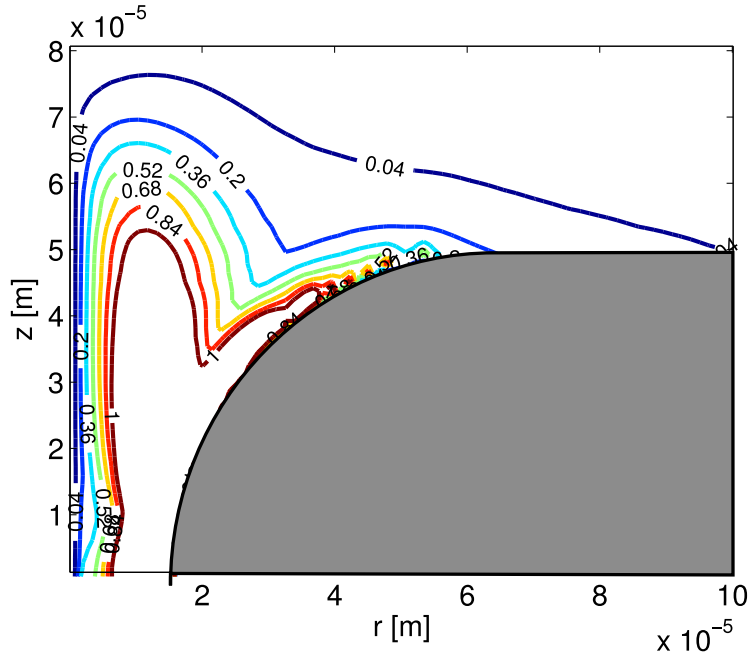


Figure 6.2: Contour plot of vorticity over the characteristic frequency of the flow, which is $\omega = 5 \cdot 10^5 \text{ s}^{-1}$, indicating the magnitude of lift over added mass.

6.4 Results of the numerical model

The numerical model is used to study the behavior of a bubble in an inkjet printhead. First, the flow field in the nozzle is examined. Second, the translation of a bubble per droplet formation cycle is calculated. Third, the growth of the bubble is calculated.

The velocity field inside the nozzle where no bubble is present, is calculated and analysed. The mean velocity field is shown in figure 6.3, in the top figure. Streamlines are drawn at regular intervals. Since the flow field is axisymmetric, the body of revolution of a streamline about the axis is a streamtube. The volume flow rate between two neighboring streamtubes is equal. A vortex with closed streamlines is present in the mean flow. A saddle point is located near $z = 25 \mu\text{m}$ from the nozzle end. At the bottom of figure 6.3, the Lagrangian transport field is shown. This is the translation of the fluid particles over one droplet formation cycle. A fluid particle that starts near the meniscus will end up at about $z = 80 \mu\text{m}$ after one cycle. In other words, it traverses the entire nozzle in one cycle. Outside of the nozzle, the translation is about $\Delta x = 1 \mu\text{m}$ per cycle. The saddle point near at $z = 25 \mu\text{m}$ is not present in the Lagrangian transport field. At the end of the nozzle, all transport vectors point towards the origin. This is an artifact from the method of calculation. Particles that are ejected from the nozzle, end up at the origin in the simulation, although this motion is not physical. The differences between the Lagrangian transport field and the mean flow are the result of the discrete nature of the transport. The fluid particles move in discrete steps, one step per cycle. If the translation per

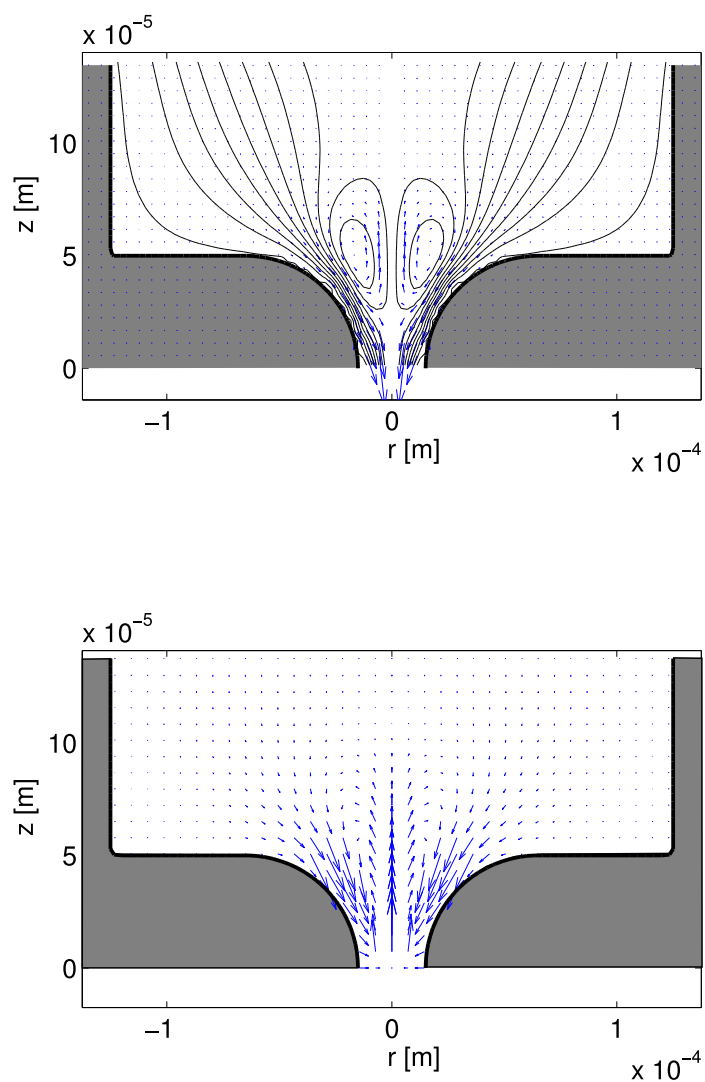


Figure 6.3: The mean velocity without an entrained air bubble (top, arrows and streamlines) and the Lagrangian transport per droplet formation cycle (bottom, arrows). The Lagrangian transport was scaled to prevent cluttering of the arrows. The largest translation per cycle is about $80 \mu\text{m}$. The mean flow has a saddle point near $z = 25 \mu$. This saddle point is absent in the Lagrangian transport. Both the mean flow and the Lagrangian transport field

cycle is small with respect to the extent of the domain, the mean flow and the Lagrangian transport are nearly the same. This occurs in the channel. In the nozzle, the Lagrangian transport is very different from the mean flow.

Very small bubbles, for which viscous drag dominates acoustic forces, behave almost like fluid particles. The translation of a bubble per cycle closely follows the Lagrangian transport field. With increasing bubble radius, the difference between these two fields increases.

To analyse the translation of a bubble per cycle, the translation of the bubble per droplet formation cycle was calculated at many positions throughout the nozzle. At these positions, the simulation is run for one $100 \mu\text{s}$ period, with one actuation pulse of the same type as in chapter 5. The initial position and the final position are compared. The results are shown in figures 6.4, 6.5, 6.6, and 6.7, where the translation of a bubble per cycle is shown. These figures were interpreted to draw (by hand) the corresponding phase portraits, of which the equilibria and trajectories are shown.

Small bubbles are almost passively convected with the liquid, as shown in figures 6.4 and 6.5. The translation direction and magnitude of a $R = 2 \mu\text{m}$

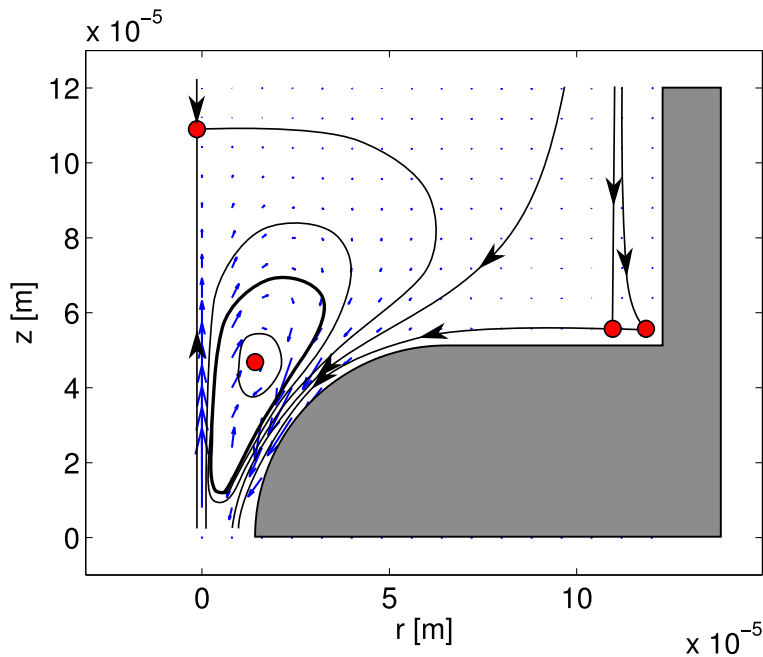


Figure 6.4: Translation of a bubble per acoustic cycle (arrows) and phase portrait for a bubble radius of $R = 2 \mu\text{m}$. The equilibria are indicated by dots and trajectories are drawn (lines). The bubble is nearly stationary anywhere but in the nozzle, where the liquid velocity is large. A saddle point is present near $r = 0$, $z = 110 \mu\text{m}$. A spiral is located near $r = 15 \mu\text{m}$, $z = 50 \mu\text{m}$, although it is hard to discern whether it is unstable or stable. It is drawn as a center. The unstable manifold of the upper saddle point either ends in the limit cycle or it runs into the meniscus. Near the corner, a stable point and a saddle point are present.

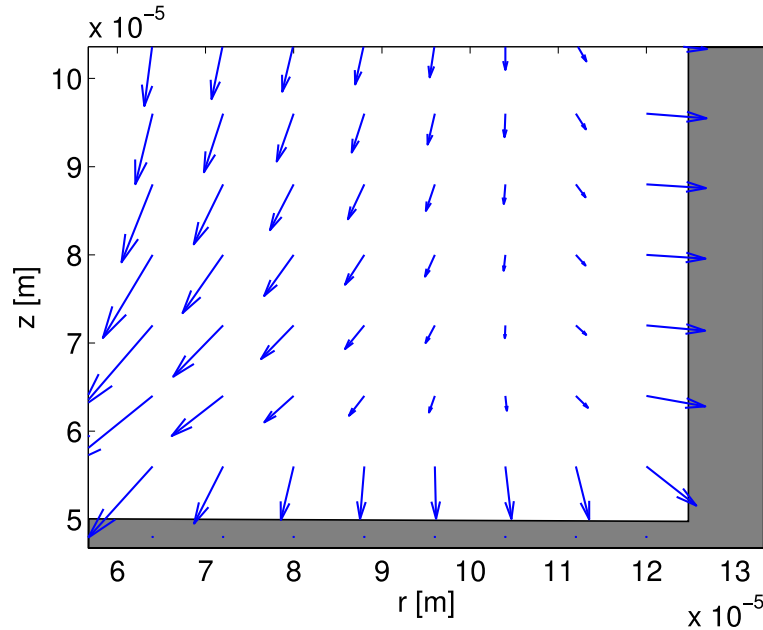


Figure 6.5: Translation of a bubble per acoustic cycle for a bubble radius of $R = 2 \mu\text{m}$, showing details of the the behavior near the corner. The corner is a stable point. About $20 \mu\text{m}$ towards the axis is a saddle point. We expect that the presence of the stable point is a result of secondary Bjerknes force. This force is small for such a small bubble, but in the absence of any other forces, it is still dominant near the corner.

bubble closely resemble the Lagrangian transport field. A center is located near $r = 15 \mu\text{m}$, $z = 50 \mu\text{m}$. A saddle point is present near $r = 0$, $z = 110 \mu\text{m}$ with the stable manifolds in the axial direction. The unstable manifold appears to end in a limit cycle. Near the corner, a stable point and a saddle point are present. Whether the trajectory that appears to be a limit cycle is indeed one, or a center or perhaps a stable or unstable spiral, is hard to discern from the calculated translation map. This is not essential since the bubble doesn't exactly follow the phase portrait.

If the bubble were to follow the trajectories of the phase portrait exactly, a $R = 2 \mu\text{m}$ bubble would move from the meniscus towards the upper saddle point, and then back towards the meniscus where it would be ejected, or it might be caught into the limit cycle. However, the bubble evolution can be chaotic since the bubble trajectory consists of a series of discrete events, the droplet formation cycles. A bubble does not follow the manifolds of the phase portrait exactly, but it moves in the direction indicated in the phase portrait in discrete finite steps. The bubble can therefore cross manifolds. A bubble can move from the unstable manifold of the upper saddle point towards the meniscus, and then cross into the closed orbits around the center. The bubble can also leave these closed orbits by crossing manifolds. The exact evolution is sensitive to the location of the bubble. Once the bubble has left the basin

of attraction of the limit cycle, it is ejected. If all bubbles would eventually be ejected, there would not be a problem with bubbles in inkjet printing. However, the phase portrait changes as the bubble grows.

The phase portrait at a bubble radius of $R_0 = 5 \mu m$ is qualitatively different from the phase portrait of a $R_0 = 25 \mu m$ bubble, see figure 6.6. Saddle points are present on the axis at $z = 110 \mu m$ from the end of the nozzle, and on the nozzle wall. The unstable manifold from the saddle point on the axis enters a stable point in the corner after approaching the saddle point on the nozzle wall closely. Apparently, between a bubble radius of $R_0 = 2 \mu m$ and $R_0 = 5 \mu m$, a global bifurcation has occurred. The saddle point at the nozzle wall is now connected to the basin of attraction of the limit cycle. Whether the limit cycle is still present is unclear. The limit cycle, if it still is one, now extends beyond the end of the nozzle.

When a bubble with a radius of $R = 10 \mu m$ is entrained, its position determines whether it enters the channel, or whether it is ejected immediately. Close to the nozzle is a saddle point at the axis and an unstable point at the nozzle wall. An entrained bubble will always be ejected quickly when it is in the region that is bounded by the channel wall, the meniscus, and the stable manifold of this saddle point. A bubble with a radius of $R = 10 \mu m$ can only remain in the printhead for more than a few droplet formation cycles if the process of air entrainment leaves the bubble beyond the saddle point near the nozzle, about $z = 20 \mu m$ from the nozzle end. When the bubble is entrained beyond the saddle point, it first moves into the channel. Two forces act in this direction. The first is secondary Bjerknes force, which pushes the bubble away from the free surface of the meniscus. The second force is viscous drag, which pushes the bubble into the channel since the mean flow along the axis is directed towards the channel as a result of microstreaming. This is shown in figure 6.3. If the bubble is entrained beyond the saddle point near the meniscus, it will enter the channel and approach the saddle point in the channel near $z = 110 \mu m$. The radial position of the bubble will then increase exponentially while the distance to the saddle point in the axial direction decreases exponentially. The bubble moves away from the saddle point in the radial direction and moves towards the corner. This corner is a stable equilibrium position for all bubble volumes that can be attained, since the only force that is significant in the corner is secondary Bjerknes force, unless the bubble touches the wall. Secondary Bjerknes force pushes the bubble towards walls, and thus into the corner. The pressure gradient vanishes in the corner, so primary Bjerknes force vanishes also. The liquid velocity vanishes in the corner so viscous drag can not remove the bubble from the corner. Added mass and history force vanish because the bubble velocity vanishes. The bubble will stay in the corner, kept in place by secondary Bjerknes force and the lubrication force. In this corner, the bubble grows until the actuation is stopped.

Besides the translational motion, the bubble also exhibits growth. As the bubble radius changes, the phase portrait changes. The growth rate of a bubble depends on its size, as shown in figure 6.8. Very small bubbles are limited in their volume oscillations by surface tension. As a result, they dissolve. Such small bubbles are small enough to neglect their influence on the pressure, the two-way coupling that was treated in chapter 5. Their growth is accurately described by an analysis in which the bubble is assumed to be embedded in an infinite volume of liquid. Indeed, such a small-bubble limit to rectified diffusion was

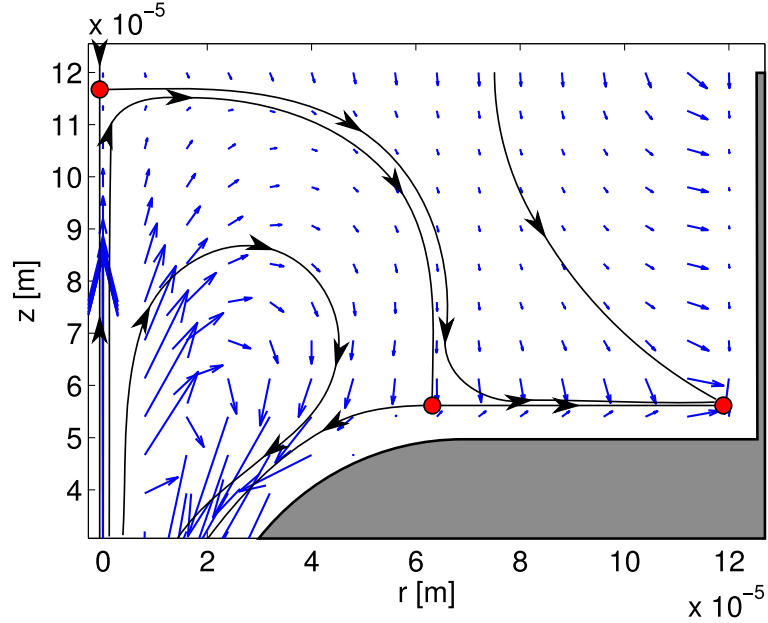


Figure 6.6: Translation of a bubble per acoustic cycle for a bubble radius of $R_0 = 5 \mu m$. The corner is still a stable point and the saddle point on the axis is also still present. The saddle point that was near the corner at a bubble radius of $R_0 = 5 \mu m$ has moved along the nozzle wall towards the meniscus. The unstable manifold from the saddle point on the axis now approaches the saddle point on the nozzle wall, and leaves the saddle point in the direction of the corner, while for $R_0 = 2 \mu m$, it ran towards the limit cycle.

found in previous studies [20], where it was identified with the Blake threshold. Very large bubbles are limited in their volume oscillations by the finite volume of the incoming acoustic wave. At the diffusive equilibrium, the ratio of volume of the acoustic wave over bubble volume is small.

$$\Pi_7 = \frac{R_c^2 P_a}{\rho_l c \omega R_0^3} = 0.1 \quad (6.37)$$

This suggests that the finite volume of the acoustic waves in the channel determines the upper limit of bubble growth.

Since there is no chance of ejecting the bubble when it has grown to $R = 10 \mu m$, the time it takes to grow to this size determines the chance of recovery by ejecting the bubble. For a bubble between $R = 1 \mu m$ and $R = 10 \mu m$, the growth rate is $\Delta V_b \sim 0.05 pl$ per cycle. A radius of $R = 10 \mu m$ corresponds to a volume of $V_b = 4 pl$, so growth to $R = 10 \mu m$ takes about 100 actuation cycles. After a hundred actuation cycles after the air entrainment, the bubble cannot be ejected anymore.

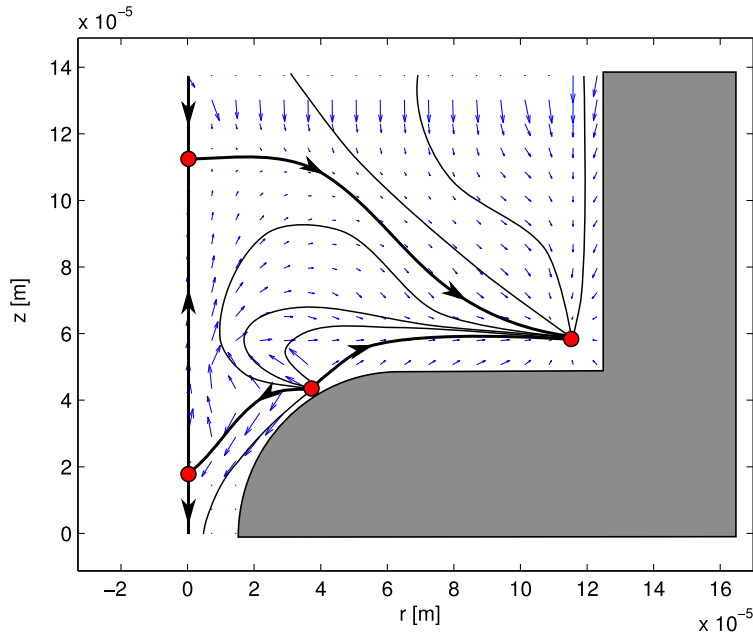


Figure 6.7: Translation of a bubble per acoustic cycle for a bubble radius of $R = 10 \mu m$. At $z = 40 \mu m$, $r = 40 \mu m$ is an unstable point. Close to the meniscus, at $z = 18 \mu m$ on the axis, there is a saddle point, where the unstable manifolds run along the axis and the stable manifolds run towards the axis. Following the unstable manifold further into the nozzle, another saddle point is encountered at $z = 115 \mu m$, in the channel. The stable manifolds of this saddle point run along the axis and the unstable manifolds run away from the axis. Following the unstable manifold, a stable point is encountered in the corner.

6.5 Conclusion

The translation was calculated from a force balance. Secondary Bjerknes force, added mass, history force, and viscous friction are different when the volume of ambient liquid is made finite. Unlike the other forces, Secondary Bjerknes force requires the influence of walls and free surfaces to be taken into account, since it is a direct result of the interaction between the bubble and the walls and free surfaces. Secondary Bjerknes force is an inviscid force, and can therefore be obtained from the bubble volume and position, the flow field, and the first and second derivatives of these quantities. A method to calculate this force was developed and an implementation in a numerical model was demonstrated for the complex case of a bubble in an inkjet printhead.

The translation and growth of a bubble in an inkjet printhead were calculated with a numerical model. This model predicts that when a small bubble ($R = 2 \mu m$) is entrained, it enters a limit cycle near a region where the bubble trajectory intersects the meniscus. With these small bubbles, there is a chance that they are ejected during each turn over the limit cycle. As the bubble grows, the limit cycle disappears at a bubble radius between $R_0 = 5 \mu m$ and

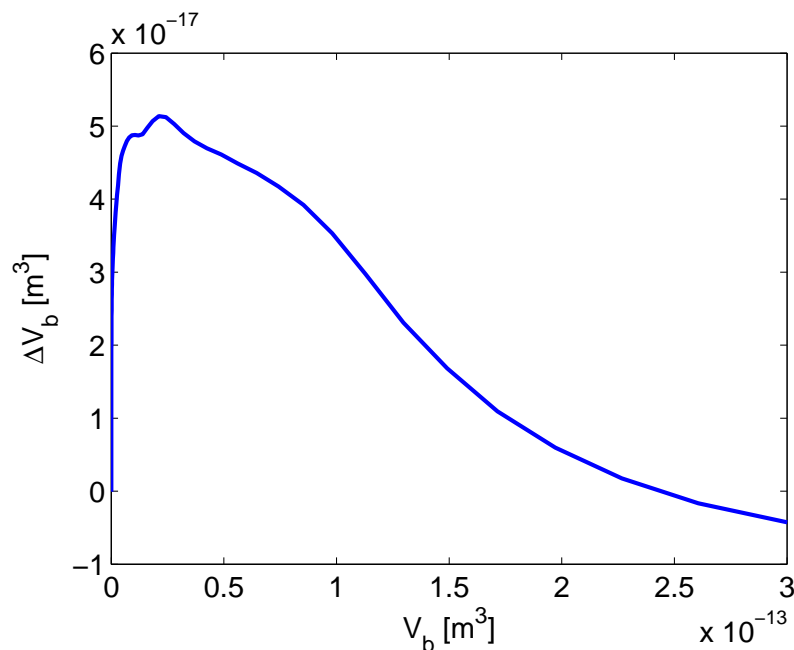


Figure 6.8: Volume growth per acoustic cycle versus bubble volume for a bubble in the channel at $r = 70 \mu m$ and $z = 70 \mu m$. The droplet production rate was $20 kHz$. The two zero-crossings at $V_b = 11 \cdot 10^{-19} m^3$ and $V_b = 244 \cdot 10^{-15} m^3$ are equilibria in the growth. The equilibrium at $V_b = 11 \cdot 10^{-19} m^3$, which corresponds to a radius of $R_b = 0.6 \mu m$, is an unstable point. The equilibrium at $V_b = 244 \cdot 10^{-15} m^3$, which corresponds to a radius of $R_b = 39 \mu m$, is a stable point.

$R_0 = 10 \mu m$. This takes about a hundred actuation cycles. After the limit cycle has been destroyed, the bubble will always end up in the corner. These larger bubbles do not enter the channel if they are entrained less than $20 \mu m$ from the end of the nozzle. In this case, they are ejected during the next droplet formation cycle. When a bubble ends up in the corner, it grows to a radius of $R = 39 \mu m$, where the bubble growth exhibits a stable equilibrium. The growth is limited by the volume of the acoustic field.

The numerical model that was used in this research contains many approximations. For instance, the bubble is represented as a particle with point forces, lift was neglected, and the meniscus dynamics were approximated with the method that was described in chapter 5. Whether all the approximations are justified, can only be truly established by an experimental validation. A direct observation of the path of a bubble in an inkjet printhead is difficult, but it can be done, as shown in chapter 4. A high-speed image recording of a bubble that is being entrained into an inkjet printhead is required, at a sufficiently high resolution to detect a $R = 2 \mu m$ bubble. A full direct numerical simulation of the complete two-phase flow problem provides a more limited, but still valuable validation. In the nozzle, a direct numerical simulation is expected to be the most

economical approach. Depending on whether the predictions of the presented numerical model turn out to be correct or not, the predictions of the numerical model will either provide an interpretation of those empirical observations, or they indicate which assumptions should be checked.

Bibliography

- [1] J. de Jong, R. Jeurissen, H. Borel, M. van den Berg, M. Versluis, H. Wijshoff, A. Prosperetti, H. Reinten, D. Lohse *Entrapped air bubbles in piezo-driven inkjet printing: Their effect on droplet velocity*, Phys. Fluids **18**, 121511 (2006).
- [2] C.E. Brennen *Cavitation and Bubble Dynamics*, Oxford University Press (1995).
- [3] T.G. Leighton *The acoustic bubble*, Academic Press, (1997).
- [4] D. Lohse, A. Prosperetti *Controlling bubbles*, J. Phys.: Condens. Matter **15**, 415-420 (2003).
- [5] C.W.M. van der Geld *On the motion of a spherical bubble deforming near a plane wall*, J. Eng. Math. **42**, 91-118 (2002).
- [6] G. Mougin, J. Magnaudet *Path Instability of a Rising Bubble*, Phys. Rev. Lett. **88**, 014502 (2001).
- [7] F. Takemura, J. Magnaudet *The transverse force on clean and contaminated bubbles rising near a vertical wall at moderate Reynolds number*, J. Fluid Mech. **495**, 235-253 (2003).
- [8] T.G. Leighton, P.R. White, C.L. Morfey, J.W.L. Clarke, G.J. Heald, H.A. Dumbrell, K.R. Holland *The effect of reverberation on the damping of bubbles* J. Acoust. Soc. Am. **112** 1366-1376 (2002).
- [9] R. Jeurissen, J. de Jong, H. Reinten, M. van den Berg, H. Wijshoff, M. Versluis, D. Lohse *Effect of an entrained air bubble on the acoustics of an ink channel*, J. Acoust. Soc. Am. **123**, 2496-2505 (2008).
- [10] L.F. Shampine, S. Thompson, *Solving DDEs in MATLAB*, Appl. Num. Math. **37**, 441-458 (2001).
- [11] E.E. Michaelides *Hydrodynamic Force and Heat/Mass Transfer From Particles, Bubbles, and Drops The Freeman Scholar Lecture* J. Fluids Eng. **125**, 209238 (2003).
- [12] R. Toegel, S. Luther, D. Lohse *Viscosity destabilizes sonoluminescing bubbles*, Phys. Rev. Lett. **96**, 114301 (2006).
- [13] J. Magnaudet, D. Legendre *The viscous drag force on a spherical bubble with a time-dependent radius*, Phys. Fluids **10** (1998).

- [14] E. van Nierop, S. Luther, J. Bleumink, J. Magnaudet, A. Prosperetti, D. Lohse *Drag and lift forces on bubbles in a rotating flow*, J. Fluid Mech. **571**, 439454 (2007).
- [15] J.J. Bluemink, D. Lohse, A. Prosperetti, L. van Wijngaarden *A sphere in a uniformly rotating or shearing flow*. *Journal of Fluid Mechanics*, J. Fluid Mech. **600**, 201233 (2008).
- [16] P. Marmottant, M. Versluis, N. de Jong, S. Hilgenfeldt, D. Lohse *High-speed imaging of an ultrasound-driven bubble in contact with a wall: Narcissus effect and resolved acoustic streaming*, Exp. Fluids **41**, 147153 (2006).
- [17] C. Veldhuis, A. Biesheuvel, L. van Wijngaarden *Shape oscillations on bubbles rising in clean and in tap water*, Phys. Fluids **20**, 040705 (2008).
- [18] G. Mougin, J. Magnaudet *Path Instability of a Rising Bubble*, Phys. Rev. Lett. **88**, 014502 (2002).
- [19] C.D. Ohl, A. Tijink, A. Prosperetti *The added mass of an expanding bubble* J. Fluid Mech. **482**, 271290 (2003).
- [20] O. Louisnard, F. Gomez *Growth by rectified diffusion of strongly acoustically forced gas bubbles in nearly saturated liquids* Phys. Rev. E **67**, 036610 (2003).
- [21] M.M. Fyrillas, A. Szeri *Dissolution or growth of soluble spherical oscillating bubbles* J. Fluid Mech. **277**, 381407 (1994).

Chapter 7

Decoupling of Marangoni flow translation and capillary spreading of a droplet¹

When a droplet moves over a completely wetting solid substrate, whether by gravity, shear stress due to air flow, or inertia, the droplet spreads. Typically, the order of magnitude of the spreading speed is coupled to the translational speed. However, when a droplet is moved by surfactant driven Marangoni flow, the spreading speed and the translation speed are completely decoupled. We investigate this unique regime in which the time scale of droplet translation is many orders of magnitude larger or smaller – depending on the droplet size – than the spreading speed. We find that the divergence of the surface velocity in thin film Marangoni flow vanishes. As examples of how these results make flows tractable by analytical methods, the translation of a ridge and the development of a fingering instability are analyzed. The analysis of the fingering instability is corroborated by an experimental observation of the fingering instability.

7.1 Introduction

Marangoni flow is flow driven by a surface tension gradient, also known as “Marangoni stress”. The spatial variation of the surface tension can arise due to temperature differences or due to differences in surfactant concentration. This paper focuses on Marangoni flow due to surfactants.

Thin film Marangoni flow is important in many technical and biological applications. Surfactants are commonly used to stabilize foams, where the Marangoni stress keeps the liquid films from draining. Marangoni Stress keeps the

¹This chapter will evolve towards a manuscript to be submitted to Phys. Rev. E: Roger Jeurissen, Anette Hosoi, Gareth McKinley, *Decoupling of Marangoni flow translation and capillary spreading of a droplet*.

alveoli in our lungs from collapsing ([1], page 405). In lab on a chip applications, liquid needs to be transported. Marangoni flow can be a useful transport method in lab-on-a-chip applications [2].

Marangoni flow can also be a problem. In inkjet printing, Marangoni stress is one of the driving forces of flow towards the nozzles, along with shear stress of air flow [3]. This flow transports dirt and other contaminants towards the nozzles. This dirt may cause air bubble entrainment which in turn causes nozzle failure. Nozzle failure is the limiting factor for performance. The relevance for inkjet printing motivated this research.

An excellent review on thin film flows is written by Oron, Davis, and Bankoff [4]. They discuss investigations of droplet spreading for the cases of constant surface tension, thermocapillary flow, and an evaporating droplet. For the complete wetting case, only spreading at constant surface tension is discussed. The effect of surfactants on the evolution of a film is discussed in this review for a film on a substrate to which a surfactant rich droplet is added. Surfactants can be used to promote spreading of a droplet [5,6]. However, the effect of Marangoni stress on the spreading of a droplet that completely wets the substrate, without the local addition of surfactant, has not been investigated.

In this research, a droplet that is translated by Marangoni flow is studied experimentally and analytically. With the aid of the obtained results, complicated flows become tractable by analytical methods. This is demonstrated by analyzing a fingering instability that develops at the leading edge of a translating ridge. Finally, the predicted evolution is compared to experimental data.

A stationary droplet on a completely wetting substrate is a slow transient state. On a completely wetting substrate, a droplet will spread until it covers the entire surface. The spreading is described by Tanner's law [7], which follows from balancing Laplace pressure and viscous friction.

$$T \sim \frac{\mu}{V_d^3 \sigma_0} L^{10} \quad (7.1)$$

In this equation, T is the time scale, μ is the dynamic viscosity, V_d is the droplet volume, σ_0 is the surface tension, and L is the horizontal length scale, the droplet radius. The time scale is proportional to the horizontal length scale to a high power. After a small period of time after droplet deposition, the horizontal length scale is essentially constant unless forces other than Laplace pressure are relevant.

On a completely wetting substrate, droplet translation by a uniform body force or a uniform surface traction induces spreading of the same order of magnitude as the translation. These cases are common. Gravity is a uniform body force that translates a droplet over an inclined plane. The shear stress is nearly constant over a thin droplet under a laminar air flow. The case of a uniform body force is described by Burgers' equation in the square of the layer thickness. The case of a uniform surface traction is governed by Burgers' equation in the layer thickness. In both cases, the velocity is small at the trailing edge while a shock forms at the leading edge, as shown in figure 7.1. The leading edge is much faster than the trailing edge so a droplet is not truly translated by these forces, it is smeared out.

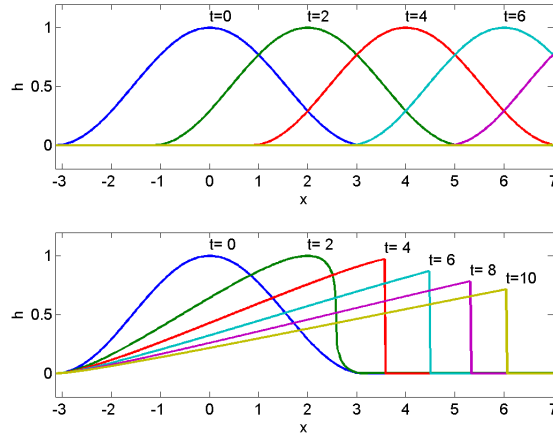


Figure 7.1: Two 2-dimensional droplets, one is moved by Marangoni flow (top), and the other (bottom) is moved by a constant shear stress at the surface. Six instants in time are shown, from 0 to 10 times the horizontal length scale over velocity.

7.2 Experimental observation of a translating droplet

Whether Marangoni flow shares the property of smearing out the droplets that it translates, is investigated experimentally on an inkjet printhead. The relevant part of the print head is shown in figure 7.2. This setup is described in de Jong et al. [8]. The nozzle plate is made out of nickel, and the ink is a wax with a melting point of about 80 degrees Celsius. All experiments were performed at a temperature of 130 degrees Celsius, well above the melting point of the ink. At this temperature, the ink is Newtonian with a viscosity of $\mu = 0.01 \text{ Nm}^{-2}\text{s}$. The surface tension is $\sigma_0 = 0.025 \text{ Nm}^{-1}$. The investigated Marangoni flow occurs at the nozzle plate, on the outside of the print head.

Marangoni flow towards any nozzle can be invoked. This phenomenon is described and analysed by de Jong et al. [8]. The hypothesis that the observed flow was surfactant concentration driven Marangoni flow, is supported by induction. This hypothesis was tested by replacing the ink with silicone oil. After this intervention, no flow was observed anymore. An incomplete explanation of the mechanism that leads to this Marangoni flow is presented by de Jong et al. Over most of the length of each channel, the cross-section can be changed slightly by a piezo actuator. This causes acoustic waves in the channel which set the ink in the nozzle that is connected to the channel in motion. This motion increases the surface tension of the ink on the nozzle plate in the direct vicinity the nozzle. The change in surface tension leads to Marangoni flow in the precursor film and ultimately to Marangoni flow in the band of ink at the center of the nozzle plate. Droplets on the precursor film are also moved by the Marangoni stress. This was observed in the same investigation, but not mentioned in [8].

A droplet that is moved over the nozzle plate by Marangoni flow is observed.

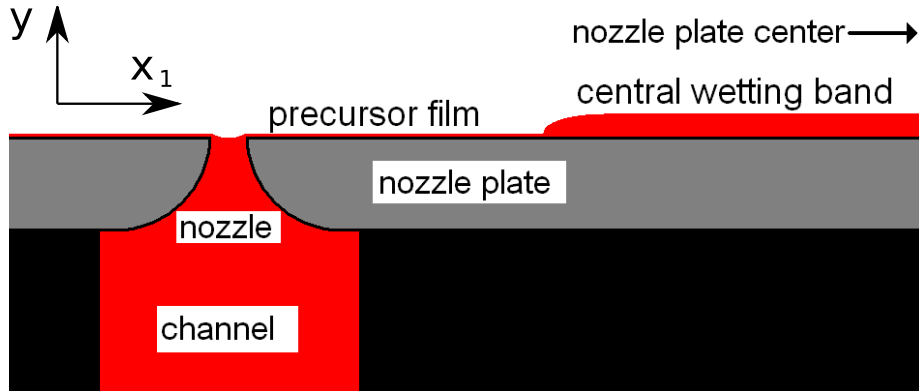


Figure 7.2: The experimental setup is an inkjet print head. The observed flows occur on the outside of the print head, in a thin layer of ink on the nozzle plate. Each nozzle is backed by a channel. Through the precursor film, the central wetting band and droplets (not shown) are connected to the nozzle.

The system is illuminated by a LED that emits light at a wavelength of $\lambda = 545 \text{ nm}$. The index of refraction of the ink is $n = 1.3$, so the thickness is 105 nm at the first dark fringe, 314 nm at the second dark fringe, and 524 nm at the third dark fringe. Six images of the experiment are shown in figure 7.3. When none of the nozzles is actuated, the droplet moves to the center of the nozzle plate, upwards in the images. A similar flow towards the center of the nozzle plate has been observed by de Jong et al. [8], but no explanation was given. This flow is subject to the same conditions as the flow towards the nozzle, and vanishes when the ink is replaced by silicone oil, as in the Marangoni flow towards the nozzle. We therefore assume that this flow towards the center of the nozzle plate is also surfactant driven Marangoni flow.

When one of the nozzles is actuated, the droplet moves towards this nozzle. The nozzle in the bottom center of the image is actuated first. Second, the nozzle in the lower right corner is actuated, and finally the nozzle in the bottom left corner is actuated. The droplet traverses a total distance of $500 \mu\text{m}$ during the part of the experiment that is shown in figure 7.3. Careful examination reveals that the droplet spreads ever so slightly. The last remnant of the third dark fringe in the first image, the small dark dot in the center of the droplet, disappears over the course of the experiment. The second dark fringe in the first image closes upon itself during the experiment, until an elongated dark spot in the last image remains. Apparently, the height decreases. From continuity, the decrease in height requires an increase in horizontal extent. The droplet must have spread.

By manually selecting the lowest dark fringe in the images, the surface area of the droplet can be determined. This procedure was applied to 22 of the frames at equidistant times. A horizontal length scale can be determined from the obtained surface area. The chosen length scale is the radius of a circle with the same area as the droplet. This effective radius is plotted in figure 7.4, along with the evolution of the radius of a droplet according to Tanner's law. The error margin is the thickness of the lowest dark fringe in the images, about two

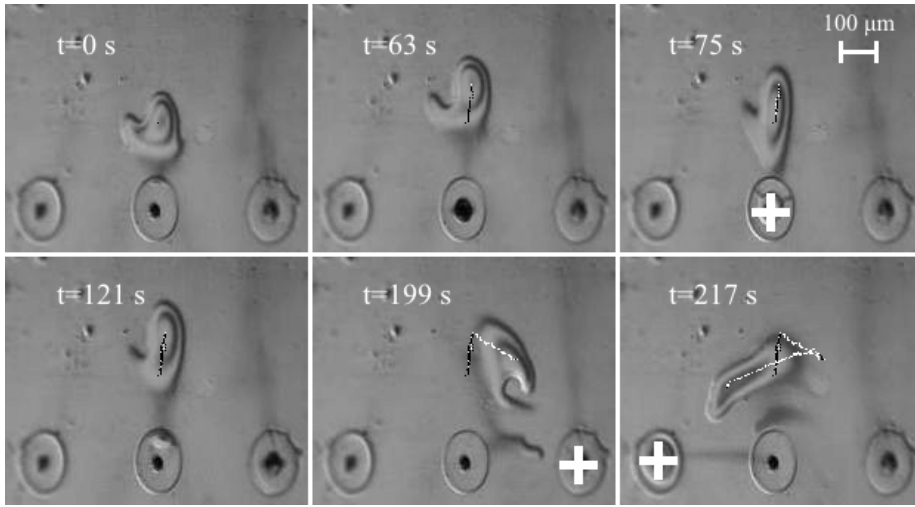


Figure 7.3: Six frames from a video recording of a droplet on a nickel nozzle plate are shown. The droplet is moved about by Marangoni flow. Actuated nozzles are marked by a plus (+) sign. The path of the top of the droplet is drawn in white when a nozzle is actuated, and in black when none of the nozzles are actuated. The length of the droplet path is about $500 \mu m$. The droplet does spread somewhat, as the highest dark fringe disappears over the course of the experiment. The height decreases. Therefore, the surface area must have increased.

pixels thick. The measured droplet radius is consistent with Tanner's law as show in figure 7.4, although the accuracy of the experiment is insufficient to distinguish between spreading according to Tanner's law, or no spreading at all. The translation distance over the course of the experiment is $500 \mu m$, while the droplet has only spread about $10 \mu m$, much less then the translation. The translation does not cause the droplet to spread.

7.3 Analysis

The droplet is very thin with respect to its horizontal extent. Thin film Marangoni flow is governed by liquid and surfactant transport, and lubrication flow. Assume that most of the surfactant is located at the surface, so the surfactant is insoluble. In other words, the layer thickness is much smaller than the ratio of surface concentration over bulk concentration. The transport equations for liquid and surfactant are

$$\begin{aligned} \partial_t \check{h} &= -\nabla \cdot (\check{h} \check{\mathbf{u}}) \\ \partial_t \check{c} &= -\nabla \cdot (2\check{c} \check{\mathbf{u}}) \end{aligned} \quad (7.2)$$

where $\check{\mathbf{u}}$ is the depth averaged velocity, \check{h} is the layer thickness, $\check{\sigma}$ is the surface tension, and \check{c} is the surface concentration of surfactant, the number of surfactant molecules per unit surface area. Dimensional variables are indicated by $\check{\cdot}$

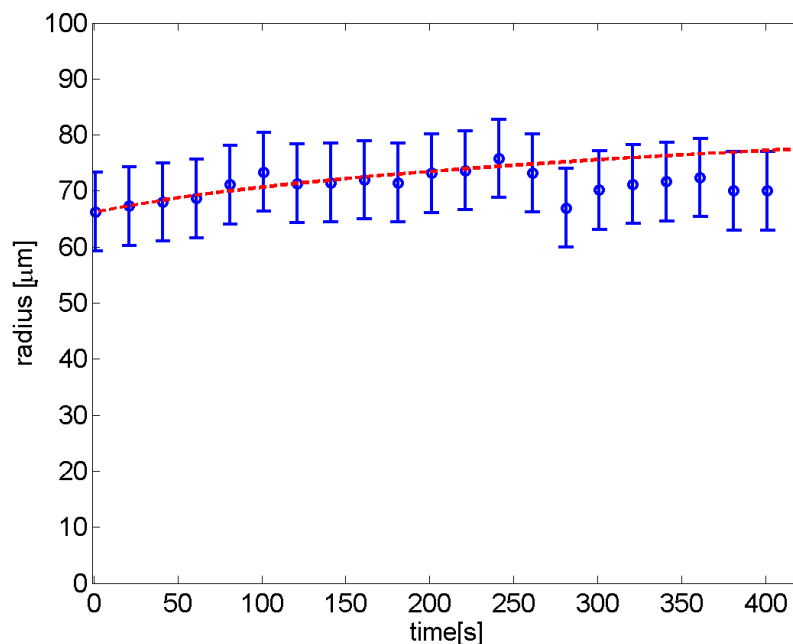


Figure 7.4: The effective radius of the droplet in figure 7.3 (circles with error bars) and the droplet radius based on Tanner's law (dashed) are plotted versus time. The droplet spreads $10 \mu m$ during the experiment.

in this paper. If the Reynolds number and the slope are both small, the flow is approximated closely by lubrication flow.

$$\check{\mathbf{u}} = \frac{1}{2\mu} \check{h} \nabla \check{\sigma} \quad (7.3)$$

The equation of state $\check{\sigma}(\check{c})$ of the surfactant, the relation between the surfactant concentration and the surface tension, is a material parameter. Although this material parameter is unknown, the order of magnitude of the derivative with respect to concentration can be estimated. The surfactant concentration is assumed large enough to significantly change the surface tension. This change in surface tension is of order $\Delta\check{\sigma} \sim -\sigma_0$ where the minus sign indicates that when surfactant is present, the surface tension is lower than in the absence of surfactant. Divide this change in surface tension by the surfactant concentration that led to this change, to obtain an estimate of the derivative of the equation of state.

$$\check{\sigma}' \sim -\frac{\sigma_0}{c_0} \quad (7.4)$$

where c_0 is a reference concentration of the same order of magnitude as the concentrations that occur in the flow, for instance the concentration averaged over the droplet at the start of the calculation or experiment. The derivative of the equation of state is negative because the surface tension decreases when surfactant is adsorbed to the surface.

The equations that govern thin layer Marangoni flow in the lubrication approximation can be nondimensionalized with

$$\sigma = \frac{\check{\sigma}}{\sigma_0} \quad (7.5)$$

$$h = \frac{\check{h}}{h_0} \quad (7.6)$$

$$\mathbf{u} = \frac{\check{\mathbf{u}}}{u_0} \quad (7.7)$$

$$t = \frac{\check{t}}{T} \quad (7.8)$$

$$\mathbf{x} = \frac{\check{\mathbf{x}}}{L} \quad (7.9)$$

$$c = \frac{\check{c}}{c_0} \quad (7.10)$$

where u_0 is the velocity of translation, $T = \frac{L}{u_0}$ is the convective time scale based on the translation velocity, L is a horizontal length scale such as the droplet diameter, $\check{\mathbf{x}}$ denotes horizontal position, and h_0 is a vertical length scale that scales with the layer thickness or the droplet height. The governing equations are nondimensionalized as defined above.

$$\partial_t h = -\nabla \cdot (h\mathbf{u}) \quad (7.11)$$

$$\partial_t c = -\nabla \cdot (2c\mathbf{u}) \quad (7.12)$$

$$\mathbf{u} = \frac{\Sigma\sigma'}{2\text{Ca}} h \nabla c \quad (7.13)$$

where $\Sigma = \frac{h_0}{L}$ is the aspect ratio of the droplet and $\text{Ca} = \frac{\mu u_0}{\sigma_0}$ is the Capillary number. Note that the derivative of the dimensionless equation of state σ' is now a negative number of order unity. We call the ratio $\text{Mg} = \frac{\Sigma\sigma'}{\text{Ca}} \approx -500$ the Marangoni number because it is a measure of the ratio of Marangoni stress and viscous friction. The Marangoni number is large in this case. This fact is used to identify which effects can be neglected, in order to simplify the analysis.

To identify negligible terms, insert equation 7.13 in equation 7.12 to obtain a nonlinear diffusion equation for the surfactant concentration.

$$\partial_t c = -\text{Mg} \nabla \cdot (ch \nabla c) \quad (7.14)$$

The chain rule was applied to the nondimensional equation of state. Note that the diffusion coefficient $\kappa = -c h \text{Mg}$ is positive definite and large. As a result, the governing set of equations is stiff. The diffusion time scale $\kappa^{-1} \approx \frac{1}{500}$ is very small with respect to the time scale of fluctuations of the boundary conditions, the convective time scale. For numerical solution of differential equations, stiffness is a problem that can sometimes be dealt with. Here, we use it to simplify the analysis, turning it into an advantage. Key to this method is to recognize that on the fast time scale $\kappa^{-1} \approx \frac{1}{500}$, the boundary conditions are essentially constant in time.

Decompose the concentration into three different components, each with a different spatial and temporal behavior.

$$c = c_0(t) + \tilde{c}(\mathbf{x}, t) + \bar{c}(\mathbf{x}, t) \quad (7.15)$$

The first is the spatial average of the slow concentration c_0 , which depends only on time. The second component is the spatial fluctuation \tilde{c} of the slow concentration. This quantity depends on both space and time, but is governed by an elliptic PDE in the spatial dimensions. The time dependence enters only through the boundary conditions. The third component is the fast concentration fluctuation \bar{c} , which decays exponentially with a time scale of κ^{-1} .

The slow concentration \hat{c} is defined as the steady state solution to equation 7.14 that satisfies the boundary conditions.

$$-\text{Mg}\nabla \cdot (\hat{c}h\nabla\hat{c}) = 0 \quad (7.16)$$

Decompose the slow concentration $\hat{c} = c_0 + \tilde{c}$ into the spatial average and the spatial fluctuation.

$$-\text{Mg}\nabla \cdot ((c_0 + \tilde{c})h\nabla\tilde{c}) = 0 \quad (7.17)$$

The average of the slow surface concentration of surfactant is defined as

$$c_0 = \frac{1}{A} \iint_{\Omega} \hat{c} da \quad (7.18)$$

where Ω is the investigated area, which is the droplet in this case. Rewrite equation 7.17 to obtain the divergence of the accompanying velocity field.

$$c_0\nabla \cdot \tilde{u} - \text{Mg}\nabla \cdot (\tilde{c}h\nabla\tilde{c}) = 0 \quad (7.19)$$

where \tilde{u} is the velocity field due to \tilde{c} , the slow velocity field fluctuation. This equation can be used to estimate the order of magnitude of the divergence of the velocity due to the slow concentration field.

The surfactant concentration is of order c_0 in the entire region of flow, not just over the droplet. If the droplet is small with respect to the distance to sources or sinks of surfactant, the spatial fluctuation of the surfactant concentration is much smaller than the average of the slow concentration.

$$\frac{\tilde{c}}{c_0} \sim \varepsilon \ll 1 \quad (7.20)$$

Since c_0 and h are order 1 quantities and $\tilde{c} \sim \varepsilon$, the divergence of the slow velocity fluctuation is of order

$$\nabla \cdot \tilde{u} \sim \text{Mg}\varepsilon^2 \quad (7.21)$$

while

$$\tilde{u} \sim \text{Mg}\varepsilon \quad (7.22)$$

which is much larger. The slow velocity field is solenoidal.

To obtain the fast concentration field, decompose equation 7.14.

$$\partial_t(c_0 + \tilde{c} + \bar{c}) = -\text{Mg}\nabla \cdot ((c_0 + \tilde{c} + \bar{c})h\nabla(c_0 + \tilde{c} + \bar{c})) \quad (7.23)$$

Neglect higher order terms in the fluctuations, retaining only first order terms. Also use the definition of the slow fluctuation and set spatial derivatives of c_0 to zero to obtain a simplified expression.

$$\partial_t(c_0 + \tilde{c} + \bar{c}) = -\text{Mg}\nabla \cdot (c_0h\nabla(\bar{c})) \quad (7.24)$$

Since $c_0 \gg \tilde{c}$, the time derivative of the slow fluctuation can be neglected.

$$\partial_t(c_0 + \tilde{c}) = -Mg\nabla \cdot (c_0 h \nabla(\tilde{c})) \quad (7.25)$$

The average concentration fluctuates on a time scale equal to the convective time scale. The time scale of the fast fluctuation κ^{-1} , the diffusive time scale, is much smaller. Since the slow concentration field satisfies the boundary conditions by definition, the fast fluctuation is subject to homogenous boundary conditions. On a small time scale of κ^{-1} , the fast fluctuation decays to the steady state solution of equation 7.25, treating $\partial_t c_0$ as a constant.

$$\frac{1}{2c_0} \partial_t c_0 = \nabla \cdot \bar{u} \quad (7.26)$$

In a steady ambient concentration field, the time derivative of c_0 is the result of the droplet traversing the concentration field. The gradient of this concentration field is of order ε , and so is the time derivative of c_0 since the traversal time is used as the time scale. The divergence of \bar{u} is of order ε , while the total velocity field is of order $Mg\varepsilon$ which is much larger. The other component of the divergence is of order $Mg\varepsilon^2$, which is also much smaller than the total velocity field. The divergence of the velocity field is small. In other words, the flow is solenoidal.

$$\nabla \cdot \mathbf{u} \approx 0 \quad (7.27)$$

This result is subject to the following conditions.

- constant ambient surfactant concentration
- the aspect ratio is much larger than the capillary number
- the relative variation of the surfactant concentration is small

This is a result of the magnitude of the decrease of the surface tension with increasing surfactant concentration. If there is a region on the surface with a net outflow of liquid, so that there is divergence in that region, there is also a net outflow of surfactant. This decreases the surfactant concentration, and thus increases the surface tension in that region. This higher surface tension causes Marangoni flow towards the region, reducing the divergence. If the given conditions are met, this negative feedback effect is so large that it prevents any significant divergence.

When $\nabla h \times \nabla c = 0$, the flow is not only solenoidal, but also two-dimensionally irrotational, i.e., the rotation of the depth averaged velocity field vanishes. This condition is met in the case of constant layer thickness. To derive this, take the curl of the velocity.

$$\nabla \times \mathbf{u} = 2Mg\nabla \times h\nabla\sigma = 2Mg(\nabla h) \times (\nabla\sigma) \quad (7.28)$$

If the rotation vanishes too, then the concentration field is governed by Laplace's equation

$$\nabla^2 c = 0 \quad (7.29)$$

so that the methods for calculating potential flow can be applied to analyze Marangoni flow of a uniform thin layer.

By Gauss's divergence theorem, a solenoidal flow field preserves the area of a droplet. The boundary of the droplet moves with the depth averaged velocity field. Integrate the divergence over the droplet and apply Gauss' divergence theorem to obtain the rate of change of the surface area of the droplet.

$$\frac{dA}{dt} = \oint_{\partial\Omega} u_n ds = \iint_{\Omega} \nabla \cdot \mathbf{u} da \quad (7.30)$$

Since the divergence vanishes everywhere, so does its integral. Marangoni flow does not change the surface area of a droplet that it translates unless one of the conditions for a solenoidal velocity field is violated. Thus, droplets are not spread due to translation by Marangoni flow.

7.4 Validation and demonstration of the solenoidal theory

If a Marangoni flow is solenoidal, this greatly simplifies analysis [9] of such flows. This is now demonstrated. A ridge along the x_2 direction that is transported by Marangoni flow in the x_1 direction is analyzed. First, we show that the vanishing divergence of the depth-averaged velocity field allows a complete analytical treatment of a small ridge. Second, the fingering instability at the leading edge of a large ridge is analyzed. The calculated results are then compared with experimental data, providing an extra test of the developed theory.

Consider a ridge that has a cross sectional profile that is constant in the x_2 direction. This ridge is transported by Marangoni flow in the x_1 direction. The Marangoni stress is caused by a concentration gradient of an insoluble surfactant. The horizontal extent of the ridge is small with respect to both $\frac{h_0}{Ca}$ and $\frac{C}{\partial_n C}$, so that this flow satisfies the conditions for solenoidal Marangoni flow. The two-dimensional divergence of the depth averaged velocity vanishes. By symmetry, the depth averaged velocity in the x_2 direction u_2 vanishes also.

$$0 = \nabla \cdot \mathbf{u} = \partial_2 u_2 + \partial_1 u_1 = \partial_1 u_1 \quad (7.31)$$

Integrate to obtain the velocity field in the x_1 direction. The depth averaged velocity far away from the ridge is used as the velocity scale.

$$u_1 = 1 \quad (7.32)$$

In a small ridge, the depth averaged velocity is constant everywhere.

In a reference frame that moves with the ridge, the depth averaged velocity of the ink vanishes. In this reference frame, the substrate at a vertical position of $y = 0$ moves in the $-x_1$ direction with a velocity $v_1(x_1, x_2, 0) = -1$, where $\mathbf{v}(x_1, x_2, y)$ is the 3-dimensional velocity field. The horizontal velocity at the liquid-air interface at $y = h(x_1)$ is $v_1(x_1, x_2, h(x_1)) = 1$, and by continuity of shear stress, assuming small slopes, the horizontal velocity in between is

$$v_1(x_1, y) = 2\frac{y}{h(x_1)} - 1 \quad (7.33)$$

Since the velocity is a derivative of the stream function, the stream function is determined by the velocity field up to an arbitrary additive constant. The

7.4. VALIDATION AND DEMONSTRATION OF THE SOLENOIDAL THEORY 121

stream function can be arbitrarily set to zero at the substrate. Integrate in the vertical direction to obtain the stream function in the entire flow domain.

$$\psi(x_1, y) = \frac{y^2}{h(x_1)} - y \quad (7.34)$$

Contours of the stream function are streamlines. They are plotted in figure 7.5 for a height profile of $h(x_1) = \varepsilon + (1 + x_1^2)^{-1}$ where ε is the small layer thickness at infinity, far away from the ridge. Many streamlines are closed.

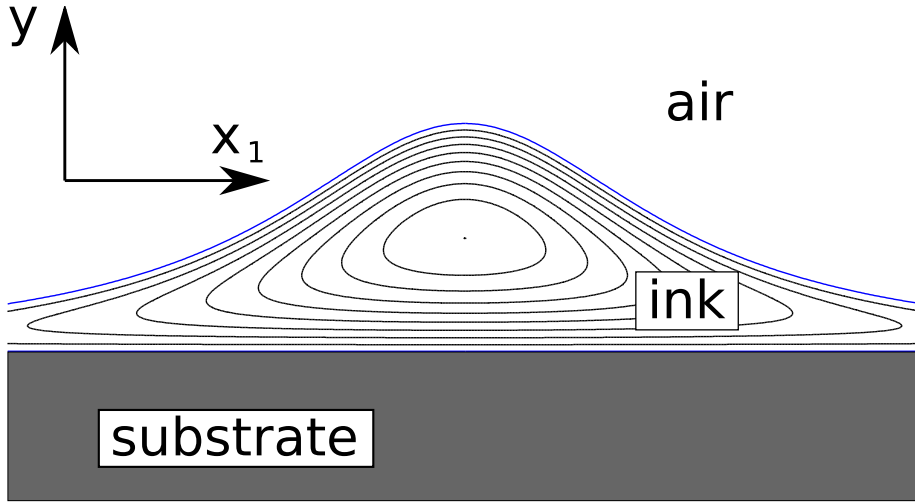


Figure 7.5: A cross-sectional area of a narrow ridge with streamlines. Most, but not all streamlines are closed. The thicknesses of the layers above and below the recirculation zone are a quarter of the layer thickness far away from the ridge. They are too small to plot individually.

A small ridge contains a recirculation zone, showing that not just the shape, but also the liquid itself is transported. The boundary of this recirculation zone is a streamline. The value of the streamfunction ψ_r at this streamline is the minimum of the streamfunction at infinity.

$$\frac{d\psi}{dy} = 2\frac{y}{h(x_1)} - 1 \quad (7.35)$$

Find the minimum.

$$\frac{d\psi}{dy} = 0 \Rightarrow \frac{y_r}{h(x_1)} - \frac{1}{2} = 0 \Rightarrow y_r = \frac{\varepsilon}{2} \quad (7.36)$$

Find the value at the minimum.

$$\psi_r = -\frac{\varepsilon}{4} \quad (7.37)$$

At the thickest point of the ridge, the layer of ink above and below the recirculation zone has a thickness of $\frac{1}{4}\varepsilon$. This is very thin indeed. Most of the ridge consists of recirculation zone.

A large wide ridge might not satisfy $Mg \gg 1$, but small parts such as the leading and trailing edges, do. The analysis of a large ridge that is presented in this paper focusses on the leading and trailing edges.

A leading edge is known to exhibit a fingering instability. In the partial wetting regime, the stability of a contact line that recedes over a vertical plate has been treated extensively [10]. For Marangoni flow in the complete wetting regime, stability of the shape of a leading or trailing edge is less thoroughly understood. The fingering instability was calculated numerically by [11] for Marangoni flow of insoluble surfactant, by [12] for Marangoni flow of soluble surfactant, and by [13] for Marangoni flow of soluble surfactant at concentrations above the critical micelle concentration using direct numerical simulations. In the case of insoluble surfactant, they concluded that the wavenumber of the fastest growing disturbance is selected by competition between Marangoni stress, surface diffusion and Laplace pressure. Marangoni stress favors small wavelength disturbances while Laplace pressure and surface diffusion provide a small wavelength cutoff. They showed that the disparity in thickness between the surfactant rich layer and the liquid film over which it spreads is essential.

Since the ambient layer thickness is constant, the flow in the ambient layer can be calculated with potential theory. The gradient of the layer thickness vanishes, so the cross product of the layer thickness gradient and the surfactant concentration gradient vanishes too. According to equation 7.28, this implies that the depth averaged velocity field is two-dimensionally irrotational. An irrotational vector field can be written as the gradient of a scalar potential. In thin film Marangoni flow the potential is $\frac{1}{2}Mg\delta\gamma$, where γ is the only variable. When this vector field is also solenoidal, the field equation for this potential is Laplace's equation.

At the edges of the ridge, the layer thickness becomes much larger than the ambient layer thickness over a small distance. Where the layer thickness is much larger than the ambient layer thickness, the surfactant concentration equilibrates at a much higher rate than in the ambient layer. The variation in surfactant concentration is small with respect to the variation in the ambient layer. In the calculation of the flow in the ambient layer, the surfactant concentration in the ridge can be held constant. This imposes a Dirichlet boundary condition on the surfactant concentration in the ambient layer at the edge of the ridge.

The fingering instability is an instability in the velocity of the edge of the ridge. The velocity of this edge is proportional to the gradient of the surfactant concentration, so the objective is to obtain the normal derivative of the surfactant concentration by solving the field equation, Laplace's equation, subject to a Dirichlet boundary condition at the edge. This instability is analogous to the Saffman-Taylor instability, since the same governing equation is solved, subject to the same boundary conditions.

The initial condition is a straight front at $x_1 = x_f$ that is perturbed slightly, as shown in figure 7.6. The amplitude $x_a \ll k^{-1}$ of this disturbance is small with respect to the wavelength. The governing equations are nondimensionalized with the film thickness h_l as length scale, the undisturbed velocity u_0 as velocity scale, and the surface tension at the ridge as force scale.

$$x_f|_{t=0} = x_a \sin(kx_2) \quad (7.38)$$

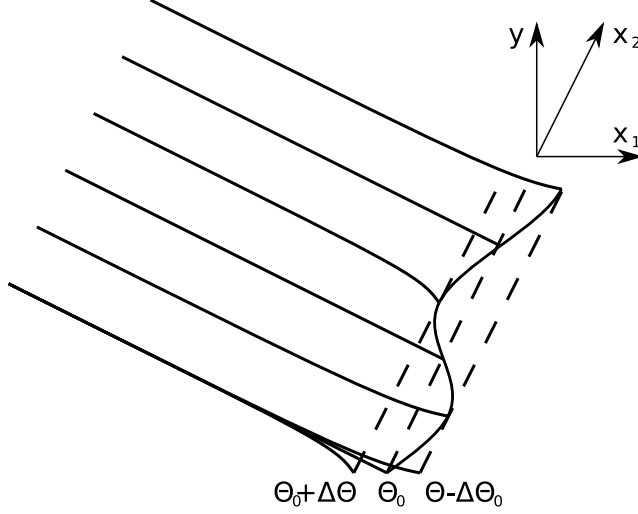


Figure 7.6: The edge of the ridge is shown, meandering along the x_2 direction due to the disturbance of the edge position. The ridge is located on the $-x_1$ side of the edge. The vertical scale is exaggerated for clarity. Since the flow in the ridge is much faster than the flow in the thin layer, the pressure in the ridge is constant. Therefore, the curvature of the free surface must vanish in the ridge. As a result, the slope $\Theta_0 - \Delta\Theta$ at the tips of the fingers is smaller than the slope $\Theta_0 + \Delta\Theta$ between the fingers.

During the evolution of the system, the front is located at

$$x_f(x_2, t) = x_a(t) \sin(kx_2) + t \quad (7.39)$$

At this front, the fluctuation of the surface tension $\tilde{\sigma}$ is set to zero arbitrarily, so the surface tension at the ridge is chosen as the reference concentration.

$$\tilde{\sigma}(x_f, x_2) = 0 \quad (7.40)$$

For small values of the amplitude x_a , a boundary condition at $x_1 = t$ can be derived. Take the Taylor series expansion of the surface tension in the distance to the edge.

$$\tilde{\sigma}(x_f, x_2) = \tilde{\sigma}(0, x_2) + x_a \sin(kx_2) \partial_1 \tilde{\sigma}|_{x_1=0} + O(x_a^2) = 0 \quad (7.41)$$

The undisturbed surface tension, where the disturbance amplitude is set to zero, gives rise to a uniform velocity field.

$$\tilde{\sigma}|_{x_a=0} = -\frac{2Ca}{h}(x_1 - t) \quad (7.42)$$

The disturbance of the surface tension σ_a due to the instability is defined by

$$\tilde{\sigma} = -\frac{2\text{Ca}}{h}(x_1 - t) + \sigma_a \quad (7.43)$$

Since this disturbance vanishes for zero disturbance amplitude, it is at least of first order in x_a , while the gradient of the undisturbed surface tension is of zeroth order. The surface tension gradient is dominated by the gradient of the undisturbed surface tension for small disturbance amplitudes. Insert in equation 7.41 to obtain a boundary condition at $x_1 = t$ on the disturbance of the surface tension.

$$\sigma_a(x_1, x_2, t)|_{x_1=u_0t} = x_a \sin(kx_2) \frac{2\text{Ca}}{h} + O(x_a^2) \quad (7.44)$$

In cartesian coordinates, Laplace's equation is separable.

$$\sigma_a = X_1(x_1 - t) X_2(x_2) \quad (7.45)$$

Retain only first order terms in x_a , neglecting higher order terms, and solve Laplace's equation.

$$X_1(x_1) = -x_a \frac{2\text{Ca}}{h} e^{kx_1} \quad (7.46)$$

$$X_2(x_2) = \sin(kx_2) \quad (7.47)$$

The spatial frequency k must be negative to satisfy the boundary condition at $x_1 \uparrow \infty$. The velocity of the front is related to the spatial derivative of the surface tension through

$$\mathbf{u} = \frac{1}{2\text{Ca}} h \nabla \sigma \quad (7.48)$$

Insert the derivative of the obtained surface tension field with respect to x_1 to obtain an ODE for the growth of the disturbance.

$$\frac{d}{dt} x_a = -x_a k \quad (7.49)$$

The solution of this ODE is

$$x_a(t) = x_a(0) e^{-kt} \quad (7.50)$$

Equation 7.50 describes the small amplitude behavior of a disturbance of spatial frequency k in the front position, where k is negative.

The leading edge of a ridge is unstable to perturbations of the front position, while the trailing edge is stable, as depicted in figure 7.7. To derive this result from the obtained expression for the evolution of the disturbance amplitude, equation 7.50, recall that k is negative. The exponent is positive. Time is nondimensionalized with

$$T = \frac{h_0}{u_0} \quad (7.51)$$

which is positive for positive u_0 . This corresponds to a thick layer that overflows a thinner layer with increasing dimensional time, so the boundary between the two regions is the leading edge of a ridge. At the trailing edge, u_0 is negative, so disturbances decay with increasing dimensional time. The trailing edge will become ever smoother, while at the leading edge, a fingering instability develops.

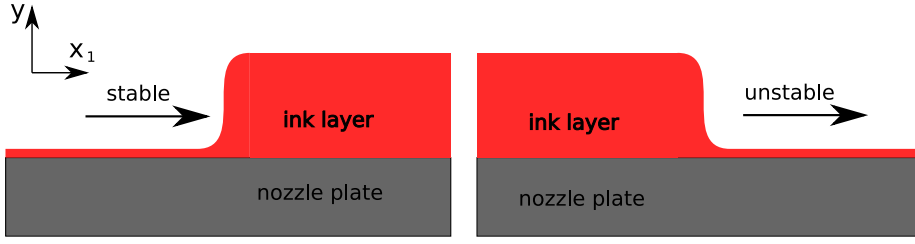


Figure 7.7: The leading edge, where the velocity of the front is towards the thinner ink layer, is unstable with respect to the fingering instability. A trailing edge is stable.

By including Laplace pressure in the analysis, the order of magnitude of the spatial frequency of the most unstable perturbation can be estimated, assuming negligible surface diffusion. A small distance after the edge of the ridge, the slope in the x_1 direction is nearly constant. This slope is recovered over a distance of Δx , as shown in figure 7.8. When the slope is recovered, it is nearly constant on a length scale of Δx . The Laplace pressure results from the curvature in the x_1 direction.

$$\check{P}_l \sim \frac{\sigma_0 \theta}{\Delta \check{x}} \quad (7.52)$$

Over the region where the curvature goes to zero, the Laplace pressure decreases to zero. This Laplace pressure gradient leads to a parabolic flow profile. The viscous stress at the top is balanced by Marangoni stress as illustrated in figure 7.9. Half of the force due to Laplace pressure is absorbed by the substrate, and the other half is absorbed by Marangoni stress. The difference in surface tension between the location of maximum curvature and the thin layer, is half the Laplace pressure integrated over the layer thickness.

$$\check{\sigma}_l \sim \check{\sigma}_c - \frac{\sigma_0 \theta \check{h}_l}{\Delta \check{x}} \quad (7.53)$$

where $\check{\sigma}_l$ is the surface tension in the thin layer, close to the edge of the ridge, and $\check{\sigma}_c$ is the surface tension in the cusp, where the curvature is greatest. \check{h}_l is the layer thickness in the thin layer. The same argument yields an expression for the surface tension difference on the other side.

$$\check{\sigma}_r \sim \check{\sigma}_c - \frac{\sigma_0 \theta \check{h}_r}{\Delta \check{x}} \quad (7.54)$$

where $\check{\sigma}_r$ is the surface tension in the ridge near the edge, and \check{h}_r is the layer thickness in the ridge, where the slope is recovered.

$$\check{h}_r \sim \check{h}_l + \frac{1}{2} \Delta \check{x} \theta \quad (7.55)$$

Combining equations 7.53, 7.54, and 7.55, an expression is obtained for the difference in surface tension over the edge of the ridge.

$$\check{\sigma}_l - \check{\sigma}_r \sim \frac{1}{2} \sigma_0 \theta^2 \quad (7.56)$$

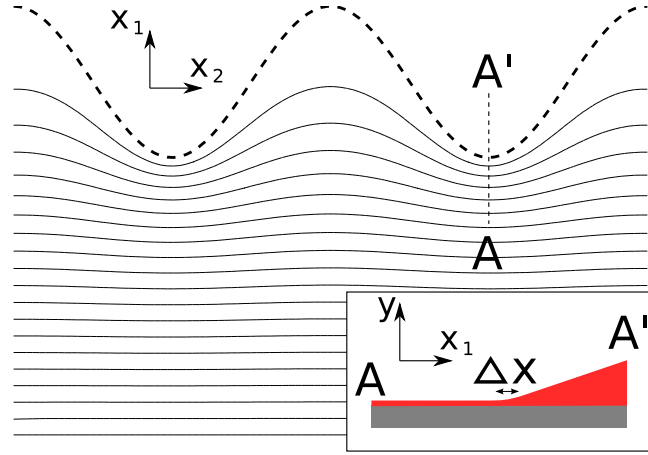


Figure 7.8: The front (thick dashed line) and concentration contours. The contours are close together at the tips of the fingers, indicating a large concentration gradient, while they are further apart in between the fingers, indicating a small concentration gradient. In the inset, a cut along the line from A to A' is sketched. The thin layer is flat, with the free surface parallel to the substrate. In the thick region, the slope is nearly constant. The slope is recovered over a region of length Δx . The height is exaggerated for clarity.

This equation is nondimensionalized, taking the surface tension in the ridge as σ_0 , the reference surface tension.

$$\sigma_l - \sigma_r \sim \frac{1}{2}\theta^2 \quad (7.57)$$

The change in surface tension is independent of the distance over which the slope is recovered. This is convenient because this distance is hard to measure or calculate. To obtain the slope, consider Laplace pressure in the ridge. Laplace pressure variation over the ridge is small, because the thickness of the ridge is much larger than the thin layer. This causes fluctuations to equilibrate much faster in the ridge than in the thin layer. The curvature of the surface must therefore vanish. In limit of a layer thickness that is small with respect to the horizontal length scales, the curvature can be approximated by the two-dimensional Laplacian of the layer thickness. The layer thickness in the ridge satisfies Laplace's equation. The boundary condition at negative infinity on the layer thickness is a constant slope. The boundary condition at the edge of the ridge is a constant layer thickness. The solution to this boundary value problem was already obtained in the calculation of the surface tension in the thin layer.

$$h(x_1, x_2) = 1 + x_a \theta_0 e^{k(t-x_1)} \sin(kx_2) + \theta_0(t-x_1) \quad (7.58)$$

The fluctuation of the slope is the derivative in the x_1 direction. The fluctuation of the slope at the edge of the ridge $\tilde{\theta}(x_2)$ determines the influence of Laplace pressure on the boundary condition on the surface tension.

$$\tilde{\theta}(x_2) = x_a \theta_0 k \sin(kx_2) \quad (7.59)$$

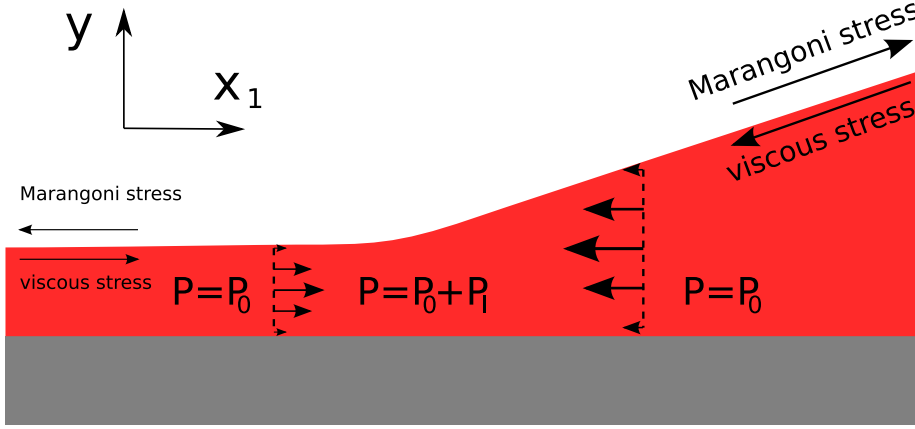


Figure 7.9: In the cusp, the Laplace pressure is lowest. Where the slope is constant, Laplace pressure vanishes. In between, there is a pressure gradient. Since Marangoni stress resists surface compression, the air-ink interface is nearly stationary. In the bulk, the pressure gradient is balanced by viscous stress. At the interface, viscous stress is balanced by Marangoni stress. The pressure gradient results in a larger Marangoni stress where the layer thickness is larger. This difference in Marangoni stress magnitude between the two sides of the cusp results in a net Marangoni stress acting on the cusp, and thus a difference in surface tension between the ridge and the ink layer.

The obtained slope is inserted into equation 7.57 to obtain the surface tension boundary condition at the edge of the ridge. The surface tension in the ridge $\sigma_r = 1$ is constant.

$$\sigma_l \sim \frac{1}{2}(\theta_0 + x_a \theta_0 k \sin(kx_2))^2 + 1 \quad (7.60)$$

This equation can be linearized in x_a .

$$\sigma_l \sim \frac{1}{2}\theta_0^2 + x_a \theta_0^2 k \sin(kx_2) + 1 \quad (7.61)$$

The Laplace equation for the surface tension in the thin layer is solved, subject to this boundary condition and the boundary condition at infinity, as before. From this solution, the Marangoni stress in the x_1 direction due to Laplace pressure can be determined. Only the part that leads to growth or decay of the disturbance in the position of the edge is retained.

$$\partial_1 \tilde{\sigma} \sim x_a \theta_0^2 k^2 \sin(kx_2) \quad (7.62)$$

Inserting this equation into the governing equation for the velocity yields the edge velocity $u_{1,L}$ due to Laplace pressure.

$$u_{1,L} \sim \frac{1}{2Ca} h_l x_a \theta_0^2 k^2 \sin(kx_2) \quad (7.63)$$

To complete the analysis, add the contribution of Laplace pressure to the

front velocity due to Marangoni stress alone.

$$\frac{d}{dt}x_a \sim -x_a \left(k + \frac{k^2 \theta_0^2 h_l}{2Ca} \right) \quad (7.64)$$

The maximum growth rate occurs at a spatial frequency of

$$k_{\max} \sim -\frac{Ca}{\theta_0 h_l} = \frac{\mu u_0}{\theta_0 h_0 \sigma_0} \quad (7.65)$$

Note that $h_l = 1$ since the thickness of the thin layer was taken as the length scale. High spatial frequencies decay.

$$k \gg -\frac{2Ca}{\theta_0 h_l} \Rightarrow \frac{d}{dt}x_a < 0 \quad (7.66)$$

According to equation 7.65, the maximum growth rate of the perturbation occurs at intermediate spatial frequencies.

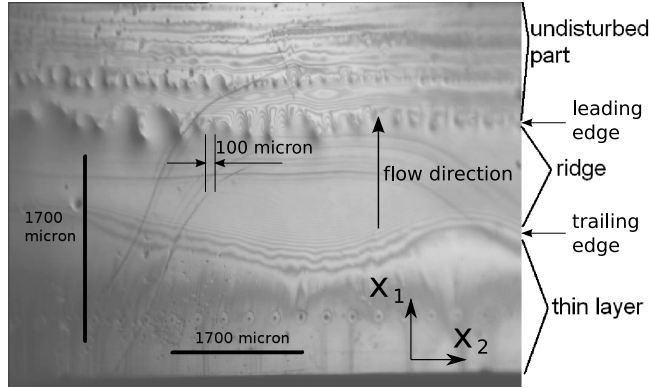


Figure 7.10: A view of the nozzle plate, 1 second after wiping with a clean cloth. Near the lower edge of the image, the nozzles are visible as small dark dots. The nozzles are in a fairly smooth, very thin (less than a quarter wavelength, about 125 nm) layer of ink. Above this thin layer is a ridge, a thicker band of ink. This ridge moves towards the center of the nozzle plate, upwards in this image, with a velocity of 10^{-3} ms^{-1} . At the top of the image is a region with a thin liquid layer that is not yet disturbed by the incoming ridge. Note that the fingering instability only develops at the leading edge of the ridge. The trailing edge is smooth. Both observations are predicted by the presented solenoidal Marangoni flow theory. The wavelength of the fingering instability is between $\lambda = 100 \mu\text{m}$ and $\lambda = 300 \mu\text{m}$, in accordance with the developed theory.

Experimentally, a large ridge was created by wiping the nozzle plate with a cloth. Since the nozzle plate is completely wetted by the ink, a thin layer is left behind. The surface tension is lower at the sides of the nozzle plate. As a result, the nozzle plate dries, not unlike the process of Marangoni drying as used in the semiconductor industry [14]. The phenomenon is shown in figure 7.10, about one second after wiping. At the bottom of the image, a flat region exists where the layer thickness is very small. This is where the nozzles are located.

The horizontal length scale is much larger than the radius of the droplet treated earlier. The assumption that $Mg \gg 1$ is invalid in this case, although it is valid over a much smaller region, such as the leading or trailing edge. Accordingly, the flow is not solenoidal and a ridge forms. In front of this ridge, the liquid is quiescent.

The trailing edge of the ridge is very smooth, while a fingering instability develops at the leading edge. The length scale is given by the circles around the nozzles. The diameter of these circles is $130 \mu m$. The viewing angle is 45° , so the length scale in the direction tangential to the flow, is $\sqrt{2}$ times the length scale in the transverse direction. The distance between the fingers is between $\lambda = 100 \mu m$ and $\lambda = 300 \mu m$.

In this case, The values of the various parameters are

$$\begin{aligned}\mu &= 10^{-2} Nm^{-2} \\ u_0 &= 10^{-3} ms^{-1} \\ \sigma_0 &= 25 \cdot 10^{-3} Nm^{-1} \\ \theta &= 25 \cdot 10^{-3} \\ h_0 &= 10^{-6} m\end{aligned}$$

Using equation 7.65, the order of magnitude of the distance between fingers of $\lambda \sim 400 \mu m$ is predicted, while a value between $\lambda = 100 \mu m$ and $\lambda = 300 \mu m$ was observed in the experiment, which is the same order of magnitude. The experimental and theoretical results agree. This confirms the solenoidal theory.

7.5 Conclusion and discussion

Thin film Marangoni flow is solenoidal, so droplet spreading and translation are completely decoupled. This can be derived from the governing equations. The assumptions are that the surfactant is insoluble, that surface diffusion is negligible, that fluctuations of the surfactant concentration are small with respect to the absolute concentration, and that the capillary number is small with respect to the aspect ratio of the system. This hypothesis was suggested by an experimental observation and tested in a different experiment. In the latter experiment, the solenoidal theory was confirmed.

If the layer thickness is constant or the surfactant concentration gradient is parallel to the gradient of the layer thickness, the two coupled transport equations reduce to Laplace's equation on the surfactant concentration.

As a demonstration of how the developed theory simplifies analysis, the evolution of the fingering instability at the leading edge of a translating ridge was treated. The mechanism of the fingering instability is revealed by the analysis. The fingers shield the rest of the front from the variation in surfactant concentration, in the same way that Faraday's cage shields the interior from electric fields. The instability is also similar to a Saffman-Taylor instability in porous media. This increases the surface tension gradient at the tips of the fingers, while the surface tension gradient is decreased between the fingers. The small wavelength cutoff is provided by Laplace pressure, as shown by Craster and Matar [13]. The prediction that the disparity of the layer thickness before and after the front is essential, is confirmed, and the cause of this necessity

is revealed. The disparity between the layer thicknesses is what provides the shielding capacity of the fingers.

For thin film Marangoni flow in general, the stiff transport equation for surfactant is reduced to an elliptic equation in two spatial dimensions. The time scale of equilibration of the surfactant concentration is much smaller than the convective time scale. This separation of time scales is called stiffness, and poses a problem for numerical analysis. The time step must be smaller than the smallest time scale for most integration methods. The large separation of time scales implies that the number of time steps must be large. This problem can sometimes be mitigated by using implicit integration schemes. This is the solution chosen by Warner, Craster, and Matar [11] [12] [13]. Implicit methods are computationally costly and can be difficult to implement. In some cases, such as the one treated, the stiffness can be turned into an advantage by considering the limiting case where the smallest time scale vanishes. The corresponding evolution equation is now replaced by a PDE of lower dimension where derivatives with respect to time are eliminated. This approach is often taken in the analysis of bulk flows, where the time scale of acoustic disturbances is very small with respect to the convective and diffusive time scales. Because numerical integration of the general case would be limited by Courant's condition on the velocity of sound $c \Delta t < \Delta x$, the limit of incompressible flow is usually considered. In incompressible flow, the liquid velocity is usually the largest velocity. For low Mach number flows, this velocity is much smaller than the velocity of sound so that the upper limit on the time step is much less stringent. In the incompressible approximation of bulk flows, the velocity is solenoidal. This simplifies the governing equations to such an extent that vorticity free solenoidal flows have been tractable for centuries. This led to the development of a plethora of potential flow methods that can now, with the theory that is presented in this paper, be applied to thin film Marangoni flow as well.

Bibliography

- [1] A. Guyton, Textbook of medical physiology (eighth edition), W.B. Saunders company (1991).
- [2] A. Darhuber, S. Troian, Principles of microfluidic actuation by modulation of surface stresses, *Annu. Rev. Fluid Mech.*, **37**, 425-455 (2005).
- [3] B. Beulen, J. de Jong, H. Reinten, M. van den Berg, H. Wijshoff, M. van Dongen *Flows on the nozzle plate of an inkjet printhead*, *Exp. Fluids* **42**, 217-224 (2007).
- [4] A. Oron, S. Davis, S. Bankoff *Long-scale evolution of thin liquid films*, *Rev. Mod. Phys.* **69**, 931-980 (1997).
- [5] O. Jensen, S. Naire *The Spreading and stability of a surfactant-laden drop on a pretreated substrate*, *J. Fluid Mech.*, **554** 5-24 (2006).
- [6] M. Clay, M. Miksis *Effects of surfactant on droplet spreading*, *Phys. Fluids Mech.*, **16** 3070-2078 (2004).
- [7] P. de Gennes, F. Brochard-Wyart, D. Quéré *Capillarity and wetting phenomena*, Springer (2004).
- [8] J. de Jong, H. Reinten, H. Wijshoff, M. van den Berg, K. Delescen, M. van Dongen, M. Versluis, D. Lohse *Marangoni flow on an inkjet nozzle plate*, *Appl. Phys. Lett.* **91**, 204102 (2007).
- [9] L. Landau, E. Lifshitz *Course of Theoretical Physics*, **6** , Butterworth-Heinemann, second edition (1987).
- [10] J.H. Snoeijer, B. Andreotti, G. Delon, M. Fermigier, *Relaxation of a dewetting contact line. Part1. A full-scale hydrodynamic calculation*, *J. Fluid Mech.*, **579**, 63-83 (2006).
- [11] M. Warner, R. Craster, O. Matar, *Fingering phenomena associated with insoluble surfactant spreading on thin liquid films*, *J. Fluid Mech.*, **510**, 169-200 (2004).
- [12] M. Warner, R. Craster, O. Matar, *Fingering phenomena created by a soluble surfactant deposition on a thin liquid film*, *Phys. Fluids*, **16**, 2933-2951 (2004).
- [13] R. Craster, O. Matar, *Fingering phenomena associated with insoluble surfactant spreading on thin liquid films*, *Phys. Fluids*, **18**, 02103 (2006).

- [14] R. Craster, O. Matar, *Models for Marangoni drying*, Phys. Fluids, **13**, 1869-1883 (2001).

Chapter 8

Conclusions

The dominant effects in nozzle failure are the compressibility of the air bubble, the inertia of the ink in the nozzle, and the viscous friction in the nozzle. In essence, the nozzle is a low-pass filter from velocity in the channel to velocity in the nozzle. As the bubble grows the cutoff frequency decreases. When the cutoff frequency of the nozzle becomes much smaller than the dominant part of the spectrum of the channel velocity, the droplet formation ceases.

The bubble influences the channel acoustics and the velocity of the ink in the nozzle through its volume oscillations. The influence of the bubble on the pressure cannot be neglected. To calculate the volume oscillations of a bubble in an inkjet printhead, the full two-way coupling between bubble volume oscillations and the channel acoustics has to be taken into account. This shows that for the bubble and channel sizes that were investigated, the two-way coupling between channel acoustics and bubble volume oscillations is much more important than an accurate modeling of the direct wall interaction. For the bubble volume oscillations, the relevant effects are identified.

- The inertia and viscous friction in the nozzle flow.
- The inertia, viscous friction, gas pressure, and surface tension effects of the radial flow field from the bubble. These effects constitute the Rayleigh-Plesset equation.
- The channel acoustics that are bidirectionally coupled to the nozzle flow and the bubble volume oscillations.

The list of relevant effects that was given above is exhaustive for the investigated parameter range.

By deriving and interpreting a complete set of dimensionless groups for a bubble in a pipe, we have developed a method to ascertain which effects are relevant and which effects can be neglected. The volume oscillations of a bubble in a pipe are now understood.

The translation map of small bubbles contains a limit cycle in the nozzle, some saddle points, and an attractor in the corner. During the part of the cycle where the bubble approaches the meniscus, the bubble might be ejected if its location at the start of the cycle is favorable. As the bubble radius increases, the limit cycle disappears and the basin of attraction of the attractor in the

corner expands to almost the entire nozzle and channel. This takes about 100 actuation cycles. After this has happened, the bubble can no longer be ejected and it will end up in the corner, where it is kept firmly in place by secondary Bjerknes force. Besides lubrication force and secondary Bjerknes force, no other forces are present since both the velocity and the pressure gradient vanish in the corner. In the corner, the bubble can grow due to rectified diffusion until the bubble volume is a few hundred picoliter, which takes about one second for the investigated printhead. The volume of the acoustic field then limits the growth of the bubble.

Air entrainment is caused by dust particles. These dust particles are transported from wherever they struck the nozzle plate to the nozzle by ink flows on the nozzle plate, as shown in previous research. In chapter 7, we have shown experimentally that the two-dimensional divergence of the depth averaged velocity of these flows vanishes. We also derived this analytically, including the conditions under which this relation holds. A flow in a thin layer of liquid that is driven by Marangoni stress due to concentration gradients of an insoluble surfactant is two-dimensionally solenoidal if the concentration fluctuation in space and time is much smaller than the absolute magnitude of the concentration. With this result, the flow was shown to obey two-dimensional potential flow if the initial layer thickness is also constant in space. As a demonstration of how this result simplifies the analysis of thin film Marangoni flow and to validate the result, a fingering instability that has been observed on the nozzle plate was calculated analytically. The predictions by this analysis were confirmed. This supports the developed theory and it suggests that the conditions for vanishing divergence are satisfied. The flow is driven by Marangoni stress due to an insoluble surfactant.

One might object to these conclusions that the influence of surfactants on the bubble evolution has been neglected, even though the flow of the same ink on the nozzle plate is driven and governed by Marangoni stress, showing that surfactants are important there. Surfactants can influence both the translation through its effect on the drag, and the volume oscillations through its effect on the Laplace pressure. The two limiting cases are a completely free surface where Marangoni stress is negligible and a completely rigid surface where Marangoni stress is dominant. The drag on a rigid sphere is larger, but still of the same order of magnitude. The influence of surfactants might change the translation quantitatively, but it is not expected to change the behavior qualitatively, so the conclusions that were drawn are expected to hold true nevertheless. The influence of surfactants on volume oscillations is expected to be small, since Laplace pressure is much smaller than the pressure fluctuation in the investigated parameter ranges. Another possible objection to these conclusions is that the bubble is assumed to remain spherical, while in other investigations, the bubble was observed to be nonspherical for similar pressure amplitudes, when it undergoes a violent collapse near a wall. In the investigated printheads, violent collapses are present in a narrow range of bubble radii. Outside of this range, the results are not affected by this phenomenon. The influence of these shape changes during a violent collapse near a wall need not be studied in a capillary tube. This is an open problem in the broader field of research of forces on bubbles. When more knowledge about this problem becomes available, the results for the translation of bubbles that undergo a violent collapse near the walls should be reconsidered.

In this research, entrained air bubbles in inkjet printheads were investigated, both the events that lead to air bubble entrainment and the evolution of an air bubble after entrainment. The causes of air entrainment were studied in depth in previous work. In this research, the driving force of the flow on the nozzle plate was identified and the effects that govern this flow were identified and quantified. This leaves the mechanism of air entrainment as the most prominent open problem of the events up to air entrainment. The evolution of the bubble after entrainment was studied experimentally in previous investigations. In those studies, the evolution was characterized as far as possible with the theory that was available at that time, most of which which was only valid for a bubble in an infinite volume of liquid. The available extensions to bubbles in confined space were for bubbles close to an infinite flat wall and for the natural frequency of oscillation of a bubble in a pipe that is short enough to neglect acoustics. Neither of the previously investigated cases is a suitable model of a bubble in an inkjet printhead. The theory on a bubble in a pipe was extended as far as necessary to predict the nonlinear volume oscillations and translational motion of the bubble.

Summary

We have investigated mechanisms that lead to nozzle failure through the influence of an entrained air bubble. We investigated how (chapters 2, 3, and 4) and under which circumstances a bubble causes nozzle failure (chapter 5), and the conditions that give rise to these circumstances (chapters 6 and 7).

In chapter 2, we identified the dominant effects in nozzle failure. The dominant effects are the compressibility of the air bubble, the inertia of the ink in the nozzle, and the viscous friction in the nozzle. In essence, the nozzle is a second order low-pass filter from velocity in the channel to velocity in the nozzle. As the bubble grows, the cutoff frequency decreases. When the cutoff frequency of the nozzle becomes much smaller than the dominant part of the spectrum of the channel velocity, the droplet formation ceases.

The bubble influences the channel acoustics and the velocity of the ink in the nozzle through its volume oscillations. Naively, one might attempt to model these by calculating the pressure at the location of the bubble by a channel acoustics calculation and use this pressure as an input to the Rayleigh-Plesset equation. This would constitute a one-way coupling of the channel acoustics to the bubble volume oscillations, neglecting the influence of the bubble on the pressure. However, we have shown that the influence of the bubble on the pressure is dominant when nozzle failure sets in. The influence of the bubble on the pressure cannot be neglected. To calculate the volume oscillations of a bubble in an inkjet printhead, the full two-way coupling between bubble volume oscillations and the channel acoustics has to be taken into account. A linearized model, where this two-way coupling is taken into account, is described in chapter 3. The predictions by this model agree quantitatively with experimental observations. This is remarkable since the direct influence of the channel walls on the bubble volume oscillations was neglected. Only the influence of the volume oscillations on the pressure far away from the bubble was taken into account. This shows that for the bubble and channel sizes that were investigated, the two-way coupling between channel acoustics and bubble volume oscillations is much more important than an accurate modeling of the direct wall interaction. The quantitative agreement between measurements and the calculation results indicates that all the relevant effects have been taken into account. For the bubble volume oscillations, the relevant effects are identified.

- The inertia and viscous friction in the nozzle flow.
- The inertia, viscous friction, gas pressure, and surface tension effects of the radial flow field from the bubble. These effects constitute the Rayleigh-Plesset equation.

- The channel acoustics that are bidirectionally coupled to the nozzle flow and the bubble volume oscillations.

This model was tested rigorously in chapter 4. The model was extended to predict the current through the piezo actuator. This current depends on all of the parameters of the system, including the bubble volume. Usually, the other relevant parameters are fixed, so the bubble volume is the only unknown parameter. This parameter is changed until the calculated piezo current matches the measured piezo current as closely as possible. The bubble volume in the model for which this optimum occurs should be the volume of the bubble in the actual printhead. This optimization procedure can be used as a method to measure the bubble volume through its influence on the channel acoustics. The accuracy, and even the possibility of this acoustic measurement method is very sensitive to the accuracy of the underlying model. Attempting to use the model in this way is therefore a rigorous test of the completeness of the model and the validity of the underlying assumptions. The error was shown to be less than 10% for bubble volumes over 20 pl . For small bubbles, nonlinear effects that cannot be captured by the linear model are expected to be relevant. The accuracy of this novel measurement method shows that the list of relevant effects that was given above is exhaustive for the investigated parameter range.

In order to establish which effects are relevant given any set of parameters, the order of magnitude of their influences can be estimated and compared. This results in a set of dimensionless groups. In chapter 5, a complete set of such dimensionless groups was derived for a bubble in a pipe, and the effects that they compare were identified. An inkjet printhead consists of a large number of pipes, the ink channels, that connect nozzles to the ink reservoir. Therefore, these dimensionless groups for a bubble in a pipe show which effects can be neglected in an inkjet printhead given any set of parameters. Since the bubble volume and the actuation amplitude are most easily varied once the printhead has been constructed, the parameter space that is spanned by these two parameters was investigated. The importance of two-way coupling and the relative magnitude of the bubble volume oscillations, which indicates the importance of nonlinearity, were predicted. A nonlinear model in which two-way coupling is taken into account was developed to test these predictions. This model couples the Rayleigh-Plesset equation for the bubble volume oscillations, the axisymmetric Navier-Stokes equation for the nozzle flow and the low reduced frequency approximation for the channel acoustics. The theoretical predictions were confirmed with the numerical model.

By deriving and interpreting this set of dimensionless groups, we have developed a method to ascertain which effects are relevant and which effects can be neglected. Using this method consists of filling in the parameter values and evaluating the ratio. This is the simplest possible theoretical method to draw conclusions about a system. The availability of such methods indicates the maturity of a field of research. The volume oscillations of a bubble in a pipe are now basically understood.

When a bubble is entrained, it is initially too small to significantly disturb the droplet formation. If the bubble remains in the channel for a few hundred actuations, it grows by rectified diffusion of dissolved air towards the bubble. Eventually, it is large enough to disrupt the droplet formation. This disruption of the droplet formation is called nozzle failure. Nozzle failure does not occur

when the bubble is ejected from the nozzle before nozzle failure occurs. This raises two questions. How does a bubble move through a printhead? How does a bubble grow in a printhead? These questions are addressed in chapter 6. The motion will influence the gas diffusion, and thus the growth. The ratio of gas transport due to convection over gas transport due to diffusion is the Péclet number, which is large in this case. Therefore, the influence of the translational motion on the growth cannot be neglected. We have derived an expression for the gas diffusion towards the bubble that is valid for a translating bubble that undergoes volume oscillations. This leaves the bubble motion to be determined. This bubble motion can be calculated by balancing the forces on the bubble, since the mass of the bubble itself is negligible. The forces that were considered are added mass, primary Bjerknes force, secondary Bjerknes force, viscous drag, lift, history force, and lubrication force. Of these forces, history force and lift were neglected. Added mass, primary Bjerknes force, and viscous drag can be present in an infinite volume of liquid. Therefore, the expressions for an infinite volume of liquid can be used as an approximation of these forces in an inkjet printhead. However, secondary Bjerknes force and lubrication force are the result of the interaction between the bubble and the walls. Lubrication force is the near-field correction to the viscous drag, and it prevents the bubble from moving through walls. Since this effect is negligible unless the bubble is very close to the wall, the distance to the wall can be assumed to be much smaller than the radius of curvature or the wall. We derived an expression for lubrication force between a bubble and a flat wall. This approximation cannot be applied to the derivation of an expression for secondary Bjerknes force. This force was calculated by a three-dimensional potential flow calculation. This method to calculate the secondary Bjerknes force can be used for arbitrary geometries, but does not require a full potential flow calculation at each timestep of the simulation. The derived expressions were incorporated into the numerical model of bubble volume oscillations, channel acoustics, and nozzle flow.

With the developed numerical model, the translation of a bubble was investigated. The translation map of very small bubbles contains a limit cycle in the nozzle, some saddle points, and an attractor in the corner. During the part of the cycle where the bubble approaches the meniscus, the bubble might be ejected if its location is precisely right. As the bubble radius increases, the limit cycle disappears and the basin of attraction of the attractor in the corner expands to almost the entire nozzle and channel. This takes about 100 actuation cycles. After this has happened, the bubble can no longer be ejected and it will end up in the corner, where it is kept firmly in place by secondary Bjerknes force. Besides lubrication force and secondary Bjerknes force, no other forces are present since both the velocity and the pressure gradient vanish in the corner. In the corner, the bubble can grow due to rectified diffusion until the bubble volume is a few hundred picoliter. The volume of the acoustic field then limits the growth of the bubble.

The mechanisms that cause air entrainment have been studied in previous research. Air entrainment is caused by dust particles. These dust particles are transported from wherever they struck the nozzle plate to the nozzle by ink flows on the nozzle plate. These ink flows appear to obey plane potential flow. The driving force could not be identified in these studies, but two hypotheses were offered, air flow and Marangoni stress. In chapter 7, we have shown experimentally that the two-dimensional divergence of the depth averaged velocity

vanishes. We also derived this analytically, including the necessary conditions. A flow in a thin layer of liquid that is driven by Marangoni stress due to concentration gradients of an insoluble surfactant is two-dimensionally solenoidal if the concentration fluctuation in space and time is much smaller than the absolute magnitude of the concentration. With this result, the flow was shown to obey two-dimensional potential flow if the initial layer thickness is also constant in space. As a demonstration of how this result simplifies the analysis of thin film Marangoni flow, and to validate the result, a fingering instability that has been observed on the nozzle plate was analyzed. The predictions by this analysis were confirmed. This supports the developed theory and it suggests that the conditions for vanishing divergence are satisfied. The flow is driven by Marangoni stress due to an insoluble surfactant.

An extensive treatment of the evolution of an air bubble in an inkjet print-head was presented. The events that result in an entrained air bubble have been studied extensively in previous investigations, leaving three important open questions: How does a dust particle lead to air entrainment? What is the driving force of the flows on the nozzle plate? What makes these flows on the nozzle plate satisfy plane potential flow? The answers to the latter two questions given in this thesis. The mechanism of air entrainment was not discovered. In further investigations of nozzle failure, the mechanism of air entrainment is the most important fundamental question. From a technological point of view, a detailed study of how the nozzle shape influences bubble translation is an important issue, as it enables the design of automatically recovering nozzles, or at least a method of influencing the chance of recovery by bubble ejection. With respect to bubble dynamics in a pipe or tube, we hope that the presented methods, in particular the dimensionless groups, are used extensively so that the results are thoroughly validated and their limitations are discovered.

Samenvatting

We hebben de mechanismes onderzocht die leiden tot nozzle uitval door de invloed van een ingehapte luchtbel. We hebben onderzocht hoe (hoofdstukken 2, 3 en 4) en onder welke omstandigheden (hoofdstuk 5) een luchtbel tot uitval van de nozzle leidt, en wanneer deze omstandigheden op kunnen treden (hoofdstukken 6 en 7).

In hoofdstuk 2 hebben we de dominante effecten geïdentificeerd. Dit zijn de compressibiliteit van de luchtbel, de massatragheid van de inkt in de nozzle en de viskeuze wrijving in de nozzle. Een nozzle gedraagt zich als een tweede orde laag-doorlaat filter van snelheid in het kanaal naar snelheid in de nozzle. De afkap frequentie neemt af wanneer de bel groeit. Wanneer de afkapfrequentie van de nozzle veel kleiner wordt dan het dominante gedeelte van het spectrum van de snelheid in het kanaal, houdt de druppelvorming op.

De bel beïnvloedt de kanaalakoestiek en de snelheid van de inkt in de nozzle door zijn volume oscillaties. Men zou in eerste instantie ertoe geneigd kunnen zijn, deze volume-oscillaties te berekenen door eerst de druk ter plaatse van de luchtbel te berekenen met een kanaalakoestiek model, om daarna deze druk te gebruiken als bronterm in de Rayleigh-Plesset vergelijking. Zo zou een model ontstaan met koppeling in één richting, van de kanaalakoestiek naar de belvolume oscillaties, waarin de invloed van de luchtbel op de druk wordt verwaarloosd. We hebben echter in dit onderzoek aangetoond dat de invloed van de luchtbel op de druk dominant is wanneer de nozzle uitvalt. De invloed van de luchtbel op de druk kan dus zeker niet verwaarloosd worden. Om de volumeoscillaties van een luchtbel in een inkjet printkop te berekenen, moet de volledige koppeling in beide richtingen worden meegenomen. In hoofdstuk 3 beschrijven we een gelineariseerd model waarin deze tweewegkoppeling volledig is meegenomen. De voorspellingen door dit model komen kwantitatief overeen met experimentele waarnemingen. Dit is des te opmerkelijker aangezien de directe invloed van de wanden van het kanaal op de volumeoscillaties verwaarloosd is. Alleen de invloed van de wand op de druk op grote afstand van de bel is meegenomen. Dit toont aan dat voor de onderzochte bel- en kanaalgroottes de tweewegkoppeling tussen kanaalakoestiek en belvolumeoscillaties veel belangrijker is dan een nauwkeurige modellering van de directe interactie tussen de bel en de wand. De kwantitatieve overeenkomst toont aan dat alle relevante effecten in het model vertegenwoordigd zijn. Daarmee zijn alle relevante effecten geïdentificeerd.

- de massatraagheid en viskeuze wrijving in de nozzlestroming
- de massatraagheid, viskeuze wrijving, gasdruk en oppervlaktespanningseffecten van het radiële snelheidsveld van de luchtbel. Dit zijn de effecten

die samen de Rayleigh-Plessetvergelijking dicteren.

- de kanaalakoestiek die in beide richtingen gekoppeld is aan de nozzlestrooming en de belvolumeoscillaties

In hoofdstuk 4 is dit model grondig getest. Ook is het model daar uitgebreid zodat het ook de stroom door de actuator kan voorspellen. Deze stroom hangt van alle parameters van het systeem af, waaronder het belvolume. Normaal gesproken liggen alle andere parameters vast zodat het belvolume de enige onbekende parameter is. Deze parameter wordt gevarieerd totdat de berekende stroom door de piezoactuator zo goed mogelijk overeenkomt met de gemeten stroom. Het belvolume in het model waarbij dit optimum optreedt zou gelijk moeten zijn aan het werkelijke belvolume. Deze optimalisatieprocedure kan gebruikt worden om het belvolume te meten aan de hand van de invloed op de kanaalakoestiek. Of dit mogelijk is en hoe nauwkeurig deze methode is, is erg gevoelig voor de nauwkeurigheid van het onderliggende model. Dit gebruik van het model is daardoor een grondige test van hoe compleet het model is en van de geldigheid van de onderliggende aannames. De fout bleek minder dan 10% te zijn voor belvolumes boven de 20 picoliter. Voor kleine bellen zijn de nietlineaire effecten die in dit lineaire model niet aanwezig zijn, waarschijnlijk wel relevant. De nauwkeurigheid van deze nieuwe methode toont aan dat de gegeven lijst met relevante effecten volledig is in de onderzochte parameter ruimte.

Om te achterhalen welke effecten relevant zijn voor een gegeven verzameling parameters, kunnen de groottes van de invloeden van deze parameters worden afgeschat en vergeleken. Dit levert een verzameling dimensieloze grootheden op. In hoofdstuk 5 wordt een complete verzameling dimensieloze grootheden afgeleidt voor een bel in een pijp, en worden de effecten die ermee worden vergeleken afgeleidt. Een inkjet printkop bestaat uit een groot aantal pijpjes, de inktkanalen, die de nozzles met het inktreservoir verbinden. Daardoor kunnen deze dimensieloze groepen worden gebruikt om te achterhalen welke effecten verwaarloosd kunnen worden voor iedere willekeurige verzameling parameters. Omdat het belvolume en de actuatieamplitude het makkelijkst kunnen worden gevarieerd wanneer de printkop gebouwd is, hebben we de parameter ruimte onderzocht die wordt opgespannen door deze twee parameters. De relevantie is zo op theoretische gronden voorspeld van de tweewegkoppeling, en van de relatieve grootte van de belvolumeoscillaties die aangeven hoe belangrijk niet-lineaire effecten zijn. Een nietlineair model waarin rekening is gehouden met de tweewegkoppeling, is ontwikkeld zodat deze voorspellingen getest konden worden. In dit model zijn de Rayleigh-Plesset vergelijking voor de belvolumeoscillaties, een axisymmetrische Navier-Stokes solver voor de stroming in de nozzle en de low reduced frequency benadering voor de kanaalakoestiek gekoppeld. De voorspelling op theoretische gronden zijn bevestigd door de resultaten van het numerieke model.

Door deze verzameling dimensieloze grootheden af te leiden hebben we een methode ontwikkeld waarmee kan worden vastgesteld welke effecten relevant zijn en welke effecten verwaarloosd kunnen worden. Het gebruik van deze methode bestaat uit het invullen van de parameterwaardes en het evalueren van de breuk. Dit is de eenvoudigste theoretische methode waarmee conclusies kunnen worden gestrokken over een systeem. Het feit dat dergelijke methodes beschikbaar zijn geeft de volwassenheid van dit onderzoeksveld aan. In grote lijnen begrijpen we nu volumeoscillaties van een bel in een pijp.

En bel die net is ingehapt is te klein om de druppelvorming significant te verstoren. Indien de bel gedurende een paar honderd actuaties in het kanaal blijft, groeit deze door rectified diffusion van in de inkt opgeloste lucht naar de bel. Uiteindelijk zal de bel groot genoeg zijn om de druppelvorming te beëindigen. Het verhinderen van de druppelvorming door een luchtbel heet nozzle uitval. Een nozzle zal niet uitvallen wanneer de bel met een druppel mee uit de nozzle wordt gespoten voordat uitval plaats vindt. Dit roept twee vragen op. Hoe beweegt een bel door een printkop en hoe groeit een bel in een printkop? Deze vragen worden behandeld in hoofdstuk 6. De beweging beïnvloedt gasdiffusie, en dus de groei van de bel. De verhouding van gastransport door convectie gedeeld door gastransport door diffusie is het Péclet getal, en die is groot in dit geval. Daarom is de invloed van de translatie op de groei verwaarloosd. We hebben een uitdrukking van de gasdiffusie naar de bel toe afgeleid, die geldig is voor een translaterende luchtbel die volumeoscillaties ondergaat. Rest nog het bepalen van de belbeweging. Deze kan worden berekend met een krachtenbalans. De massa van de bel is verwaarloosbaar, dus de krachten op de luchtbel moeten in evenwicht zijn met elkaar. Added mass, primary Bjerknes force, secondary Bjerknes force, viskeuze wrijving, lift, Boussinesque-Basset history force en lubrication force zijn overwogen. History force en lift zijn na deze overweging verwaarloosd. Added mass, primary Bjerknes force en viskeuze wrijving kunnen ook aanwezig zijn in een onbegrensd volume vloeistof. Daardoor kunnen de uitdrukkingen voor deze krachten voor een bel in een onbegrensd volume vloeistof worden gebruikt als benadering voor een bel in een inkjet printkop. Secondary Bjerknes force en lubrication force zijn daarentegen het gevolg van interactie tussen de bel en de wand. Lubrication force is de correctie op de viskeuze wrijving door het nabije veld, en deze verhindert dat de bubble door de muur heen gaat. Doordat dit effect verwaarloosbaar klein is tenzij de bel zich zeer dicht bij de wand bevindt, kan worden aangenomen dat de afstand tot de wand veel kleiner is dan dan de kromtestraal van de wand. We hebben een uitdrukking afgeleid voor de lubrication force tussen een bel en een vlakke wand. Dezelfde benadering kan niet worden toegepast om de secondary Bjerknes force te berekenen. Die kracht is berekend met een driedimensionale potentiaalstromingsberekening. De gebruikte methode kan voor arbitraire geometriën worden toegepast, maar vereist toch geen volledige berekening van de potentiaalstroming tijdens iedere tijdstap van de simulatie. De verkregen uitdrukkingen zijn in het numerieke model geïmplementeerd, waarin de belvolumeoscillaties, kanaalakoestiek en nozzlestroming al werden berekend.

Met het ontwikkelde model is de verplaatsing van de bel onderzocht. De verplaatsing van zeer kleine bellen bevat een limit cycle in de nozzle, een aantal zadelpunten, en een aantrekkend punt in de hoek. Gedurende het deel van de limit cycle waarin de bel de meniscus benadert kan de bel naar buiten worden gespoten indien de locatie precies gunstig is. Naarmate de belstraal toeneemt, verdwijnt de limit cycle en groeit het gebied waarin de bel naar de hoek toegaat totdat die bijna de hele nozzle en het kanaal beslaat. Dit duurt ongeveer honderd actuaties. Daarna kan de bel niet meer naar buiten worden gespoten en komt in de hoek terecht, waar die zal blijven ten gevolge van secondary Bjerknes force. Behalve lubrication force en secondary Bjerknes force werken er geen andere krachten op de bel wanneer die zich in de hoek bevindt doordat de snelheid en drukgradient daar allebei klein zijn. In de hoek kan de bel vervolgens groeien door rectified diffusion totdat het belvolume een paar honderd picoliter is. De

volume amplitude van het akoestische veld is dan de beperkende factor in de belgroei.

De mechanismes van het inhappen van lucht zijn in eerder onderzoek uitgezocht. Lucht wordt ingehapt ten gevolge van de invloed van stofdeeltjes. Deze stofdeeltjes worden naar de nozzle verplaatst vanaf de plek waar ze de nozzleplaat raken door inktstroming op de nozzleplaat. Deze inktstromingen lijken zich te gedragen als potentiaalstroming in een vlak. De aandrijvende kracht kon niet met zekerheid worden geïdentificeerd in deze onderzoeken, maar twee hypothesen werden geponeerd, luchtstroming en Marangoni stress. In hoofdstuk 7 hebben we experimenteel aangetoond dat de tweedimensionale divergentie van de dieptegemiddelde snelheid in deze laag nul is. We hebben dit ook analytisch afgeleid, samen met de daarvoor noodzakelijke voorwaarden. Stroming in een dunne laag vloeistof die wordt aangedreven door Marangoni stress ten gevolge van de gradient van de concentratie van een niet oplosbare oppervlakteactieve stof, is tweedimensionaal divergentievrij indien de concentratiefluctuatie in tijd en ruimte veel kleiner is dan de absolute waarde van de concentratie. Met dit resultaat konden we aantonen dat de vloeistof stroomt als een potentiaalstroming wanneer tevens de initiële laagdikte constant is. Om te laten zien hoe dit resultaat de analyse van Marangoni flow in een dunne laag vereenvoudigd, hebben we een vingerinstabiliteit die op de nozzleplaat is waargenomen geanalyseerd. De voorspellingen van deze analyse werden door de waarnemingen bevestigd. Dit bevestigt de ontwikkelde theorie en het suggereert dat aan de voorwaarden voor divergentievrije stroming is voldaan in dit geval. We concluderen daarom dat deze stroming wordt aangedreven door een niet oplosbare oppervlakteactieve stof.

In dit proefschrift is een uitgebreide behandeling van het gedrag van een luchtbel in een inkjet printkop gegeven. De gebeurtenissen die leiden tot een ingehapte luchtbel zijn uitgebreid bestudeerd in eerder onderzoek. Daarbij zijn drie vragen onbeantwoord gebleven: Hoe leidt een stofdeeltje tot het inhappen van lucht? Wat drijft de stroming op een nozzleplaat aan? Waardoor gedragen deze stromingen zich als een potentiaalstroming? De laatste twee vragen zijn in dit proefschrift beantwoord. Hoe een stofdeeltje leidt tot het inhappen van lucht is niet ontdekt. In verder onderzoek van nozzle uitval is dit mechanisme het belangrijkste fundamentele punt. Van een technologisch perspectief is een gedetailleerd onderzoek van het de nozzlevorm verplaatsing van een luchtbel beïnvloedt een belangrijk open vraagstuk omdat deze kennis het ontwerpen van automatisch Herstellende nozzles mogelijk zou kunnen maken, of anders op zijn minst een handvat geeft voor het beïnvloeden van de herstellkans door het naar buiten spuiten van de luchtbel. Met betrekking tot het gedrag van een bel in een pijp hopen we dat de aangereikte methodes, in het bijzonder de dimensieloze groepen, op brede schaal worden toegepast zodat deze resultaten grondig worden gevalideerd en hun beperkingen aan het licht komen.

An extensive treatment of the evolution of an air bubble in an inkjet print-head was presented. The events that result in an entrained air bubble have been studied extensively in previous investigations, leaving three important open questions: How does a dust particle lead to air entrainment? What is the driving force of the flows on the nozzle plate? What makes these flows on the nozzle plate satisfy plane potential flow? The answers to the latter two questions given in this thesis. The mechanism of air entrainment was not discovered. In further investigations of nozzle failure, the mechanism of air entrainment is the most

important fundamental question. From a technological point of view, a detailed study of how the nozzle shape influences bubble translation is an important issue, as it enables the design of automatically recovering nozzles, or at least a method of influencing the chance of recovery by bubble ejection. With respect to bubble dynamics in a pipe or tube, we hope that the presented methods, in particular the dimensionless groups, are used extensively so that the results are thoroughly validated and their limitations are discovered.

Acknowledgements

The research in this thesis was financially supported by the Stichting Technologie en Wetenschap (technology and science foundation), Océ Technologies B.V., and the University of Twente, for which I am very grateful. It is wonderful to get paid for something you enjoy doing.

I am very grateful to Detlef Lohse for supporting this research project, for supporting my visit to MIT as a visiting student, and for supporting my research ideas. Detlef provided an environment where truth in science depends purely on the merit of the arguments. Requests for advice were usually met promptly, even those made in the middle of the night (by e-mail).

To Gerrit de Bruin, I am very grateful for generously given advice, support, anecdotes, and interesting problems. Andrea Prosperetti, Sacha Hilgenfeld, Jacco Snoeijer, Michel Versluis, and Devaraj van der Meer, thank you for the proofreading and valuable advice. I thank Joanita Leferink for tackling administrative problems as much as possible, and Bas Benschop for his help on IT. I would like to thank all the people at the Physics of Fluids group for the stimulating discussions, hints, tips, and pleasant company.

This research was a close cooperation with two other PhD students, Jos de Jong and Arjan van der Bos. When I started this project, I knew that I would be working together with Jos, an excellent experimenter who is friendly, reliable, and has a good sense of humor. I'm still amazed that I was so lucky again when Arjan joined this project. Apparently, being a good experimenter goes with a lot of other practical knowledge and I am indebted to them for lots of useful advice on how to handle computer and car problems.

At Océ, I mostly worked together with Hans Reinten, Herman Wijshoff, and Marc van den Berg. I greatly enjoyed the interesting discussions and the collegial friendship. Together, they have the skills to tackle any problem, and they used those skills to help me whenever I needed them. Thank you. I would like to thank the graduate students whom I have had the pleasure to work with at Océ: Bart Beulen, Mark van de Ven, Huub Borel, Koos Delescen, and Theo Driessen. Many people at Océ helped me on many occasions and therefore I am indebted to them. Two of them need to be mentioned in particular: Jan Simons for his help on the analysis of the electrical measurement methods, Wim de Zeeuw for his help on interpreting measurements on inkjet printheads.

I spend three wonderful months as a visiting student at MIT. I am very grateful to Gareth McKinley and Anette Hosoi for making this possible and providing the short but numerous pieces of valuable advice, and the occasional in-depth feedback. I thank Donna Wilker for the pleasant conversation and for solving all the bureaucratic problems, usually before I knew that they existed. A big thank you to Sarah Bates and all the others at the Hatsopoulos microfluids

lab for the friendship, the numerous interesting discussions on all kind of topics, the help in small and large ways, and their hospitality.

I felt truly welcome and at home at Océ, at the Physics of Fluids group, and at the Hatsopoulos Microfluids lab. This is a testament to the openminded, friendly people there. The world is a good place. Thank you.

To Wim Veldhuijzen and Annerie Kok, and Paul Klaarwater I am very grateful for their hospitality. I could stay overnight whenever a trip to Enschede required that, at times at very short notice. Enjoying their company made the trips to Enschede that much more pleasant.

I am very grateful to my parents, Eugene Jeurissen en Ria Jeurissen-Meijers, for their unconditional support, their advice, and their love. Thank you.

I am deeply grateful for the support, the love, the advice, and the direct help in dealing with problems from my wife, Wemke Veldhuijzen. It seems that every PhD research project has its crises. This one certainly did. Without Wemke's help and support in overcoming them, this thesis would not have reached its current quality. In addition to that she was a valuable reviewer of presentations and manuscripts. I am very lucky to get both the support of a loving partner and the support of a supportive but critical colleague from the same person.

About the author

Roger Josef Maria Jeurissen was born on November 7, 1977 in Soest, the Netherlands, to Eugène Maria Gerardus Jeurissen and Maria Gerarda Jeurissen-Meijers. He graduated from high school (VWO) at "het Baarnsch Lyceum" in Baarn in 1996. In August 1996, he started his studies of applied physics at the University of Twente in the Netherlands. He did his traineeship at MARIN in Wageningen, the Netherlands, in which he performed a verification study of boundary element methods for the analysis of sheet cavitation on ship propellers. In December 2004, he obtained his master degree with professor Detlef Lohse on air entrapment in piezo-driven inkjet printheads at Océ Technologies B.V. in Venlo, the Netherlands. In March 2005, he continued this subject with professor Detlef Lohse at the Physics of Fluids group of the University of Twente as a PhD student in close cooperation with Océ Technologies B.V. until September 2009. In February, March, and April of 2008, he joined the groups of professor Gareth McKinley and professor Anette Hosoi at the Massachusetts Institute of Technology as a visiting student. On June 27, 2009, he married Wemke Veldhuijzen and their daughter, Jorinde Jeurissen, was born on August 29, 2009.